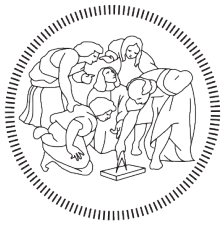

POLITECNICO
MILANO 1863

SCHOOL OF INDUSTRIAL AND INFORMATION ENGINEERING
Department of Aerospace Science and Technology
Master of Science in SPACE ENGINEERING

Solar Array Drive Mechanism disturbance estimation: a robust approach applied to Sentinel-2 mission

Master Thesis

Student:
Gianluca Mingione
Matricola 899187

Supervisor:
Prof. Camilla Colombo
Co-supervisor:
Davide Oddenino

Academic Year 2020-2021

When referring to this work, full bibliographic details must be given, i.e.
Gianluca Mingione, "Solar Array Drive Mechanism disturbance estimation: a robust approach applied to Sentinel-2 mission". 2021, Politecnico di Milano, Faculty of Industrial Engineering, Department of Aerospace Science and Technologies, Master in Space Engineering, Supervisor: Camilla Colombo, Co-supervisor: Davide Oddenino

Printed in Italy

To my family

Abstract

Pointing stability requirements have become more demanding for high-precision scientific and observation missions. In the last decades, space agencies have been pushing towards higher performing payloads and on-board instruments to perform more precise and detailed observations. Nevertheless, high-performance instruments are typically more sensitive to micro-vibrations. These perturbations are in general amplified by the satellite structure when being transmitted to sensitive payload units and might degrade considerably the instrument pointing accuracy. There are different sources of micro-vibrations on-board a spacecraft, including the solar array oscillations induced by the Solar Array Drive Mechanism (SADM). Following the experience of flying satellites with rotating solar arrays equipped with SADM, it has been shown that even a small input due to geometry errors or alignment imperfections can excite much larger oscillations of the solar array than predicted. In order to cope with stringent stability requirements, a toolbox to assess the effect of on-board induced oscillations on the attitude performances was developed in previous studies. In addition, it was demonstrated that a major cause of disturbance amplifications is the coupling between the moving SADM and the solar array flexible body modes of vibration. This thesis aims to design an estimator which robustly evaluates the input disturbance generated by the solar array rotation mechanism by means of the information produced by the developed toolbox. The estimation of the frequency content and the amplitude spectrum of the micro-vibrations induced by the SADM allows to prevent the magnification of the input disturbance promoted by the spacecraft dynamics. In the present study, a survey on different estimation techniques is carried out, ranging from nonlinear real-time estimation techniques which rely on the Kalman filter formulation to a more robust approach based on the $\mathcal{H}_\infty$ theory. The present work develops a method which combines the different estimation techniques and exploits their definition while trying to compensate for their limitations. The result is an estimator made up of a first robust system-based segment in series with a second part that depends only on the shape of the input disturbance.

Sommario

I requisiti di missione relativi alla stabilità di puntamento per missioni scientifiche e di osservazione della Terra stanno diventando più stringenti rispetto al passato. Negli ultimi decenni le agenzie spaziali si stanno spingendo verso una strumentazione scientifica da operare a bordo di satelliti sempre più precisa al fine di permettere osservazioni più dettagliate. Tuttavia, strumentazioni scientifiche ad alta precisione sono solitamente più sensibili alle microvibrazioni. Questi disturbi sono in genere amplificati dalla struttura del satellite e tendono a degradare considerevolmente l'accuratezza di puntamento. A bordo di un satellite possono essere presenti diverse fonti di microvibrazioni, incluse le oscillazioni dei pannelli solari indotte dal meccanismo che permette la loro rotazione attorno al proprio asse. Dai dati di missioni spaziali in volo attorno al pianeta, è stato dimostrato che piccoli errori o imperfezioni a livello di tale meccanismo possono generare oscillazioni ben maggiori di quelle previste. Al fine di fronteggiare requisiti di missione così stringenti, studi precedenti hanno sviluppato e validato un *toolbox* per la valutazione degli effetti indotti dal meccanismo di rotazione sull'assetto del satellite e si è dimostrato che questi effetti vengono maggiormente amplificati a causa dell'accoppiamento delle componenti in frequenza del disturbo con i modi propri di vibrare del pannello solare. L'obiettivo di questa tesi consiste nel creare uno stimatore che valuti in modo robusto il disturbo generato dal meccanismo di rotazione del pannello solare attraverso i modelli sviluppati negli studi precedenti. La stima del contenuto in frequenza delle microvibrazioni indotte da tale meccanismo permette infatti di prevenire l'amplificazione di questi disturbi. Questa tesi descrive inoltre diverse tecniche di stima esistenti ed esamina sia approcci che forniscono dati in tempo reale fondati sulla formulazione non lineare del filtro di Kalman, sia metodi più robusti basati sulla teoria del controllo $\mathcal{H}_\infty$. In particolare, in questo elaborato viene sviluppato un approccio che combina diverse tecniche di stima ed utilizza i vantaggi dei diversi metodi cercando allo stesso tempo di compensarne le relative limitazioni. Il risultato è uno stimatore formato da una prima parte robusta che coinvolge il solo sistema dinamico, in serie con una seconda parte che dipende unicamente dalla struttura del disturbo da valutare.

Contents

List of Figures

List of Tables

List of Acronyms

AOCS	Attitude and Orbit Control System
ARE	Algebraic Riccati Equation
ECSS	European Cooperation for Space Standardization
EKF	Extended Kalman Filter
ESA	European Space Agency
ESTEC	European Space Research and Technology Centre
FFT	Fast Fourier Transform
IMU	Inertial Measurement Unit
LFT	Linear Fractional Transformation
LPV	Linear Parameter Varying
LTI	Linear Time Invariant
NASA	National Aeronautics and Space Administration
PSD	Power Spectral Density
SADM	Solar Array Drive Mechanism
SDT	Satellite Dynamics Toolbox
SVD	Singular Value Decomposition
UKF	Unscented Kalman Filter

Nomenclature

$[\mathbf{r}]^\wedge$	Skew-symmetric matrix associated to $\mathbf{r}$ representing the cross product (hat operator)
$\boldsymbol{\Delta}$	System parameter uncertainty block
$\boldsymbol{\eta}$	Solar array model coordinates vector
$\boldsymbol{\omega}$	Angular velocity vector
$\boldsymbol{\tau}_{PG}$	Kinematic model between points P and G
$\delta\theta$	Angular deflection of gearbox output shaft with respect to input shaft
$\dot{\boldsymbol{\omega}}$	Acceleration vector
γ	Stepper motor electrical micro-step angle
$\mathcal{C}$	Controllability matrix
$\mathcal{F}_l$	Lower LFT
$\mathcal{F}_u$	Upper LFT
$\mathcal{O}$	Observability matrix
$\mathcal{R}_A$	Reference frame rigidly attached to satellite base at appendage connection point
$\mathcal{R}_B$	Reference frame rigidly attached to satellite base at its centre of mass
$\mathcal{R}_i$	Inertial frame
$\mathcal{R}_{SA}$	Reference frame rigidly attached to solar array
ω_i	Angular frequency of i-th flexible mode
$\overline{\sigma}$	Largest singular value
σ	Singular value
$\underline{\sigma}$	Smallest singular value
$\mathbf{a}$	Acceleration vector
$\mathbf{A}^*$	Conjugate transpose of matrix $\mathbf{A}$
$\mathbf{D}_G$	Satellite base dynamic model at point G
$\mathbf{F}$	Force vector

$\mathbf{G}(s)$	System transfer function
$\mathbf{I}_n$	Identity matrix of size n
$\mathbf{J}_G^B$	Satellite base inertia matrix with respect to point G
$\mathbf{l}_P^i$	Modal participation vector expressed at point P of i-th flexible mode
$\mathbf{r}$	Position vector
$\mathbf{R}_x$	Rotation matrix about axis x
$\mathbf{T}$	Torque vector
$\mathbf{u}(t)$	Input vector
$\mathbf{v}$	Velocity vector
$\mathbf{w}(t)$	Input disturbance vector
$\mathbf{x}(t)$	State vector
$\mathbf{y}(t)$	Output vector
$\mathbf{z}(t)$	Performance vector
ξ_i	Damping ratio of i-th flexible mode
C	Damping coefficient
$F(s)$	Estimator transfer function
I	Stepper motor two-phase current amplitude
K	Stiffness coefficient
$K(s)$	Controller transfer function
K_m	Motor torque constant
m_B	Satellite base mass
N_g	Gearbox or transmission ratio
z	Gear teeth number

Chapter 1

Introduction

DURING the last decades, there has been a constant trend by both the European Space Agency (ESA) and the National Aeronautics and Space Administration (NASA) to push towards higher performing payloads and on-board instruments [9]. This interest derives from the growing need of more stringent pointing performance for future observation and science missions. High-performance instruments are generally extremely sensitive to micro-vibration that can degrade their pointing accuracy and become critical for very demanding missions. Micro-vibrations or jitter, as defined in the European Cooperation for Space Standardisation (ECSS) for mechanical loads [29], are low-level vibrations occurring during on-orbit operations of mobile or vibratory parts. These perturbations are in general amplified by the satellite structure when being transmitted to sensitive payload units and as a result, micro-vibrations might cause severe disturbances and degrade instrument pointing performances. In fact, the inherent lightweight nature of the majority of spacecraft structures and the resulting multitude of closely spaced, lightly damped, low-frequency flexible body modes of vibration impact severely the final pointing budget. Micro-vibrations are generated by internal mechanisms placed on-board the spacecraft and typically include rotating mechanisms such as reaction wheels or momentum wheels as well as sensor-related mechanical devices like cryocoolers, cryopumps or scanning mirrors. Other micro-vibration sources encompass high gain antennas and solar array drive mechanisms. An additional aspect that makes the spacecraft micro-vibration problem organisationally challenging is its multi-disciplinary nature which involves multiple engineering disciplines. Structure, control and system engineering teams need to collaborate in order to limit the propagation of the internal disturbance and the amplification of the natural modes of the spacecraft structure.

An exemplary demonstration of the problems related to the generation of micro-vibration disturbance and pointing performance degradation was the Hubble Space Telescope mission [11]. Not long after its on-orbit activation, issues impacting the telescope capability to perform its mission were encountered. Examination of the real-time flight telemetry data revealed that the spacecraft was experiencing unexpectedly large disturbances that were most pronounced as the spacecraft entered or left the Earth's shadow. Further studies [23] identified the cause of the anomalous perturbation in the solar array flexible mode that was thermally excited by the transition from and to eclipse. The attitude control was then redesigned in order to take into account this phenomenon.

This example illustrates the necessity of predicting, managing, and controlling on-board micro-vibrations for spacecrafts accommodating sensitive sensor payloads with stringent requirements.

The present work was developed within the framework of an internship in the AOCS

(Attitude and Orbit Control Systems) & Pointing Systems Section (TEC-SAA) of the European Space Research and Technology Centre (ESTEC) situated in Noordwijk, the Netherlands. ESTEC is the European Space Agency's main technology development and test centre for spacecraft and space technology.

In this thesis, the evaluation of micro-vibration disturbance generated by the Solar Array Drive Mechanism (SADM) is investigated. In particular, a new approach involving two filters in series is introduced and applied to the specific case of ESA's Sentinel-2 mission.

1.1 State of the art

This section provides an overview of the models used to describe the dynamics of a generic spacecraft when the external forces and torques acting on the body are known. In addition, it describes the most common estimation techniques and their evolution over time.

The dynamics of a spacecraft when approximated as a rigid body is characterised by six degrees of freedom, namely three translational and three rotational degrees of freedom. The translational and rotational dynamics can be evaluated using the Newton's second law of motion and the Euler's equations respectively. However, it can be convenient to treat all the six degrees of freedom all together and include couplings between rotations and translations. Alazard et al. [3] developed a dynamic model for spacecraft which accounts for the global dynamics of rigid body and incorporates the possibility to connect multiple flexible appendages. In other words, the spacecraft is approximated as a rigid body which accommodates the main subsystems, and several appendages such as antennas, solar arrays or propellant tanks can be connected to the rigid base and the flexible nature of their structure is preserved. The rotational dynamics is approximated to be linear, by assuming that the angular velocity of the spacecraft are small. The linear assumption is usually realistic for such systems, since external perturbations and thus motions are typically small. Accordingly, this model allows to compute the linear inverse dynamic model of a generic spacecraft, i.e. the translational and angular accelerations of the body when the forces and torques acting on the spacecraft are known. Moreover, it is able to account for the rotation of the single appendages and includes the possibility to consider parametric variations of the system parameters due to modeling uncertainties. In addition, the MATLAB® implementation of the model was carried out and described in the user guide [2] which introduces a toolbox called Satellite Dynamics Toolbox (SDT). The user guide describes the modeling principles used in the toolbox and includes several examples. In the case one or more appendages are solar arrays, Alazard and Cumer specialised the toolbox even further in [1] by encompassing the dynamics of the solar array drive mechanism that allows the continuous rotation of the appendage in order to collect maximum sun power onto the solar cells. The main mechanical components of the SADM are the stepper motor which is responsible to generate the actual rotation and the gearbox that transmits the motor torque to the solar array. A purely torsional model along the axis of the solar array was developed and integrated in SDT model. In particular, the report [1] is focused on the study of the overall dynamics of Sentinel-2A satellite. In addition, a frequency analysis of the system is included and reveals that the Sentinel-2 SADM generates some perturbation torques. The torsional disturbance at gearbox level is dominant and is characterised as a sawtooth signal with harmonic components that depend on the assembly physical and geometrical parameters.

The evaluation of the gearbox disturbance can be performed by using different estimation techniques. The most common approach makes use of the Kalman filter, which is the optimal linear estimator for linear systems with additive white noise in both the dynamics and the measurement systems [28]. The filter is named after Rudolph E. Kálmán, who in 1960 published the article [20] describing a recursive solution to the discrete-time linear filtering problem. Since then, the Kalman filter has found application in virtually every area of engineering, including guidance, navigation, and control of vehicles, signal processing, robotics and trajectory optimisation [33]. In addition, several extensions and generalisations to the Kalman filter have been developed. In particular, since most of the problems in engineering are not linear, different methods to apply the filter to nonlinear system have been introduced. A common extension of the Kalman filter to nonlinear systems is the Extended Kalman Filter (EKF), which relies on Taylor series expansions to linearise the dynamics and the measurement equation about a working point. The idea of the EKF was originally proposed by Stanley Schmidt so that the Kalman filter could be applied to nonlinear spacecraft navigation problems [5]. The EKF is the most widely applied state estimation algorithm for nonlinear systems [28]. However, when the system dynamics and the measurement equation are highly nonlinear, the extended Kalman filter may produce unreliable results because of the fact that the covariance of the state is propagated in time through linearisation of the nonlinear model. The Unscented Kalman Filter (UKF) uses a deterministic sampling technique known as the unscented transformation to generate a set of sample points around the mean [19]. These points are then propagated through the nonlinear dynamics of the system and a new mean and covariance are computed. The resulting filter depends on how the transformed statistics of the unscented transformation are calculated and which set of points are used. For certain systems, the UKF gives more accurate estimates of of the true mean and covariance with respect to the EKF [28]. This can be verified with a Taylor series expansion of the posterior statistics. Moreover, the UKF removes the requirement to explicitly calculate Jacobians, which might be a difficult task for complicated functions (i.e, requiring complex derivatives if done analytically or computationally costly if done numerically), or even impossible in case the functions are not differentiable. The UKF was first published in 1995 and has been rapidly finding applications in several areas, including aircraft model estimation, financial forecasting and neural network training [6]. In case the nonlinearities of the system are particularly severe, an alternative approach can be used, which makes use of a large set of particles to represent the posterior distribution of the stochastic process. This method is called particle filter and was first introduced in the 1940s by the work of Metropolis and Wiener [22]. But only since the 1980s has computational power been adequate for its implementation. Nonetheless, even now it is the computational burden of the particle filter its main obstacle to a more widespread use. Particle filters find applications in different fields, including signal and image processing, robotics, artificial intelligence, economics, and mathematical finance.

Besides the different estimation techniques introduced above which are all based on the Kalman filter formulation, more robust approaches have also been introduced during the last decades to which rely on the $\mathcal{H}_\infty$ theory. The primary objective of the linear $\mathcal{H}_\infty$ theory was addressed to the synthesis of a controller that stabilised the system while minimising the input-output worst-case scenario in terms of magnitude amplification over all the frequency spectrum. The estimation problem of specific quantities of the system can be considered as a special case and is called $\mathcal{H}_\infty$ filtering [34]. The phrase $\mathcal{H}_\infty$ control comes from the name of the mathematical space over which the optimisation takes place, namely the Hardy space. These methods were originally introduced into control

theory in the late 1970s by Zames [32] and different techniques have been developed for the synthesis of the controller, including Riccati-based approaches which require the solution of two algebraic Riccati equations [15], and optimisation-based reformulations of the Riccati equations which make use of linear matrix inequalities [13].

1.2 Scope of the thesis

The scope of the present thesis is the estimation of the amplitude and frequency spectra of the disturbance generated by the solar array drive mechanism. In particular, the estimation concerns the perturbation produced by the SADM gearbox of the Sentinel-2 mission and it is to be performed by means of the information provided by the on-board gyroscopes along with the model of the spacecraft dynamics.

The direct evaluation of the amplitude and frequency of the harmonic components in which the input disturbance can be decomposed cannot be performed. The estimation using techniques which rely on the nonlinear Kalman filter formulation present some observability problems, and this result will be demonstrated by considering a simple one-dimensional system with a single degree of freedom. On the other hand, evaluation through approaches that are based on the Fourier series are not possible either, since direct information of the input signal would be needed and there is no sensor on-board the spacecraft which provides such output.

This thesis introduces an alternative approach which makes use of an estimator made up of two parts. A first segment deals with the robust estimation of the disturbance acting on the gearbox so that the second part has access to direct information of the input signal and the methods mentioned above could be employed. This technique produces generates different advantages. First of all, it allows to fulfil the objective to produce an estimation of both the frequency and the amplitude spectrum. In addition, the division of the estimator into two separate parts permits to create two simpler components devoted to a specific function, with no observability-related issues due to the reduced size of the states to be considered. In particular, the first component can be designed as a system-based estimator which evaluates the input disturbance independently of its structure or variation in time. Furthermore, since the system describing the satellite dynamics can be approximated as linear, robust approaches which rely on linear formulations can be used. Moreover, the second part of the estimator is system-independent and is only based on the input disturbance shape. The present work explores both the formulation based on the Fourier series and the Kalman filter theory and compares the results that these techniques produce when the input disturbance is a single harmonic with constant or time-varying amplitude and frequency or is generated by the sum of multiple harmonics.

1.3 Thesis outline

This thesis provides a detailed presentation of the most common estimation techniques and their derivation. In addition, it applies the different approaches to a simple system with a single degree of freedom to compare and investigate their behaviour when the input disturbance is modeled in several forms. In addition, the theory related to the mathematical modeling of the satellite dynamics is introduced and later formulated in a state-space representation. Eventually, the methods for the estimation of the gearbox disturbance acting on the real system are presented.

Chapter 2 describes the full mathematical model describing the dynamics of a generic spacecraft equipped with a solar array drive mechanism. The theory is then specialised to the Sentinel-2 case.

Chapter 3 shows the procedure to implement a robust controller using the $\mathcal{H}_\infty$ formulation. The $\mathcal{H}_\infty$ filtering theory is later presented as a special formulation of the control problem for the implementation of the robust system-based estimator.

Chapter 4 presents the most common nonlinear estimation techniques which rely on the nonlinear formulation of the Kalman filter. An algorithm summarising the steps to be performed to implement the different filters is also included.

Chapter 5 introduces a simple one-dimensional system with a single degree of freedom subjected to a harmonic disturbance and presents the problems that arise if a direct estimation method is implemented for the evaluation of the input amplitude and frequency. An alternative approach is described and a comparison of the estimation results produced by the Fourier analysis and the Kalman filter formulation for different input cases is explored.

Chapter 6 applies the developed theory to estimate the amplitude and frequency spectra of the disturbance generated by Sentinel-2 gearbox and reports the results obtained by the different approaches.

Chapter 7 concludes the thesis and describes the main achievements obtained in the present work as well as the possible future developments.

Chapter 2

Mathematical modeling of satellite dynamics

2.1 Satellite dynamic toolbox

THE Satellite Dynamic Toolbox (SDT) is a mathematical model designed for the computation of the linear dynamics of a generic spacecraft made up of a main body, which is assumed to be rigid, and one or several appendages [2]. The appendages can be considered as flexible and/or rotating bodies and are connected to the base at specific points P_i. By means of the SDT the inverse dynamic model of the spacecraft is typically computed, i.e. the translational and rotational accelerations of the spacecraft are obtained from knowledge of the forces and torques acting on the main body.

The dynamic model makes use of the Newton-Euler equations for the description of the body movement in the three-dimensional space, which are linearised by assuming that the angular velocity $\boldsymbol{\omega}$ of the spacecraft is small. The linear assumption is usually realistic for such systems, since external perturbations and thus motions are typically small. The 3 degrees of freedom associated to body translation and the 3 degrees of freedom related to rotation are then treated together.

As an example, Figure 2.1 shows the structure of a spacecraft composed of a rigid main body or hub with centre of mass in G, and a solar array as appendage with centre of mass in C and connected to the base at point P. Two reference frames are introduced to develop the dynamics of the overall spacecraft: $\mathcal{R}_B$ is the frame with centre at point G and rigidly attached to the hub, whereas $\mathcal{R}_A$ is the same frame with centre at the connection location P, with x-axis aligned with the solar array longitudinal axis. To conclude, a third reference frame can be introduced in case the appendage can rotate around the longitudinal axis. Such frame is denoted as $\mathcal{R}_{SA}$, is rigidly attached to the solar array and will rotate around the x-axis if viewed from a frame fixed with respect to the hub. The last two reference frames shall be introduced for each different appendage.

From an inertial frame $\mathcal{R}_i$ the position vector of any point of the spacecraft base, for instance point P, can be written as the sum:

$$\mathbf{r}_P = \mathbf{r}_G + \mathbf{r}_{GP} \tag{2.1}$$

where $\mathbf{r}_P$ and $\mathbf{r}_G$ are the inertial position of point P and of the hub's centre of mass respectively, while $\mathbf{r}_{GP}$ is the vector position of P with respect to the centre of mass G.

Since the base of the spacecraft is assumed to be rigid, vector $\mathbf{r}_{GP}$ has a constant magnitude and its direction will generally change in time due to rotational movement if

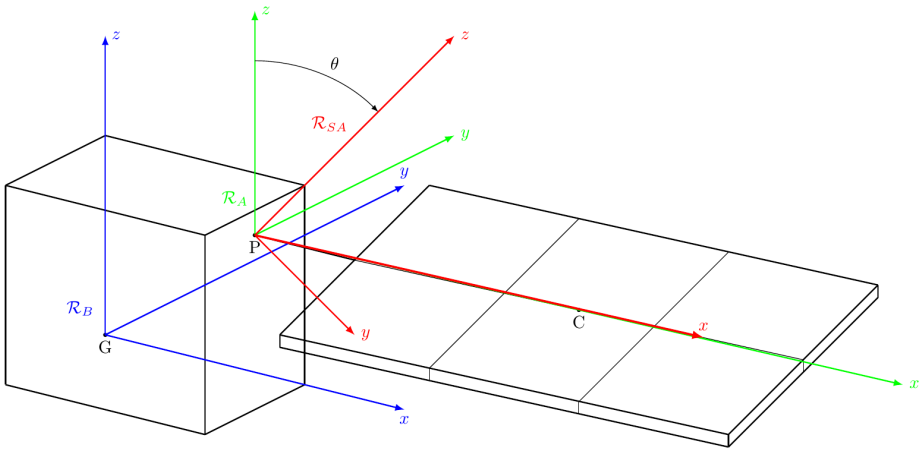

Figure 2.1: Physical model of a spacecraft with one appendage

seen from an inertial frame, while it will remain constant from a body fixed frame such as $\mathcal{R}_B$.

Accordingly, using the transport theorem the time derivative of vector $\mathbf{r}_{GP}$ with respect to the inertial frame $\mathcal{R}_i$ can be written as [3]:

$$\left.\frac{d\mathbf{r}_{GP}}{dt}\right|_{\mathcal{R}_i} = \left.\frac{d\mathbf{r}_{GP}}{dt}\right|_{\mathcal{R}_B} + \boldsymbol{\omega} \wedge \mathbf{r}_{GP} = \boldsymbol{\omega} \wedge \mathbf{r}_{GP} \tag{2.2}$$

since $\mathbf{r}_{GP}$ is constant both in magnitude and direction in frame $\mathcal{R}_B$, and where $\boldsymbol{\omega}$ denotes the angular velocity of frame $\mathcal{R}_B$ relative to $\mathcal{R}_i$, which coincides with the angular velocity of the body as frame $\mathcal{R}_B$ is rigidly attached to the base.

By carrying out the time derivative of equation (2.1), the inertial velocity $\mathbf{v}_P$ can be computed as:

$$\mathbf{v}_P = \mathbf{v}_G + \boldsymbol{\omega} \wedge \mathbf{r}_{GP} \tag{2.3}$$

which allows to obtain the velocity of any point of the rigid base from knowledge of the centre of mass velocity $\mathbf{v}_G$, the position of point P with respect to G, and the angular velocity of the body.

The components of vector $\mathbf{r}_{GP}$ can be written with respect to any reference frame as:

$$\mathbf{r}_{GP} = \begin{Bmatrix} x \\ y \\ z \end{Bmatrix} \tag{2.4}$$

where such quantities are strictly dependent on the selected reference frame.

By introducing the skew-symmetric matrix $[\mathbf{r}_{GP}]^\wedge$ associated with vector $\mathbf{r}_{PG}$, defined as:

$$[\mathbf{r}_{GP}]^\wedge = \begin{bmatrix} 0 & -z & y \\ z & 0 & -x \\ -y & x & 0 \end{bmatrix} \tag{2.5}$$

and with the property $([\mathbf{r}_{GP}]^\wedge)^T = -[\mathbf{r}_{GP}]^\wedge$, the cross product in equation (2.3) can be written as the product of a matrix and a vector:

$$\boldsymbol{\omega} \wedge \mathbf{r}_{GP} = -\mathbf{r}_{GP} \wedge \boldsymbol{\omega} = -[\mathbf{r}_{GP}]^\wedge \boldsymbol{\omega} \tag{2.6}$$

The velocity of any point P of the rigid hub can then be alternatively computed as [3]:

$$\mathbf{v}_P = \mathbf{v}_G - [\mathbf{r}_{GP}]^\wedge \boldsymbol{\omega} \tag{2.7}$$

Therefore, if both translational and rotational velocity of the hub are considered and embedded in a single vector, velocities of the centre of mass can be written in a compact form as:

$$\begin{Bmatrix} \mathbf{v}_G \\ \boldsymbol{\omega} \end{Bmatrix} = \boldsymbol{\tau}_{GP} \begin{Bmatrix} \mathbf{v}_P \\ \boldsymbol{\omega} \end{Bmatrix} = \begin{bmatrix} \mathbf{I}_3 & [\mathbf{r}_{GP}]^\wedge \\ \mathbf{0}_3 & \mathbf{I}_3 \end{bmatrix} \begin{Bmatrix} \mathbf{v}_P \\ \boldsymbol{\omega} \end{Bmatrix} \tag{2.8}$$

where matrix $\boldsymbol{\tau}_{GP}$ is the kinematic model that allows to pass from velocities of point P to velocities of point G.

Similarly, the relation between the acceleration of the centre of mass and any point of the rigid base can be inferred by deriving in time equation (2.3) as:

$$\mathbf{a}_P = \mathbf{a}_G + \dot{\boldsymbol{\omega}} \wedge \mathbf{r}_{GP} + \boldsymbol{\omega} \wedge (\boldsymbol{\omega} \wedge \mathbf{r}_{PG}) \tag{2.9}$$

Since $\boldsymbol{\omega}$ is small, the nonlinear term can be neglected and the previous relation can be written as:

$$\mathbf{a}_P = \mathbf{a}_G - [\mathbf{r}_{GP}]^\wedge \dot{\boldsymbol{\omega}} \tag{2.10}$$

The same kinematic model between acceleration at P and at G can then be introduced as:

$$\begin{Bmatrix} \mathbf{a}_G \\ \dot{\boldsymbol{\omega}} \end{Bmatrix} = \boldsymbol{\tau}_{GP} \begin{Bmatrix} \mathbf{a}_P \\ \dot{\boldsymbol{\omega}} \end{Bmatrix} = \begin{bmatrix} \mathbf{I}_3 & [\mathbf{r}_{GP}]^\wedge \\ \mathbf{0}_3 & \mathbf{I}_3 \end{bmatrix} \begin{Bmatrix} \mathbf{a}_P \\ \dot{\boldsymbol{\omega}} \end{Bmatrix} \tag{2.11}$$

The previous kinematic models are particularly useful to compute the velocities and acceleration starting from knowledge of the same quantities with respect to a different point of the structure. However, the dynamic model of the rigid body shall be introduced to obtain information of the spacecraft motion. Inertial quantities of the structure, such as the mass m_B of the base and its inertia matrix $\mathbf{J}_G^B$ with respect to its centre of mass in the frame $\mathcal{R}_B$ are typically known. By combining Newton's and linear Euler's equations, the dynamic model $\mathbf{D}_B$ is computed as follows:

$$\begin{Bmatrix} \mathbf{F}_{ext} \\ \mathbf{T}_{ext,G} \end{Bmatrix} = \mathbf{D}_B \begin{Bmatrix} \mathbf{a}_G \\ \dot{\boldsymbol{\omega}} \end{Bmatrix} = \begin{bmatrix} m_B \mathbf{I}_3 & \mathbf{0}_3 \\ \mathbf{0}_3 & \mathbf{J}_G^B \end{bmatrix} \begin{Bmatrix} \mathbf{a}_G \\ \dot{\boldsymbol{\omega}} \end{Bmatrix} \tag{2.12}$$

where $\mathbf{F}_{ext}$ and $\mathbf{T}_{ext,G}$ are the external forces and torques acting on the hub's centre of mass G respectively.

The power generated by such external forces and torques along a virtual velocity field is independent of the point of application and can be expressed as [3]:

$$P_{ext} = \begin{Bmatrix} \mathbf{v}_G \\ \boldsymbol{\omega} \end{Bmatrix}^T \begin{Bmatrix} \mathbf{F}_{ext} \\ \mathbf{T}_{ext,G} \end{Bmatrix} = \begin{Bmatrix} \mathbf{v}_P \\ \boldsymbol{\omega} \end{Bmatrix}^T \begin{Bmatrix} \mathbf{F}_{ext} \\ \mathbf{T}_{ext,P} \end{Bmatrix} \tag{2.13}$$

By means of the kinematic model derived in equation (2.8) the following relation can be obtained:

$$\begin{Bmatrix} \mathbf{v}_G \\ \boldsymbol{\omega} \end{Bmatrix}^T \begin{Bmatrix} \mathbf{F}_{ext} \\ \mathbf{T}_{ext,G} \end{Bmatrix} = \left(\boldsymbol{\tau}_{GP} \begin{Bmatrix} \mathbf{v}_P \\ \boldsymbol{\omega} \end{Bmatrix} \right)^T \begin{Bmatrix} \mathbf{F}_{ext} \\ \mathbf{T}_{ext,G} \end{Bmatrix} = \begin{Bmatrix} \mathbf{v}_P \\ \boldsymbol{\omega} \end{Bmatrix}^T \boldsymbol{\tau}_{GP}^T \begin{Bmatrix} \mathbf{F}_{ext} \\ \mathbf{T}_{ext,G} \end{Bmatrix} \tag{2.14}$$

The expression of the external power can then be written as:

$$P_{ext} = \begin{Bmatrix} \mathbf{v}_P \\ \boldsymbol{\omega} \end{Bmatrix}^T \boldsymbol{\tau}_{GP}^T \begin{Bmatrix} \mathbf{F}_{ext} \\ \mathbf{T}_{ext,G} \end{Bmatrix} = \begin{Bmatrix} \mathbf{v}_P \\ \boldsymbol{\omega} \end{Bmatrix}^T \begin{Bmatrix} \mathbf{F}_{ext} \\ \mathbf{T}_{ext,P} \end{Bmatrix} \tag{2.15}$$

From the last equivalence the following expression is derived:

$$\begin{Bmatrix} \mathbf{F}_{ext} \\ \mathbf{T}_{ext,P} \end{Bmatrix} = \boldsymbol{\tau}_{GP}^T \begin{Bmatrix} \mathbf{F}_{ext} \\ \mathbf{T}_{ext,G} \end{Bmatrix} = \begin{bmatrix} \mathbf{I}_3 & \mathbf{0}_3 \\ -[\mathbf{r}_{GP}]^\wedge & \mathbf{I}_3 \end{bmatrix} \begin{Bmatrix} \mathbf{F}_{ext} \\ \mathbf{T}_{ext,G} \end{Bmatrix} \tag{2.16}$$

The previous equation allows to express the external forces and torques with respect to any point of the structure from knowledge of such quantities acting on the centre of mass of the body. In addition, it permits to derive the dynamic model of the spacecraft base with respect to the generic point P.

By substituting equation (2.11) into (2.12) and finally into equation (2.16) the following expression is derived:

$$\begin{Bmatrix} \mathbf{F}_{ext} \\ \mathbf{T}_{ext,P} \end{Bmatrix} = \boldsymbol{\tau}_{GP}^T \mathbf{D}_B \boldsymbol{\tau}_{GP} \begin{Bmatrix} \mathbf{a}_P \\ \dot{\boldsymbol{\omega}} \end{Bmatrix} \tag{2.17}$$

Thus the transport of the direct dynamic model from the centre of mass G to a generic point of the structure P can be written as [3]:

$$\mathbf{D}_B^P = \boldsymbol{\tau}_{GP}^T \mathbf{D}_B \boldsymbol{\tau}_{GP} = \begin{bmatrix} m_B \mathbf{I}_3 & m_B [\mathbf{r}_{GP}]^\wedge \\ -m_B [\mathbf{r}_{GP}]^\wedge & \mathbf{J}_G^B - m_B ([\mathbf{r}_{GP}]^\wedge)^2 \end{bmatrix} \tag{2.18}$$

If the base and the appendages are separated, on each appendage the reaction forces $\mathbf{F}_{B/A}$ and the reaction torques $\mathbf{T}_{B/A,P}$ generated by the spacecraft's hub will act in correspondence of the connection point P.

By introducing the direct dynamic model of the single appendage $\mathbf{D}_A$ which is generally computed at the appendage centre of mass C, such dynamic model can be expressed at the connection point P using the transport model [3]:

$$\mathbf{D}_A^P = \boldsymbol{\tau}_{CP}^T \mathbf{D}_A \boldsymbol{\tau}_{CP} = \begin{bmatrix} \mathbf{I}_3 & [\mathbf{r}_{CP}]^\wedge \\ \mathbf{0}_3 & \mathbf{I}_3 \end{bmatrix}^T \begin{bmatrix} m_A \mathbf{I}_3 & \mathbf{0}_3 \\ \mathbf{0}_3 & \mathbf{J}_C^A \end{bmatrix} \begin{bmatrix} \mathbf{I}_3 & [\mathbf{r}_{CP}]^\wedge \\ \mathbf{0}_3 & \mathbf{I}_3 \end{bmatrix} \tag{2.19}$$

where $\mathbf{r}_{CP}$ is the position vector of the appendage centre of mass C with respect to the connection point P, m_A is the mass of the appendage and $\mathbf{J}_C^A$ is its inertia matrix with respect to C.

If no other forces nor torques act on the appendage, then the following relation can be obtained:

$$\begin{Bmatrix} \mathbf{F}_{B/A} \\ \mathbf{T}_{B/A,P} \end{Bmatrix} = \mathbf{D}_A^P \begin{Bmatrix} \mathbf{a}_P \\ \dot{\boldsymbol{\omega}} \end{Bmatrix} \tag{2.20}$$

Likewise, the spacecraft hub will experience the reaction forces $\mathbf{F}_{A/B} = -\mathbf{F}_{B/A}$ and the reaction torques $\mathbf{T}_{A/B,P} = -\mathbf{T}_{B/A,P}$ generated by each appendage, besides the external contributions acting on the structure. Therefore, the dynamic model of the base with respect to its centre of mass G can be expressed as [3]:

$$\begin{Bmatrix} \mathbf{F}_{ext} - \mathbf{F}_{B/A} \\ \mathbf{T}_{ext,G} - \mathbf{T}_{B/A,G} \end{Bmatrix} = \mathbf{D}_B \begin{Bmatrix} \mathbf{a}_G \\ \dot{\boldsymbol{\omega}} \end{Bmatrix} \tag{2.21}$$

and from the dynamic model $\mathbf{D}_A^G = \boldsymbol{\tau}_{PG}^T \mathbf{D}_A^P \boldsymbol{\tau}_{PG}$ of the appendage transported in G the following expression can be derived:

$$\begin{Bmatrix} \mathbf{F}_{ext} \\ \mathbf{T}_{ext,G} \end{Bmatrix} = (\mathbf{D}_B + \mathbf{D}_A^G) \begin{Bmatrix} \mathbf{a}_G \\ \dot{\boldsymbol{\omega}} \end{Bmatrix} \tag{2.22}$$

However, in the general case each appendage can rotate around a specific axis, which will be aligned to x-axis in both $\mathcal{R}_A$ and $\mathcal{R}_{SA}$ from the definition of such reference frames. The dynamic model $\mathbf{D}_A$ of the appendage is typically written in the frame $\mathcal{R}_{SA}$, which is rigidly attached to the appendage. Nevertheless, to obtain the dynamic model of the overall spacecraft expressed in the hub's centre of mass, the appendage dynamic model shall be considered in the frame $\mathcal{R}_A$, which on the contrary is fixed with respect to the hub. Since the two reference frames are coincident, with the only difference that $\mathcal{R}_{SA}$ is rotated around the x-axis by the rotation angle θ of the appendage with respect to $\mathcal{R}_A$, the following rotation matrix from frame $\mathcal{R}_{SA}$ to frame $\mathcal{R}_A$ can be introduced:

$$\mathbf{R}_x(\theta) = \begin{bmatrix} 1 & 0 & 0 \\ 0 & \cos\theta & \sin\theta \\ 0 & -\sin\theta & \cos\theta \end{bmatrix} \tag{2.23}$$

Therefore, the dynamic model of the appendage written with respect to the hub's centre of mass is expressed as:

$$\mathbf{D}_A^G = \boldsymbol{\tau}_{PG}^T \begin{bmatrix} \mathbf{R}_x(\theta) & \mathbf{0}_3 \\ \mathbf{0}_3 & \mathbf{R}_x(\theta) \end{bmatrix} \mathbf{D}_A^P \begin{bmatrix} \mathbf{R}_x(\theta) & \mathbf{0}_3 \\ \mathbf{0}_3 & \mathbf{R}_x(\theta) \end{bmatrix}^T \boldsymbol{\tau}_{PG} \tag{2.24}$$

Furthermore, the appendages are generally flexible bodies as opposed to the spacecraft base, which on the contrary is usually considered to be rigid. To take into account the flexibility of the structure, the cantilever hybrid model reported by Cumer and Chrétien in [8] is used, since the rigid and flexible contributions of the appendage can be considered separately. In particular, the dynamics of the single appendage can be described by the following equations [3]:

$$\begin{Bmatrix} \mathbf{F}_{B/A} \\ \mathbf{T}_{B/A,P} \end{Bmatrix} = \mathbf{D}_A^P \begin{Bmatrix} \mathbf{a}_P \\ \dot{\boldsymbol{\omega}} \end{Bmatrix} + \mathbf{L}_P^T \ddot{\boldsymbol{\eta}} \tag{2.25}$$

$$\ddot{\boldsymbol{\eta}} + \mathrm{diag}(2\xi_i\omega_i)\dot{\boldsymbol{\eta}} + \mathrm{diag}(\omega_i^2)\boldsymbol{\eta} = -\mathbf{L}_P \begin{Bmatrix} \mathbf{a}_P \\ \dot{\boldsymbol{\omega}} \end{Bmatrix} \tag{2.26}$$

where $\boldsymbol{\eta}$ is a vector with n components representing the modal coordinates of the flexible structure, ω_i, ξ_i, and $\mathbf{l}_P^i$ are the frequency, the damping ratio and the flexible contribution row vector of the i-th flexible mode expressed at point P. Matrix $\mathbf{L}_P \in \mathbb{R}^{n\times 6}$ is then defined as:

$$\mathbf{L}_P = \begin{bmatrix} \mathbf{l}_P^1 \\ \mathbf{l}_P^2 \\ \vdots \\ \mathbf{l}_i^n \end{bmatrix} \tag{2.27}$$

2.2 Solar array drive mechanism

The Solar Array Drive Mechanism (SADM) is a rotating mechanism that allows the solar array panels to be continuously tilted, in order to collect maximum sun power onto the solar cells. This mechanism is particularly important for the spacecraft to be provided with a steady energy supply. The main mechanical components of the SADM are the stepper motor – the electrical drive unit that generates the actual rotation – and the gearbox, which transmits the motor torque to the solar array. However, they also represent sources of disturbance, that may be dangerously magnified when coupling with the resonance frequencies of the solar array occurs.

The assembly of the two components is a purely torsional model and can thus be reduced to a system with only one degree of freedom. The angular acceleration and the torque around the SADM rotation axis is modified by the assembly model, whereas the other components bypass the assembly, affecting directly the spacecraft hub and the appendage.

2.2.1 Stepper motor model

The stepper motor is an electromechanical device converting electrical pulses to discrete mechanical rotation. The main characteristic of the stepper motor is its ability to translate switched excitation changes into precisely defined increments of rotor angular position, defined as steps or micro-steps.

In case the spacecraft is not rotating and the only movement is generated by the stepper motor, the rotation angle θ_r represents the solar array rotation around its axis. However, the global rotation of the rotor is due to the spacecraft motion as well. Therefore, the overall acceleration of the rotor, which is also the input shaft of the gearbox, can be written as [1]:

$$\ddot{\theta}_i = \ddot{\theta}_r + \dot{\omega}_x\big|_{\mathcal{R}_A} \tag{2.28}$$

where $\dot{\omega}_x\big|_{\mathcal{R}_A}$ is the component of the spacecraft angular acceleration $\dot{\boldsymbol{\omega}}$ projected along the solar array rotational axis, which coincides with the x-axis in the reference frame $\mathcal{R}_A$ rigidly attached to the appendage.

The torque generated by the stepper motor is dependent on a set of parameters which characterise such device and can be described by the following equation [1]:

$$T_m = K_m I \gamma i \tag{2.29}$$

where K_m is the motor torque constant, I is the amplitude of the two-phase current of the stepper motor, γ is defined as the electrical micro-step angle, and i is an integer value that depends on the reference angle of the rotor which represents the desired configuration and is thus the input of the system. In addition, by considering the stiffness and the damping contributions of the stepper motor, the overall torque acting on the spacecraft hub can be computed as [1]:

$$T_{r/HUB} = -T_m + C_0\dot{\theta}_r + K_0\theta_r \tag{2.30}$$

where $K_0 = K_m I z$ is defined as the electromagnetic stiffness, z is the rotor teeth number, and C_0 is the viscous damping coefficient of the motor.

The dynamics of the rotor can then be described by the following equation [1]:

$$J_r\ddot{\theta}_i = T_{i/r} + T_{HUB} \tag{2.31}$$

where J_r is the inertia of the rotor, $T_{i/r}$ represents the torque produced by the gearbox and acting of the motor, and $T_{HUB} = -T_{r/HUB}$ is the torque generated by the spacecraft hub on the rotor around the direction of the solar array rotational axis.

2.2.2 Gearbox model

Between the stepper motor and the solar array, a gearbox is present in order to provide both angular velocity and torque conversion. The velocity of the rotor is usually reduced to attain the desired angular rate of the solar panel, while the torque generated by the motor is generally amplified. As in case of the stepper motor, the gearbox model will be purely torsional with a single rotational degree of freedom around the longitudinal axis of the input and output shafts, whose inertia is denoted J_i and J_o respectively.

The gearbox ratio, or transmission ratio N_g, is introduced and defined as the ratio of the angular velocity of the input shaft $\dot{\theta}_i$ to the angular velocity of the output shaft $\dot{\theta}_o$. However, due to the stiffness of the gearbox, the output shaft experiences an additional deflection with respect to the expected output angular position, that can be expressed as [1]:

$$\delta\theta = \theta_o - \frac{\theta_i}{N_g} \tag{2.32}$$

In case the deflection could be neglected it is easy to verify that the previous definition of the gearbox ratio is retrieved.

The torsional torques acting on the input shaft of the gearbox are generated by the rotor of the stepper motor $T_{r/i} = -T_{i/r}$ on one side and the torque produced by the main body of the gearbox itself $T_{g/i}$ on the other side. The dynamics of the input shaft can then be expressed as [1]:

$$J_i\ddot{\theta}_i = -T_{i/r} - T_{g/i} \tag{2.33}$$

The main structure of the gearbox is considered to be massless, and the its stiffness and viscous damping are denoted K_g and C_g respectively. Its entire dynamics is not completely negligible due to its stiffness that in turn generated the angular deflection on the output shaft $\delta\theta$ and is described by the following relation [1]:

$$C_g\delta\dot{\theta} + K_g\delta\theta = T_{PERT} + T_{g/o} \tag{2.34}$$

where the torque T_{PERT} is the harmonic disturbance produced by one or more contact damage frequencies in the gear pairs inside the gearbox main body. Such disturbance may be dangerously magnified if coupling with the natural frequencies of the solar array and thus might lead to pointing accuracy degradation. The characterisation of the disturbance and the techniques for accurate estimation of T_{PERT} will be treated in the next chapters.

In addition, the dynamics of the gearbox depends on the quantity $T_{g/o}$, which is the torque produced by the gearbox and acting on the output shaft connected to the solar array. The value of $T_{g/o}$ can also be derived from the gearbox ratio as:

$$T_{g/o} = N_g T_{g/i} \tag{2.35}$$

To conclude, the dynamics of the output shaft can be described by the following expression [1]:

$$J_o\ddot{\theta}_o = T_{g/o} + T_{SA/o} \tag{2.36}$$

where $T_{SA/o}$ is the torsional torque generated by the solar array and acting on the output shaft of the gearbox.

2.2.3 Augmented satellite dynamic toolbox

The satellite dynamics toolbox can be integrated with the model of the solar array drive mechanism to obtain a more powerful tool named SDT+ with additional capability to include the dynamics of the mechanisms that allow the rotation of the appendages.

Such tool can be used to model and simulate the overall dynamics of a spacecraft, including the input command of the stepper motor and the perturbations generated by the single subsystems, as well as the global frequency response of the body.

In addition, it can be specialised to any specific configuration and further generalised to encompass any finite number of flexible and/or rotating appendages, connected to the spacecraft main body at any point of the structure.

As an example, Figure 2.2 shows a block diagram representation of the SDT+ model with a solar array as the only appendage. Each block includes the dynamic model of a specific subsystem.

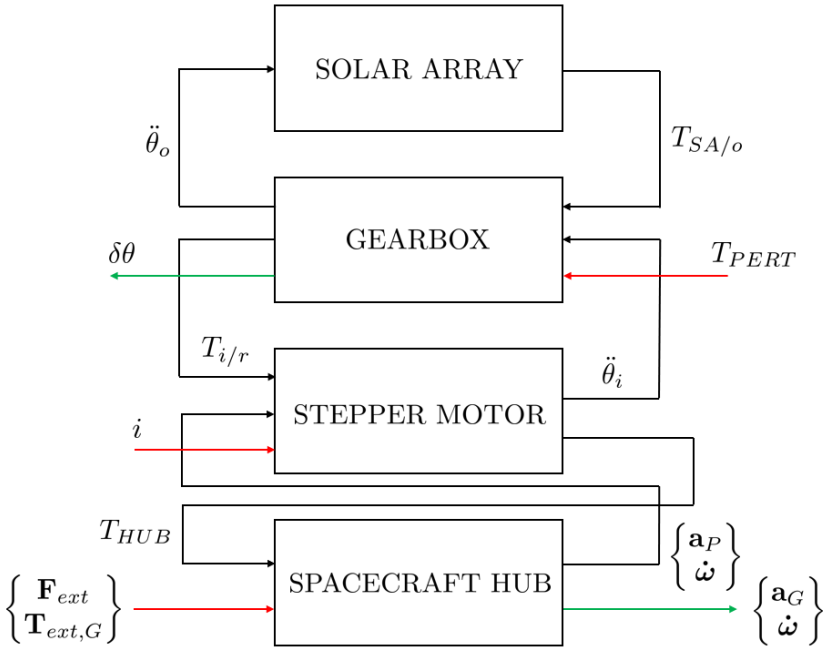

Figure 2.2: Example of SDT+ block diagram

2.3 Sentinel-2 mathematical model

Sentinel-2 is an Earth observation mission within the Copernicus program of the European Space Agency and the European Commission for global land monitoring at high resolution. The mission provides data on vegetation, soil, water and atmosphere by delivering images in 13 spectral bands, including the visible and the near-infrared.

Sentinel-2 is able to distinguish between different crop types and generates information about changes in land cover as well as pollution in lakes and coastal waters, floods, volcanic eruptions and landslides monitoring. In addition, the mission has been designed to have high temporal resolution, with a geometric revisit time of 5 days in order to make meaningful information rapidly available to users.

The mission is a constellation of two equally spaced twin satellites on the same orbit, Sentinel-2A and Sentinel-2B. The orbit is sun-synchronous to guarantee the same illumination angle on the planet while performing the imaging acquisition, and allowing seamless combination of provided information with historical data. Table 2.1 contains some orbital information for the two spacecrafts.

	Orbital parameter	Value
a	Semi-major axis [km]	7173
e	Eccentricity [-]	0.0013
i	Inclination [deg]	98.62
Ω	RAAN [deg]	293.66
ω	Perigee argument [deg]	109.86
T	Orbital period [min]	100.6

Table 2.1: Sentinel-2 orbital parameters

The satellite structure is shown in Figure 2.3 and it is made up of two main components, i.e. the hub and the solar array. The solar array is equipped with a SADM that allows the panel to be tilted continuously during the orbit, in order to collect maximum sun power onto the solar cells. Moreover, the solar array is designed to operate in two different modes, namely the forward mode when the sun is visible with respect to the spacecraft, and a more rapid rewind mode during eclipse to recover the initial configuration. The solar array configuration over time is depicted in Figure 2.4 and depends on the angle $\theta(t)$ which represents the rotation of the appendage – and thus of frame $\mathcal{R}_{SA}$ – with respect to the reference frame $\mathcal{R}_A$ rigidly attached to the satellite rigid base (see also Figure 2.1).

From knowledge of Sentinel-2A geometrical and inertial properties as well as information about the solar array and the relative driving mechanism, the satellite dynamics can be modelled using the SDT+ previously described. In particular, Figure 2.5 shows the kinematic model of the Sentinel-2 gearbox with its main components, which will be also used to characterise the perturbations generated during the operation.

The overall SDT+ model specialised to the Sentinel-2A structure is shown in Figure 2.7. The dynamics of each subsystem composing the satellite is included and the equations of motions derived in the previous section are combined and connected to each other to reconstruct the global motion of the spacecraft. This block representation is particularly useful, since the relations of the single quantities are easily retrievable and can be computed by means of simple sums and multiplications.

Figure 2.3: Sentinel-2A model [31]

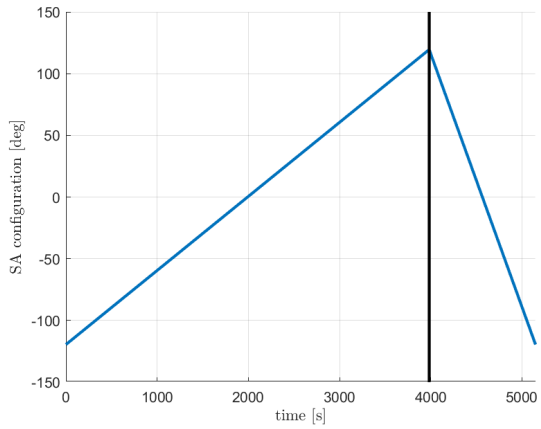

Figure 2.4: Sentinel-2 solar array configuration over one orbit

Furthermore, from the dynamic model of Sentinel-2A generated by the SDT+ it is possible to carry out further analysis. For instance, Figure 2.6 shows the frequency response of the spacecraft structure as described by the corresponding singular values. The different peaks represent the natural frequency of the overall satellite as well as the flexible frequencies of the solar array. In particular, the response is computed by considering both the stepper motor and the perturbation generated by the gearbox as the input to the angular accelerations $\dot{\boldsymbol{\omega}}$. Since the satellite dynamics depends on the rotation angle $\theta(t)$ of the solar array, the frequency response slightly differs over time and more responses are depicted to show the behaviour of the structure in different configurations. In addition, it is clearly visible that the frequency response from the gearbox is more relevant at almost every frequency, and will dominate the spacecraft dynamics with respect to the motor response. Therefore, the response of the stepper motor will be neglected in the following, and the present study will only focus on the estimation on the disturbance generated by the gearbox.

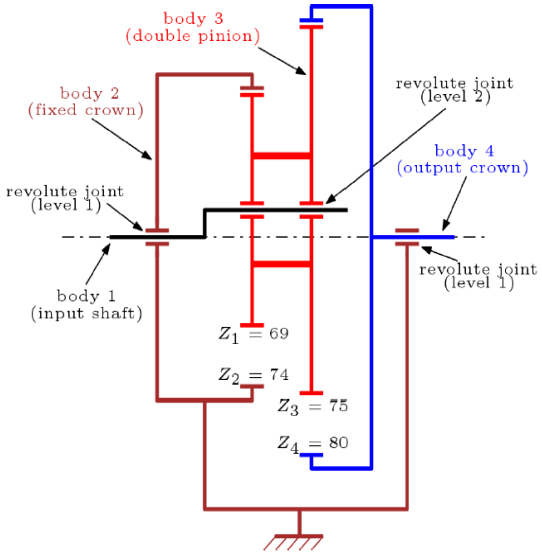

Figure 2.5: Sentinel-2 gearbox kinematic model [1]

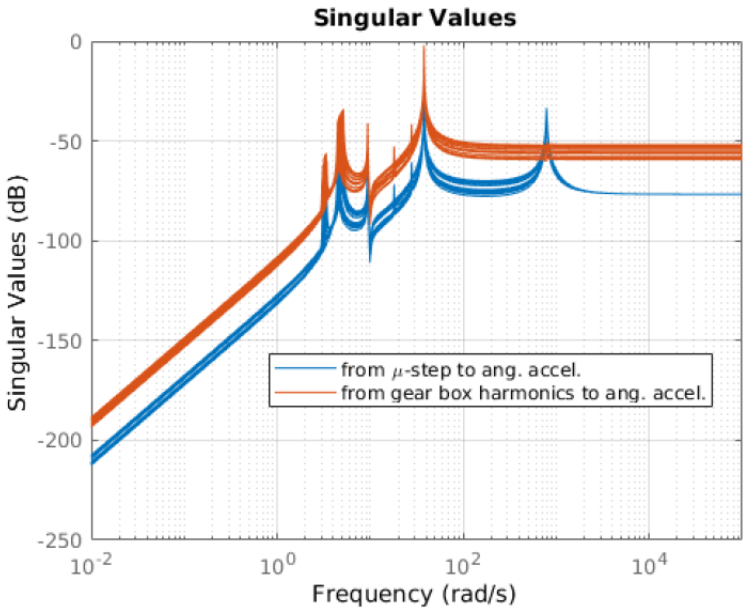

Figure 2.6: Sentinel-2 gearbox and stepper motor frequency response [1]

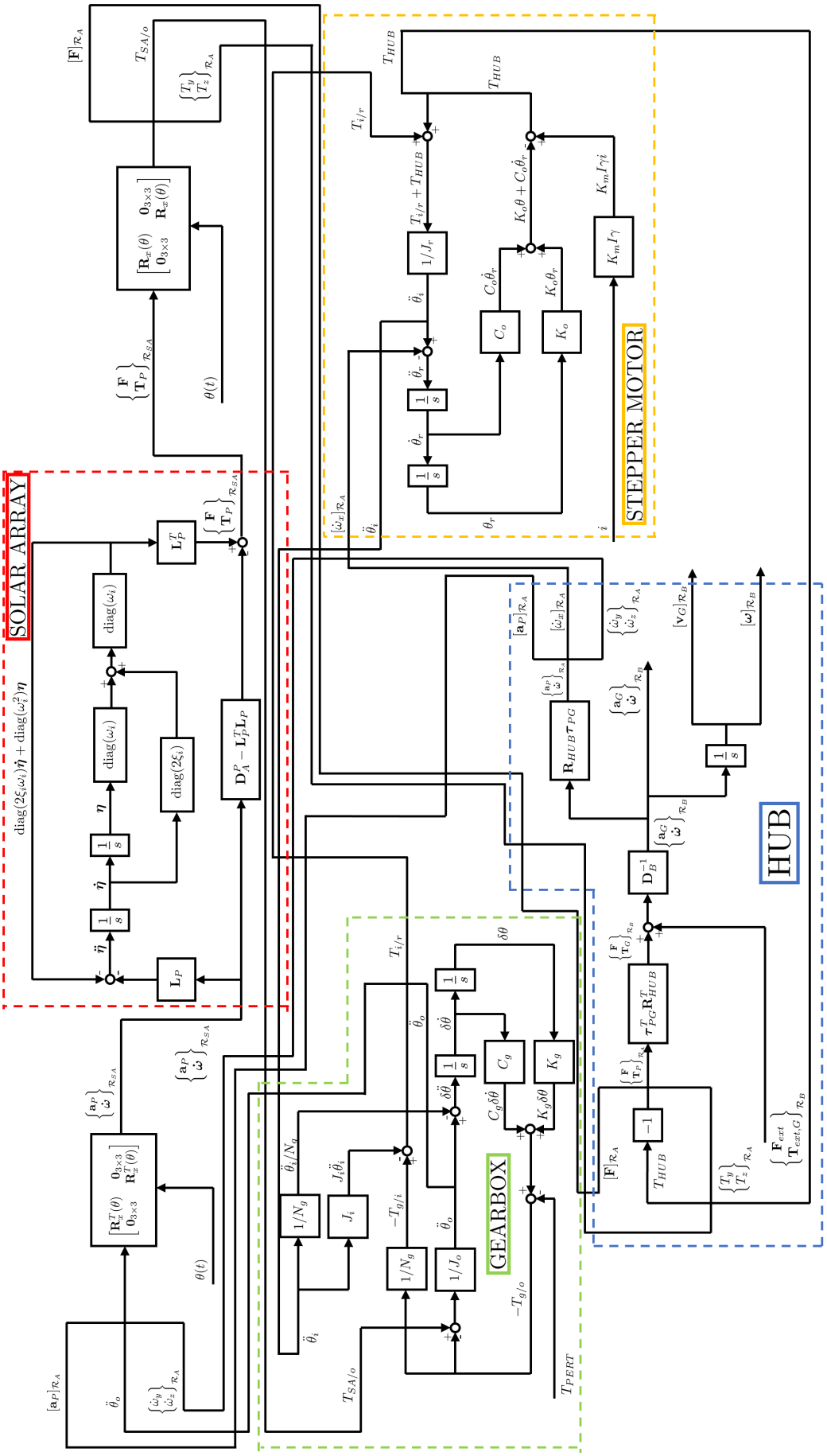

Figure 2.7: Sentinel-2A dynamics block diagram representation

Chapter 3

Linear $\mathcal{H}_\infty$ control theory

3.1 Review of linear systems representation

LINEAR Time-Invariant (LTI) dynamical systems can be described using a state-space representation in the time domain or equivalently in the frequency domain, by introducing a transfer function which depends on the complex variable $s = \sigma + j\omega$. Modern control theory makes use of the former technique for the design of the controller. A state vector $\mathbf{x}(t) \in \mathbb{R}^n$ is defined according to the system variables and the overall dynamic system is described by a set of n first-order differential equations [18]:

$$\dot{\mathbf{x}}(t) = \mathbf{A}\mathbf{x}(t) + \mathbf{B}_u\mathbf{u}(t) + \mathbf{B}_w\mathbf{w}(t) \tag{3.1}$$

$$\mathbf{y}(t) = \mathbf{C}_y\mathbf{x}(t) + \mathbf{D}_{yu}\mathbf{u}(t) + \mathbf{D}_{yw}\mathbf{w}(t) \tag{3.2}$$

$$\mathbf{z}(t) = \mathbf{C}_z\mathbf{x}(t) + \mathbf{D}_{zu}\mathbf{u}(t) + \mathbf{D}_{zw}\mathbf{w}(t) \tag{3.3}$$

where:

- $\mathbf{u}(t) \in \mathbb{R}^{n_u}$ is the input control vector formed by controllable variables used to regulate in some way the dynamic response of the system such that it exhibits a desired dynamic behaviour;
- $\mathbf{w}(t) \in \mathbb{R}^{n_w}$ is the input disturbance vector encompassing the exogenous or environmental variables acting on the system, that are responsible of exciting the system in an undesired manner;
- $\mathbf{y}(t) \in \mathbb{R}^{n_y}$ includes the measured output variables, which are physical quantities measured by sensors and representing the system response as perceived by an observer;
- $\mathbf{z}(t) \in \mathbb{R}^{n_z}$ encompasses performance variables, which are quantities related to a performance measure of the system response and typically introduced as error output to be minimised when a control system is to be designed;
- $\mathbf{A} \in \mathbb{R}^{n\times n}$ is the system state matrix;
- $\mathbf{B}_u \in \mathbb{R}^{n\times n_u}$ is the input matrix, in which the i-th column refers to the influence vector of the i-th control input;
- $\mathbf{B}_w \in \mathbb{R}^{n\times n_w}$ is the disturbance matrix, in which the i-th refers to the influence vector of the i-th disturbance input;

- $\mathbf{C}_y \in \mathbb{R}^{n_y \times n}$ is the output matrix, in which the i-th row refers to the i-th output variable;
- $\mathbf{C}_z \in \mathbb{R}^{n_z \times n}$ is the performance matrix, in which the i-th row refers to i-th performance variable;
- $\mathbf{D}_{yu} \in \mathbb{R}^{n_y \times n_u}$ is the direct feedthrough matrix, in which the element (i, j) refers to the direct feedthrough term of the j-th control input on the i-th output;
- $\mathbf{D}_{yw} \in \mathbb{R}^{n_y \times n_w}$ is the disturbance feedthrough matrix, in which the element (i, j) refers to the direct feedthrough term of the j-th exogenous input on the i-th output;
- $\mathbf{D}_{zu} \in \mathbb{R}^{n_z \times n_u}$ is the direct feedthrough matrix of the performance, in which the element (i, j) refers to the direct feedthrough term of the j-th control input on the i-th performance variable;
- $\mathbf{D}_{zw} \in \mathbb{R}^{n_z \times n_w}$ is the disturbance direct feedthrough matrix of the performance, in which the element (i, j) refers to the j-th exogenous input on the i-th performance variable.

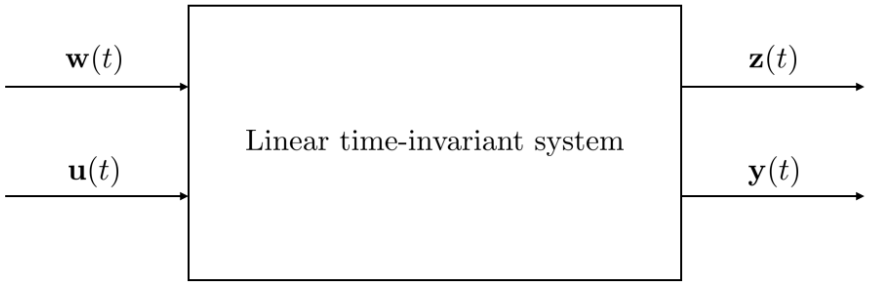

Figure 3.1: General linear time-invariant system block diagram

In contrast to modern control theory, classical control theory relies on the Laplace transform, which converts a function of time t to a function of the complex variable $s = \sigma + j\omega$ as follows [12]:

$$f(s) = \mathcal{L}[f(t)] = \int_{-\infty}^{+\infty} f(t)e^{-st}\, dt \tag{3.4}$$

In case the complex variable s has only imaginary part (i.e., $\sigma = 0$), the Laplace transform reduces to the Fourier transform [12]:

$$f(j\omega) = \mathcal{F}[f(t)] = \int_{-\infty}^{+\infty} f(t)e^{-j\omega t}\, dt \tag{3.5}$$

The main difference between the two transforms lies in the fact that Laplace transforms can be used to study the complete response characteristics of feedback systems, including transient response. On the other hand, Fourier transforms mainly involve steady-state response of the system.

The transfer function $\mathbf{G}(s)$ of a system is defined as the ratio between the Laplace transform of the system output $\mathbf{y}(s)$ and the Laplace transform of the system input

$\mathbf{u}(s)$ with zero initial conditions. In general, when inputs and outputs are multiple, the transfer function is a $n_y \times n_u$ matrix:

$$\mathbf{y}(s) = \mathbf{G}(s)\mathbf{u}(s) \tag{3.6}$$

The transfer function can be inferred from the state-state representation of the system, by applying the Laplace transform to the state equation and substituting it in the output equation (a single input vector including controllable and exogenous variables is here considered) [18]:

$$\mathbf{G}(s) = \mathbf{C}(s\mathbf{I} - \mathbf{A})^{-1}\mathbf{B} + \mathbf{D} \tag{3.7}$$

In addition, the system equation and the output equation can be written in a more compact form as:

$$\begin{Bmatrix} \dot{\mathbf{x}}(t) \\ \mathbf{y}(t) \end{Bmatrix} = \begin{bmatrix} \mathbf{A} & \mathbf{B} \\ \mathbf{C} & \mathbf{D} \end{bmatrix} \begin{Bmatrix} \mathbf{x}(t) \\ \mathbf{u}(t) \end{Bmatrix} \tag{3.8}$$

Furthermore, the following additional notation is introduced for the system transfer function [34]:

$$\mathbf{G}(s) = \left[\begin{array}{c|c} \mathbf{A} & \mathbf{B} \\ \hline \mathbf{C} & \mathbf{D} \end{array}\right] = \mathbf{C}(s\mathbf{I} - \mathbf{A})^{-1}\mathbf{B} + \mathbf{D} \tag{3.9}$$

3.1.1 Controllability and observability

A system is said to be controllable if and only if it is possible, by means of the input $\mathbf{u}(t)$, to transfer the system from any initial state $\mathbf{x}(t_0)$ to any other state $\mathbf{x}(T)$ in a finite time interval $T - t_0 \geq 0$.

In other words, controllability explores the interaction between input and state, seeking to characterise the extent to which state trajectories can be controlled by piecewise continuous input signals over a finite interval of time.

For linear systems, controllability can be checked by evaluating the rank of the controllability matrix $\mathcal{C}$, which is defined as [18]:

$$\mathcal{C} = \begin{bmatrix} \mathbf{B} & \mathbf{AB} & \mathbf{A}^2\mathbf{B} & \dots & \mathbf{A}^{n-1}\mathbf{B} \end{bmatrix} \tag{3.10}$$

In particular, the pair $(\mathbf{A}, \mathbf{B})$ is said to be controllable if and only if $\text{rank}(\mathcal{C}) = n$. If $\mathcal{C}$ is not full rank, the system is said to be uncontrollable and the subspace spanned by its columns defines the controllable subsystem.

Alternatively, the degree of controllability of a linear system can be evaluated by introducing the controllability grammian $\mathbf{W}_c$ and checking whether it is strictly positive definite for any t [18]:

$$\mathbf{W}_c = \int_0^t e^{\mathbf{A}\tau}\mathbf{B}\mathbf{B}^T e^{\mathbf{A}^T\tau} d\tau \tag{3.11}$$

An unforced system is said to be observable if and only if it is possible to determine any state $\mathbf{x}(t)$ by using only a finite record $\mathbf{y}(\tau)$ for $t \leq \tau \leq T$ of the output.

The idea of observability relies on whether or not measurements of the output signals over a finite time interval can be processed in order to uniquely determine the state of the system.

For linear systems, observability can be checked by evaluating the rank of the observability matrix $\mathcal{O}$, which is defined as [18]:

$$\mathcal{O} = \begin{bmatrix} \mathbf{C} \\ \mathbf{CA} \\ \mathbf{CA}^2 \\ \vdots \\ \mathbf{CA}^{n-1} \end{bmatrix} \tag{3.12}$$

In particular, the pair $(\mathbf{A}, \mathbf{C})$ is said to be observable if and only if $\text{rank}(\mathcal{O}) = n$. If $\mathcal{O}$ is not full rank, the system is said to be unobservable and the subspace spanned by its columns defines the observable subsystem.

Analogously to the controllability case, the degree of observability of a linear system can be evaluated by introducing the observability grammian $\mathbf{W}_o$ and checking whether it is strictly positive definite for any t [18]:

$$\mathbf{W}_o = \int_0^t e^{\mathbf{A}^T\tau}\mathbf{C}^T\mathbf{C}e^{\mathbf{A}\tau}d\tau \tag{3.13}$$

If a system contains an uncontrollable subsystem it is said to be uncontrollable. Similarly, if a system contains an unobservable subsystem it is said to be unobservable. A distinction is introduced between an uncontrollable (unobservable) system in which the uncontrollable (unobservable) part is stable and a system in which the uncontrollable (unobservable) part is unstable.

In particular, if the uncontrollable part is stable, the system is said to be stabilizable.

Likewise, if the unobservable subsystem is stable, the overall system is said to be detectable.

3.2 Singular values and $\mathcal{H}_\infty$ norm

Singular Value Decomposition (SVD) of a matrix is a factorisation that generalises the decomposition of a square matrix by means of eigenvalues and eigenvectors to any rectangular matrix by introducing the singular values σ_i.

It can be demonstrated that any complex matrix $\mathbf{A} \in \mathbb{R}^{m\times n}$ can be decomposed as the product of a rectangular diagonal matrix $\mathbf{\Sigma}$ and two unitary ($\mathbf{U}^*\mathbf{U} = \mathbf{U}\mathbf{U}^* = \mathbf{I}$) square matrices $\mathbf{U}$ and $\mathbf{V}^*$, where the superscript * denotes the conjugate transpose (i.e., transpose of the matrix and complex conjugate of each entry) in the following order [34]:

$$\mathbf{A} = \mathbf{U}\mathbf{\Sigma}\mathbf{V}^* \tag{3.14}$$

In particular:

$$\mathbf{U} = \begin{bmatrix} \mathbf{u}_1 & \mathbf{u}_2 & \dots & \mathbf{u}_m \end{bmatrix} \in \mathbf{R}^{m\times m} \tag{3.15}$$

$$\mathbf{V} = \begin{bmatrix} \mathbf{v}_1 & \mathbf{v}_2 & \dots & \mathbf{v}_n \end{bmatrix} \in \mathbf{R}^{n\times n} \tag{3.16}$$

$$\mathbf{\Sigma} = \begin{bmatrix} \mathbf{\Sigma}_1 & \mathbf{0} \\ \mathbf{0} & \mathbf{0} \end{bmatrix} \in \mathbf{R}^{m\times n} \tag{3.17}$$

$$\mathbf{\Sigma}_1 = \begin{bmatrix} \sigma_1 & 0 & ... & 0 \\ 0 & \sigma_2 & ... & 0 \\ \vdots & \vdots & \ddots & \vdots \\ 0 & 0 & ... & \sigma_p \end{bmatrix} \in \mathbf{R}^{p \times p} \tag{3.18}$$

Matrix $\mathbf{A}$ does not possess a unique SVD, however it is usually decomposed such that the entries in matrix $\mathbf{\Sigma}$ are ordered in a decreasing fashion:

$$\sigma_1 \geq \sigma_2 \geq ... \geq \sigma_p \geq 0, \quad p = \min(n, m) \tag{3.19}$$

Following the singular value decomposition, p quantities σ_i are obtained, which are called singular values of matrix $\mathbf{A}$. The columns of $\mathbf{U}$ and the columns of $\mathbf{V}$ are respectively the left singular vectors and the right singular vectors of $\mathbf{A}$. By passing from the matrix to a vector notation, it can be verified that:

$$\mathbf{A}\mathbf{v}_i = \sigma_i \mathbf{u}_i \tag{3.20}$$
$$\mathbf{A}^* \mathbf{u}_i = \sigma_i \mathbf{v}_i \tag{3.21}$$

By taking the inverse of $\mathbf{A}^*$ to obtain $\mathbf{u}_i$ in the second equation and substituting in the first equation (the same approach can be performed in the reversed order) the above equations can be written as:

$$\mathbf{A}^*\mathbf{A}\mathbf{v}_i = \sigma_i^2 \mathbf{v}_i \tag{3.22}$$
$$\mathbf{A}\mathbf{A}^*\mathbf{u}_i = \sigma_i^2 \mathbf{u}_i \tag{3.23}$$

The last expressions prove that the squared singular value σ_i^2 is both an eigenvalue of $\mathbf{A}^*\mathbf{A}$ with corresponding eigenvector $\mathbf{v}_i$, and an eigenvalue of $\mathbf{A}\mathbf{A}^*$ associated to the eigenvector $\mathbf{u}_i$. Thus, the singular value σ_i of matrix $\mathbf{A}$ can also be defined as the square root of the non-negative eigenvalues of matrices $\mathbf{A}^*\mathbf{A}$ and $\mathbf{A}\mathbf{A}^*$.

To denote the largest and the smallest singular values, the following notations are typically used:

$$\overline{\sigma}(\mathbf{A}) = \sigma_{max}(\mathbf{A}) = \sigma_1 \rightarrow \text{largest singular value of } \mathbf{A}$$
$$\underline{\sigma}(\mathbf{A}) = \sigma_{min}(\mathbf{A}) = \sigma_p \rightarrow \text{smallest singular value of } \mathbf{A}$$

Geometrically, the singular value decomposition of a real matrix $\mathbf{A}$ can be seen as the linear transformation of of the unit sphere in $\mathbb{R}^m$ into a hyperellipsoid in $\mathbb{R}^m$ which is obtained by stretching the unit sphere by the factors σ_1, σ_2, ..., σ_m (possibly zero) in the orthogonal directions defined by $\mathbf{u}_1$, $\mathbf{u}_2$, ..., $\mathbf{u}_m$. Vectors $\sigma_i \mathbf{u}_i$ are the principal semi-axes of the hyperellipsoid, with lengths σ_1, σ_2, ..., σ_m. If $\mathbf{A}$ has rank p, exactly p of the lengths σ_i will turn out to be nonzero.

In the simple case $\mathbf{A} \in \mathbb{R}^{2\times 2}$, the SVD factorises matrix $\mathbf{A}$ as:

$$\mathbf{A} = \begin{bmatrix} \cos\theta_1 & -\sin\theta_1 \\ \sin\theta_1 & \cos\theta_1 \end{bmatrix} \begin{bmatrix} \sigma_1 & 0 \\ 0 & \sigma_2 \end{bmatrix} \begin{bmatrix} \cos\theta_2 & -\sin\theta_2 \\ \sin\theta_2 & \cos\theta_2 \end{bmatrix} \tag{3.24}$$

The geometrical representation of the SVD is represented in Figure 3.2.

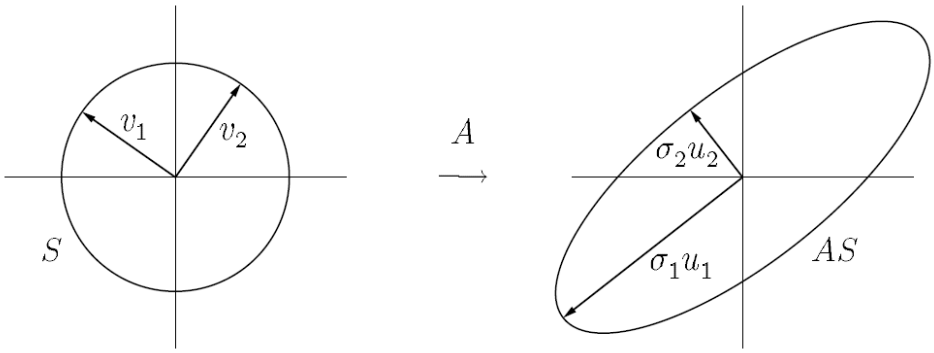

Figure 3.2: Singular value decomposition - geometrical representation [30]

From the control theory point of view, the unit vector $\mathbf{v}_1$ is the highest gain input (or control) direction, while $\mathbf{u}_1$ is the highest gain output (or observing) direction. In a similar fashion, $\mathbf{v}_n$ represents the lowest gain input direction, while $\mathbf{u}_m$ is the lowest gain output direction.

This result is particularly useful in case the LTI dynamical system under study has multiple inputs and/or outputs in order to minimise the highest gain direction. This is strictly connected to the idea of the $\mathcal{H}_\infty$ norm of a system's transfer function, which is defined as [4]:

$$||\mathbf{G}||_\infty = \sup_\omega \overline{\sigma}(\mathbf{G}(j\omega)) \tag{3.25}$$

The $\mathcal{H}_\infty$ norm scans the largest singular value of the transfer function $\mathbf{G}(j\omega)$ over all the frequency domain and returns the peak value that $\overline{\sigma}(\mathbf{G}(j\omega))$ achieves, which – in case the system inputs are exogenous variables whose effects shall be cancelled – represents the worst-case scenario, i.e. the highest gain direction that the combinations of the external disturbances can generate.

In other words, when the transfer function $G(s)$ represents a single-input and single-output linear system, the $\mathcal{H}_\infty$ norm can be regarded as the largest possible amplification factor of the system's steady-state response to sinusoidal excitations. For instance, the steady-state response of the system with respect to a sinusoidal input $u(t) = U \sin(\omega_0 t + \varphi)$ is [34]:

$$y(t) = U|G(j\omega_0)| \sin(\omega_0 t + \varphi + \angle G(j\omega_0)) \tag{3.26}$$

and thus the largest possible amplification factor is $\sup_{\omega_0} \overline{\sigma}(G(j\omega))$, which is precisely the $\mathcal{H}_\infty$ norm of the transfer function.

Similarly, in the multiple-input and multiple-output case, the $\mathcal{H}_\infty$ norm of a matrix transfer function $\mathbf{G}(s)$ can also be considered as the largest possible amplification factor of the system's steady-state response to sinusoidal excitations. The sinusoidal inputs can be written as:

$$\mathbf{u}(t) = \begin{bmatrix} u_1 \sin(\omega_0 t + \varphi_1) \\ u_2 \sin(\omega_0 t + \varphi_2) \\ \vdots \\ u_n \sin(\omega_0 t + \varphi_n) \end{bmatrix} \quad \hat{\mathbf{u}} = \begin{bmatrix} u_1 \\ u_2 \\ \vdots \\ u_n \end{bmatrix} \tag{3.27}$$

Then the steady-state response of the system can be written as:

$$\mathbf{y}(t) = \begin{bmatrix} y_1 \sin(\omega_0 t + \theta_1) \\ y_2 \sin(\omega_0 t + \theta_2) \\ \vdots \\ y_m \sin(\omega_0 t + \theta_m) \end{bmatrix} \quad \hat{\mathbf{y}} = \begin{bmatrix} y_1 \\ y_2 \\ \vdots \\ y_m \end{bmatrix} \tag{3.28}$$

for some y_i and θ_i that depend on the transfer function. Furthermore, the $\mathcal{H}_\infty$ norm can be defined as [34]:

$$||\mathbf{G}||_\infty = \sup_{\omega_0, \varphi_i, \hat{\mathbf{u}}} \frac{||\hat{\mathbf{y}}||}{||\hat{\mathbf{u}}||} \tag{3.29}$$

where $||\cdot||$ is the Euclidian norm.

3.3 Algebraic Riccati equations

Algebraic Riccati Equations (AREs) are a type of nonlinear matrix equation that is particularly recurrent in system control synthesis. For instance, an approach for the computation of the $\mathcal{H}_\infty$ control requires the solution of two AREs are required. The general algebraic Riccati equation can be written as follows [34]:

$$\mathbf{A}^*\mathbf{X} + \mathbf{X}\mathbf{A} + \mathbf{X}\mathbf{R}\mathbf{X} + \mathbf{Q} = \mathbf{0} \tag{3.30}$$

where $\mathbf{A}$, $\mathbf{R}$, and $\mathbf{Q}$ are $n \times n$ known matrices, with $\mathbf{R}$ and $\mathbf{Q}$ symmetric, while the unknown to be determined is the symmetric matrix $\mathbf{X}$. To solve such problem, the $2n \times 2n$ Hamiltonian matrix $\mathbf{H}$ associated with the general Riccati equation is introduced [34]:

$$\mathbf{H} = \begin{bmatrix} \mathbf{A} & \mathbf{R} \\ -\mathbf{Q} & -\mathbf{A}^* \end{bmatrix} \tag{3.31}$$

The Hamiltonian matrix $\mathbf{H}$ has the property to have its eigenvalues symmetric with respect to the imaginary axis. This statement can be easily proved by introducing a second $2n \times 2n$ matrix $\mathbf{J}$ defined as [34]:

$$\mathbf{J} = \begin{bmatrix} \mathbf{0} & -\mathbf{I}_n \\ \mathbf{I}_n & \mathbf{0} \end{bmatrix} \tag{3.32}$$

By making use of the structure of $\mathbf{J}$, it can be obtained that $\mathbf{J}^2 = \mathbf{J} \cdot \mathbf{J} = -\mathbf{I}_{2n}$. Therefore:

$$\mathbf{J}^{-1}\mathbf{H}\mathbf{J} = \mathbf{I}_{2n} \cdot \mathbf{J}^{-1}\mathbf{H}\mathbf{J} = \mathbf{J}\mathbf{J}^{-1} \cdot \mathbf{J}^{-1}\mathbf{H}\mathbf{J} = -\mathbf{J}\mathbf{H}\mathbf{J} = -\mathbf{H}^* \tag{3.33}$$

which means that $\mathbf{H}$ and $-\mathbf{H}^*$ are similar, and then they must share the same eigenvalues. Thus, λ is an eigenvalue of $\mathbf{H}$ (and of $-\mathbf{H}^*$) if and only if $-\overline{\lambda}$ is as well.

Assuming that $\mathbf{H}$ has no eigenvalues on the imaginary axis, the above consideration entails that $\mathbf{H}$ has n eigenvalues with $\mathrm{Re}(s) > 0$ and n eigenvalues with $\mathrm{Re}(s) < 0$. The eigenvectors $\mathbf{x}_1$, $\mathbf{x}_2$, ..., $\mathbf{x}_n \in \mathbb{C}^{2n}$ associated to the eigenvalues of the latter type form a basis for the stable invariant subspace, and can be used to find a solution for the algebraic Riccati equation. In particular, a new matrix can be formed by gathering the above-mentioned stable eigenvectors, that in turn can be partitioned into two submatrices $\mathbf{X}_1$ and $\mathbf{X}_2$ with dimensions $n \times n$ as follows:

$$\begin{bmatrix}\mathbf{v}_1 & \mathbf{v}_2 & \dots & \mathbf{v}_n\end{bmatrix} = \begin{bmatrix}\mathbf{X}_1 \\ \mathbf{X}_2\end{bmatrix} \tag{3.34}$$

If $\mathbf{X}_1$ is nonsingular, then the solution of the general ARE is obtained as [34]:

$$\mathbf{X} = \mathbf{X}_2\mathbf{X}_1^{-1} \tag{3.35}$$

The last relation proves that the stabilising solution of the algebraic Riccati equation $\mathbf{X}$ is uniquely determined by the associated Hamiltonian matrix $\mathbf{H}$. In other words, a function $\mathbf{X} = \mathrm{Ric}(\mathbf{H})$ can be introduced to express such result. In addition, the condition $\mathbf{H} \in \mathrm{dom}(\mathrm{Ric})$ will denote that matrix $\mathbf{H}$ has no eigenvalues on the imaginary axis.

To sum up, it can be demonstrated that if $\mathbf{H} \in \mathrm{dom}(\mathrm{Ric})$ and $\mathbf{X} = \mathrm{Ric}(\mathbf{H})$, then:

- $\mathbf{X}$ is real and symmetric;
- $\mathbf{X}$ satisfies the algebraic Riccati equation:

$$\mathbf{A}^*\mathbf{X} + \mathbf{X}\mathbf{A} + \mathbf{X}\mathbf{R}\mathbf{X} + \mathbf{Q} = \mathbf{0};$$

- $\mathbf{A} + \mathbf{R}\mathbf{X}$ is stable.

3.4 Linear fractional transformation

A Linear Fractional Transformation (LFT) is a mapping in the complex domain of the form [34]:

$$F(s) = \frac{a + bs}{c + ds} \tag{3.36}$$

where a, b, c, and $d \in \mathbb{C}$ are complex scalars. In other words, a linear fractional transformation is a transformation that is represented by a fraction whose numerator and denominator are linear.

The linear fractional transformation defined above for scalars can be generalised to the matrix case. To derive the LFT involving matrices, a complex matrix $\mathbf{G}$ is introduced and partitioned as follows:

$$\mathbf{G} = \begin{bmatrix}\mathbf{G}_{11} & \mathbf{G}_{12} \\ \mathbf{G}_{21} & \mathbf{G}_{22}\end{bmatrix} \in \mathbb{C}^{(n_z+n_y)\times(n_w+n_u)} \tag{3.37}$$

with $\mathbf{G}_{11} \in \mathbb{C}^{n_z\times n_w}$, $\mathbf{G}_{12} \in \mathbb{C}^{n_z\times n_u}$, $\mathbf{G}_{21} \in \mathbb{C}^{n_y\times n_w}$, and $\mathbf{G}_{22} \in \mathbb{C}^{n_y\times n_u}$.

Then a lower LFT with respect to matrix $\mathbf{K} \in \mathbb{C}^{n_u\times n_y}$ can be defined as [34]:

$$\mathcal{F}_l(\mathbf{G}, \mathbf{K}) = \mathbf{G}_{11} + \mathbf{G}_{12}\mathbf{K}(\mathbf{I}_{n_y} - \mathbf{G}_{22}\mathbf{K})^{-1}\mathbf{G}_{21} \tag{3.38}$$

provided that matrix $\mathbf{I}_{n_y} - \mathbf{G}_{22}\mathbf{K}$ is nonsingular. The motivation and derivation of the lower LFT can be obtained starting from the block diagram shown in Figure 3.3, where $\mathbf{G}$ represents the linear dynamical system and $\mathbf{K}$ represents the feedback control to be designed.

The LFT mapping encompasses the two systems in a single one denoted as $\mathbf{M}$ in Figure 3.4, that is:

$$\mathbf{M} = \mathcal{F}_l(\mathbf{G}, \mathbf{K}) \tag{3.39}$$

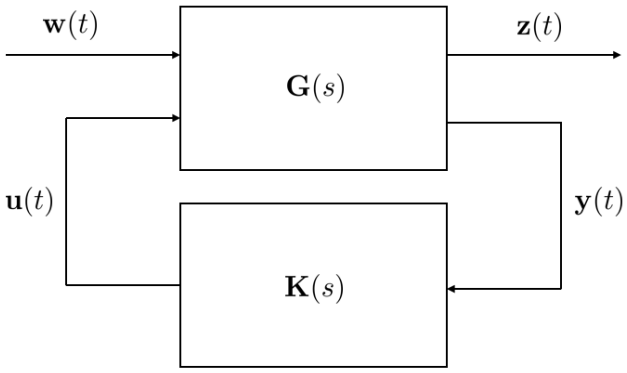

Figure 3.3: Lower LFT block diagram

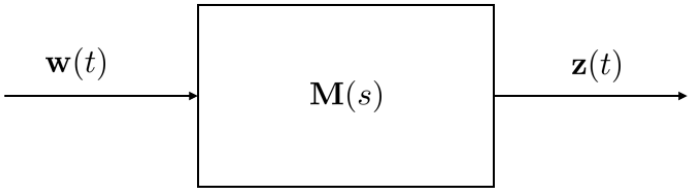

Figure 3.4: Lower LFT closed-loop block diagram

with exogenous variable acting on the system as the only inputs and the performance parameters as the output.

Starting from the block diagram depicted in Figure 3.3 the following relations can be inferred:

$$\begin{Bmatrix} \mathbf{z} \\ \mathbf{y} \end{Bmatrix} = \mathbf{G} \begin{Bmatrix} \mathbf{w} \\ \mathbf{u} \end{Bmatrix} = \begin{bmatrix} \mathbf{G}_{11} & \mathbf{G}_{12} \\ \mathbf{G}_{21} & \mathbf{G}_{22} \end{bmatrix} \begin{Bmatrix} \mathbf{w} \\ \mathbf{u} \end{Bmatrix} \tag{3.40}$$

$$\mathbf{u} = \mathbf{K}\mathbf{y} \tag{3.41}$$

that can also be written as:

$$\mathbf{z} = \mathbf{G}_{11}\mathbf{w} + \mathbf{G}_{12}\mathbf{u} \tag{3.42}$$

$$\mathbf{y} = \mathbf{G}_{21}\mathbf{w} + \mathbf{G}_{22}\mathbf{u} \tag{3.43}$$

$$\mathbf{u} = \mathbf{K}\mathbf{y} \tag{3.44}$$

By substituting the third relation into the first two equations and solving for $\mathbf{y}$ in the second equation:

$$\mathbf{z} = \mathbf{G}_{11}\mathbf{w} + \mathbf{G}_{12}\mathbf{K}\mathbf{y} \tag{3.45}$$

$$\mathbf{y} = (\mathbf{I}_{n_y} - \mathbf{G}_{22}\mathbf{K})^{-1}\mathbf{G}_{21}\mathbf{w} \tag{3.46}$$

The expression for the lower LFT is then derived by writing $\mathbf{y}$ of the second expression into the first equation as the closed-loop transfer function between the input $\mathbf{w}$ and the output $\mathbf{z}$:

$$\mathbf{z} = [\mathbf{G}_{11} + \mathbf{G}_{12}\mathbf{K}(\mathbf{I}_{n_y} - \mathbf{G}_{22}\mathbf{K})^{-1}\mathbf{G}_{21}]\mathbf{w} \tag{3.47}$$
$$= \mathcal{F}_l(\mathbf{G}, \mathbf{K})\mathbf{w} = \mathbf{M}\mathbf{w} \tag{3.48}$$

An analogous reasoning can be implemented to derive the upper LFT with respect to matrix $\Delta \in \mathbb{R}^{n_u \times n_y}$, starting from the block diagram shown in Figure 3.5.

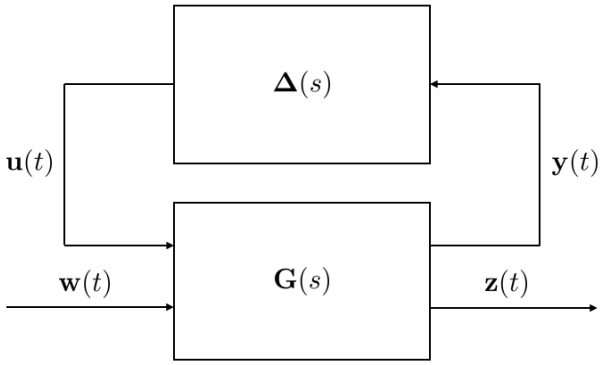

Figure 3.5: Upper LFT block diagram

Matrix $\mathbf{G}$ is partitioned differently, with $\mathbf{G}_{11} \in \mathbb{C}^{n_y \times n_u}$, $\mathbf{G}_{12} \in \mathbb{C}^{n_y \times n_w}$, $\mathbf{G}_{21} \in \mathbb{C}^{n_z \times n_u}$, and $\mathbf{G}_{22} \in \mathbb{C}^{n_z \times n_w}$.

The following expressions are derived:

$$\begin{Bmatrix} \mathbf{y} \\ \mathbf{z} \end{Bmatrix} = \begin{bmatrix} \mathbf{G}_{11} & \mathbf{G}_{12} \\ \mathbf{G}_{21} & \mathbf{G}_{22} \end{bmatrix} \begin{Bmatrix} \mathbf{u} \\ \mathbf{w} \end{Bmatrix} \tag{3.49}$$
$$\mathbf{u} = \boldsymbol{\Delta}\mathbf{y} \tag{3.50}$$

By carrying out a similar procedure, the expression for the upper LFT is derived and represents the closed-loop transfer function between the input $\mathbf{w}$ and the output $\mathbf{z}$ encompassing the dynamic systems $\mathbf{G}$ and $\boldsymbol{\Delta}$ as:

$$\mathbf{z} = [\mathbf{G}_{21} + \boldsymbol{\Delta}(\mathbf{I}_{n_y} - \mathbf{G}_{11}\boldsymbol{\Delta})^{-1}\mathbf{G}_{12} + \mathbf{G}_{22}]\mathbf{w} \tag{3.51}$$
$$= \mathcal{F}_u(\mathbf{G}, \boldsymbol{\Delta})\mathbf{w} = \mathbf{M}\mathbf{w} \tag{3.52}$$

The LFT is particularly useful in control theory for both controller analysis and synthesis. It can be demonstrated that any dynamical system can be put in the general LFT form as shown in Figure 3.6, where $\mathbf{G}$ is the block including the dynamics of the nominal plant, $\mathbf{K}$ is the feedback controller, and $\boldsymbol{\Delta}$ represents the uncertainties related to the system model [34]. The input, output and intermediate variables can be rearranged into vector $\mathbf{w}$, which includes external disturbances, noise, and reference signals, vector $\mathbf{z}$ encompassing all controlled signals and tracking errors, vectors $\mathbf{y}$ and $\mathbf{u}$ that denote

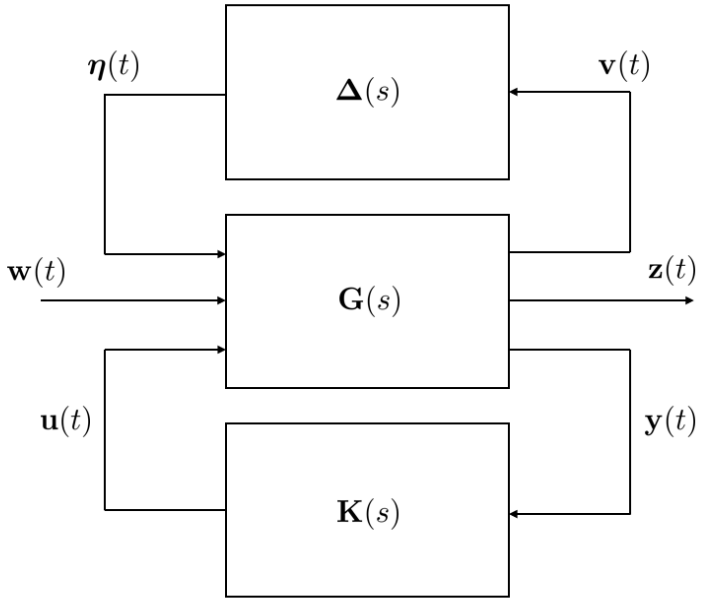

Figure 3.6: General LFT block diagram

the sensor outputs and the input control signal, and vectors $\mathbf{v}$ and $\boldsymbol{\eta}$ which represent the input and output signals of the uncertainty block $\boldsymbol{\Delta}$.

Once the system is put into the general LFT block form, the upper and lower LFTs can be employed to obtain the closed-loop transfer function. To show the procedure that permits to achieve such result, the generic nominal block system diagram without uncertainties is considered in Figure 3.7, and will be transformed into the LFT standard form. $\mathbf{P}$ is the nominal plant, $\mathbf{d}$ the external uncontrollable disturbance, $\mathbf{n}$ the measurement noise, while $\mathbf{W}_1$, $\mathbf{W}_2$, $\mathbf{W}_d$, and $\mathbf{W}_n$ represent selected weighting functions that can be tuned both in frequency and amplitude according to the knowledge about the input (in the $\mathbf{W}_d$ and $\mathbf{W}_n$ case) or the relative importance that it wants to be given to each output variable (in the case of $\mathbf{u}_f$ and $\mathbf{v}$).

To obtain the LFT standard form, the output variables are written as functions of the input parameters as:

$$\mathbf{v} = \mathbf{W}_2\mathbf{P}\mathbf{W}_d\mathbf{d} + \mathbf{W}_2\mathbf{P}\mathbf{u} \tag{3.53}$$

$$\mathbf{u}_f = \mathbf{W}_1\mathbf{u} \tag{3.54}$$

$$\mathbf{y} = \mathbf{W}_n\mathbf{n} + \mathbf{P}\mathbf{W}_d\mathbf{d} + \mathbf{P}\mathbf{u} \tag{3.55}$$

The exogenous variables and the performance parameters of the dynamical system are gathered into vector $\mathbf{w}$ and $\mathbf{z}$ respectively:

$$\mathbf{w} = \begin{Bmatrix} \mathbf{d} \\ \mathbf{n} \end{Bmatrix} \quad \mathbf{z} = \begin{Bmatrix} \mathbf{v} \\ \mathbf{u}_f \end{Bmatrix} \tag{3.56}$$

The LFT form in equation 3.40 is recovered as:

$$\begin{Bmatrix} \mathbf{z} \\ \mathbf{y} \end{Bmatrix} = \begin{bmatrix} \mathbf{G}_{11} & \mathbf{G}_{12} \\ \mathbf{G}_{21} & \mathbf{G}_{22} \end{bmatrix} \begin{Bmatrix} \mathbf{w} \\ \mathbf{u} \end{Bmatrix} \rightarrow \begin{Bmatrix} \mathbf{v} \\ \mathbf{u}_f \\ \mathbf{y} \end{Bmatrix} = \left[\begin{array}{cc:c} \mathbf{W}_2\mathbf{P}\mathbf{W}_d & \mathbf{0} & \mathbf{W}_2\mathbf{P} \\ \mathbf{0} & \mathbf{0} & \mathbf{W}_1 \\ \hdashline \mathbf{P}\mathbf{W}_d & \mathbf{W}_n & \mathbf{P} \end{array}\right] \begin{Bmatrix} \mathbf{d} \\ \mathbf{n} \\ \mathbf{u} \end{Bmatrix} \tag{3.57}$$

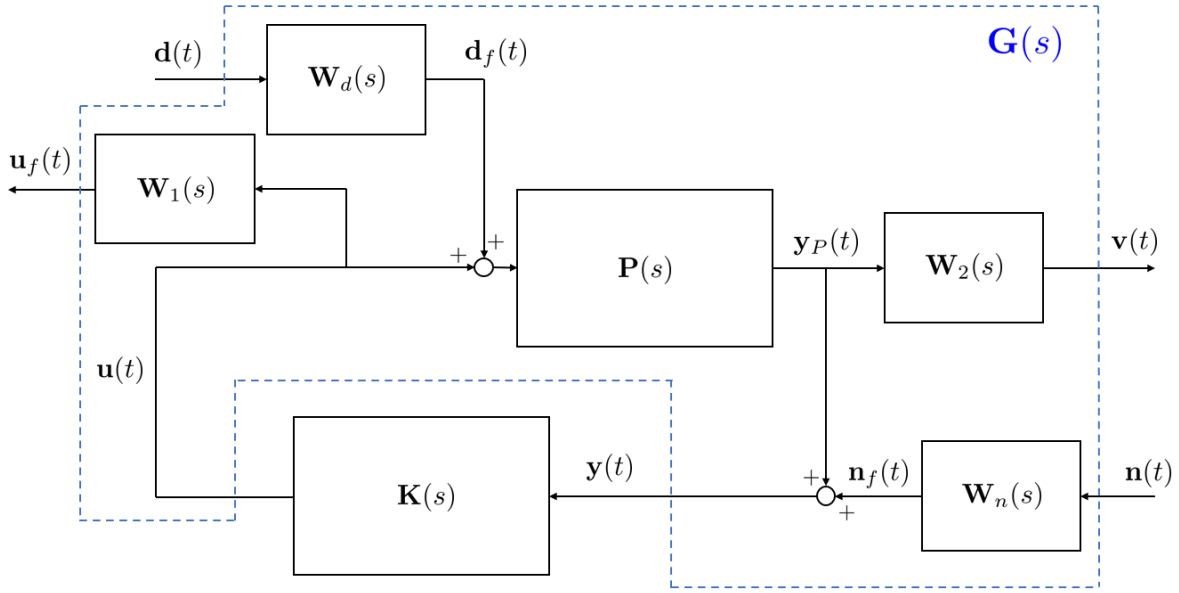

Figure 3.7: Block diagram representation of a generic system

A state-space realisation for the generalised dynamic system $\mathbf{G}$ from the generic block diagram in Figure 3.7 can be obtained by directly realising the transfer matrix $\mathbf{G}$ using multivariable realisation techniques. However, the direct realisation approach is usually complicated. Another way to obtain the state-space realisation of $\mathbf{G}$ can be achieved by means of known realisation of each component of the overall system, that can be written as:

$$\mathbf{P}(s) = \left[\begin{array}{c|c} \mathbf{A}_P & \mathbf{B}_P \\ \hline \mathbf{C}_P & \mathbf{D}_P \end{array}\right] \quad \mathbf{W}_1(s) = \left[\begin{array}{c|c} \mathbf{A}_u & \mathbf{B}_u \\ \hline \mathbf{C}_u & \mathbf{D}_u \end{array}\right] \quad \mathbf{W}_2(s) = \left[\begin{array}{c|c} \mathbf{A}_v & \mathbf{B}_v \\ \hline \mathbf{C}_v & \mathbf{D}_v \end{array}\right] \tag{3.58}$$

$$\mathbf{W}_d(s) = \left[\begin{array}{c|c} \mathbf{A}_d & \mathbf{B}_d \\ \hline \mathbf{C}_d & \mathbf{D}_d \end{array}\right] \quad \mathbf{W}_n(s) = \left[\begin{array}{c|c} \mathbf{A}_n & \mathbf{B}_n \\ \hline \mathbf{C}_n & \mathbf{D}_n \end{array}\right]$$

That is:

$$\dot{\mathbf{x}}_P = \mathbf{A}_P\mathbf{x}_P + \mathbf{B}_P(\mathbf{d}_f + \mathbf{u}); \quad \mathbf{y}_P = \mathbf{C}_P\mathbf{x}_P + \mathbf{D}_P(\mathbf{d}_f + \mathbf{u}) \tag{3.59}$$

$$\dot{\mathbf{x}}_u = \mathbf{A}_u\mathbf{x}_u + \mathbf{B}_u\mathbf{u}; \quad \mathbf{u}_f = \mathbf{C}_u\mathbf{x}_u + \mathbf{D}_u\mathbf{u} \tag{3.60}$$

$$\dot{\mathbf{x}}_v = \mathbf{A}_v\mathbf{x}_v + \mathbf{B}_v\mathbf{y}_P; \quad \mathbf{v} = \mathbf{C}_v\mathbf{x}_v + \mathbf{D}_v\mathbf{y}_P \tag{3.61}$$

$$\dot{\mathbf{x}}_d = \mathbf{A}_d\mathbf{x}_d + \mathbf{B}_d\mathbf{d}; \quad \mathbf{d}_f = \mathbf{C}_d\mathbf{x}_d + \mathbf{D}_d\mathbf{d} \tag{3.62}$$

$$\dot{\mathbf{x}}_n = \mathbf{A}_n\mathbf{x}_n + \mathbf{B}_n\mathbf{n}; \quad \mathbf{n}_f = \mathbf{C}_n\mathbf{x}_n + \mathbf{D}_n\mathbf{n} \tag{3.63}$$

An augmented state vector is then defined:

$$\mathbf{x}(t) = \left\{\begin{array}{c} \mathbf{x}_P(t) \\ \mathbf{x}_u(t) \\ \mathbf{x}_v(t) \\ \mathbf{x}_d(t) \\ \mathbf{x}_n(t) \end{array}\right\} \tag{3.64}$$

The intermediate variables are expressed as functions of the inputs and of the system states as:

$$\mathbf{d}_f = \mathbf{C}_d\mathbf{x}_d + \mathbf{D}_d\mathbf{d} \tag{3.65}$$
$$\mathbf{y}_P = \mathbf{C}_P\mathbf{x}_P + \mathbf{D}_P(\mathbf{d}_f + \mathbf{u}) = \mathbf{C}_P\mathbf{x}_P + \mathbf{D}_P\mathbf{u} + \mathbf{D}_P\mathbf{C}_d\mathbf{x}_d + \mathbf{D}_P\mathbf{D}_d\mathbf{d} \tag{3.66}$$
$$\mathbf{n}_f = \mathbf{C}_n\mathbf{x}_n + \mathbf{D}_n\mathbf{n} \tag{3.67}$$

The dynamics of the augmented state components can be written as:

$$\dot{\mathbf{x}}_P = \mathbf{A}_P\mathbf{x}_P + \mathbf{B}_P\mathbf{u} + \mathbf{B}_P\mathbf{C}_d\mathbf{x}_d + \mathbf{B}_P\mathbf{D}_d\mathbf{d} \tag{3.68}$$
$$\dot{\mathbf{x}}_u = \mathbf{A}_u\mathbf{x}_u + \mathbf{B}_u\mathbf{u} \tag{3.69}$$
$$\dot{\mathbf{x}}_v = \mathbf{A}_v\mathbf{x}_v + \mathbf{B}_v\mathbf{C}_P\mathbf{x}_P + \mathbf{B}_v\mathbf{D}_P\mathbf{u} + \mathbf{B}_v\mathbf{D}_P\mathbf{C}_d\mathbf{x}_d + \mathbf{B}_v\mathbf{D}_P\mathbf{D}_d\mathbf{d} \tag{3.70}$$
$$\dot{\mathbf{x}}_d = \mathbf{A}_d\mathbf{x}_d + \mathbf{B}_d\mathbf{d} \tag{3.71}$$
$$\dot{\mathbf{x}}_n = \mathbf{A}_n\mathbf{x}_n + \mathbf{B}_n\mathbf{n} \tag{3.72}$$

with performance and output equations:

$$\mathbf{z} = \begin{Bmatrix} \mathbf{v} \\ \mathbf{u}_f \end{Bmatrix} = \begin{Bmatrix} \mathbf{C}_v\mathbf{x}_v + \mathbf{D}_v\mathbf{C}_P\mathbf{x}_P + \mathbf{D}_v\mathbf{D}_P\mathbf{u} + \mathbf{D}_v\mathbf{D}_P\mathbf{C}_d\mathbf{x}_d + \mathbf{D}_v\mathbf{D}_P\mathbf{D}_d\mathbf{d} \\ \mathbf{C}_u\mathbf{x}_u + \mathbf{D}_u\mathbf{u} \end{Bmatrix} \tag{3.73}$$
$$\mathbf{y} = \mathbf{C}_P\mathbf{x}_P + \mathbf{D}_P\mathbf{u} + \mathbf{D}_P\mathbf{C}_d\mathbf{x}_d + \mathbf{D}_P\mathbf{D}_d\mathbf{d} + \mathbf{C}_n\mathbf{x}_n + \mathbf{D}_n\mathbf{n} \tag{3.74}$$

The state-space realisation of $\mathbf{G}$ is then:

$$\dot{\mathbf{x}}(t) = \mathbf{A}\mathbf{x}(t) + \mathbf{B}_w\mathbf{w}(t) + \mathbf{B}_u\mathbf{u}(t) \tag{3.75}$$
$$\mathbf{z}(t) = \mathbf{C}_z\mathbf{x}(t) + \mathbf{D}_{zw}\mathbf{w}(t) + \mathbf{D}_{zu}\mathbf{u}(t) \tag{3.76}$$
$$\mathbf{y}(t) = \mathbf{C}_y\mathbf{x}(t) + \mathbf{D}_{yw}\mathbf{w}(t) + \mathbf{D}_{yu}\mathbf{u}(t) \tag{3.77}$$

or, alternatively:

$$\begin{aligned} \mathbf{G}(s) &= \left[\begin{array}{c|cc} \mathbf{A} & \mathbf{B}_w & \mathbf{B}_u \\ \hline \mathbf{C}_z & \mathbf{D}_{zw} & \mathbf{D}_{zu} \\ \mathbf{C}_y & \mathbf{D}_{yw} & \mathbf{D}_{yu} \end{array}\right] = \begin{bmatrix} \mathbf{C}_z \\ \mathbf{C}_y \end{bmatrix} (s\mathbf{I}_n - \mathbf{A})^{-1} \begin{bmatrix} \mathbf{B}_w & \mathbf{B}_u \end{bmatrix} + \begin{bmatrix} \mathbf{D}_{zw} & \mathbf{D}_{zu} \\ \mathbf{D}_{yw} & \mathbf{D}_{yu} \end{bmatrix} \\ &= \left[\begin{array}{cc:c} \mathbf{W}_2\mathbf{P}\mathbf{W}_d & \mathbf{0} & \mathbf{W}_2\mathbf{P} \\ \mathbf{0} & \mathbf{0} & \mathbf{W}_1 \\ \hdashline \mathbf{P}\mathbf{W}_d & \mathbf{W}_n & \mathbf{P} \end{array}\right] = \begin{bmatrix} \mathbf{G}_{11} & \mathbf{G}_{12} \\ \mathbf{G}_{21} & \mathbf{G}_{22} \end{bmatrix} \end{aligned} \tag{3.78}$$

with:

$$\mathbf{A} = \begin{bmatrix} \mathbf{A}_P & \mathbf{0} & \mathbf{0} & \mathbf{B}_P\mathbf{C}_d & \mathbf{0} \\ \mathbf{0} & \mathbf{A}_u & \mathbf{0} & \mathbf{0} & \mathbf{0} \\ \mathbf{B}_v\mathbf{C}_P & \mathbf{0} & \mathbf{A}_v & \mathbf{B}_v\mathbf{D}_P\mathbf{C}_d & \mathbf{0} \\ \mathbf{0} & \mathbf{0} & \mathbf{0} & \mathbf{A}_d & \mathbf{0} \\ \mathbf{0} & \mathbf{0} & \mathbf{0} & \mathbf{0} & \mathbf{A}_n \end{bmatrix} \tag{3.79}$$

$$\mathbf{B}_u = \begin{bmatrix} \mathbf{B}_P\mathbf{D}_d & \mathbf{0} \\ \mathbf{0} & \mathbf{0} \\ \mathbf{B}_v\mathbf{D}_P\mathbf{D}_d & \mathbf{0} \\ \mathbf{B}_d & \mathbf{0} \\ \mathbf{0} & \mathbf{B}_w \end{bmatrix} \quad \mathbf{B}_u = \begin{bmatrix} \mathbf{B}_P \\ \mathbf{B}_u \\ \mathbf{B}_v\mathbf{D}_P \\ \mathbf{0} \\ \mathbf{0} \end{bmatrix} \tag{3.80}$$

$$\mathbf{C}_z = \begin{bmatrix} \mathbf{C}_P & \mathbf{0} & \mathbf{C}_v & \mathbf{D}_v\mathbf{D}_P\mathbf{C}_d & \mathbf{0} \\ \mathbf{0} & \mathbf{C}_u & \mathbf{0} & \mathbf{0} & \mathbf{0} \end{bmatrix} \quad \mathbf{C}_y = \begin{bmatrix} \mathbf{C}_P & \mathbf{0} & \mathbf{0} & \mathbf{D}_P\mathbf{C}_d & \mathbf{0} \end{bmatrix} \tag{3.81}$$

$$\mathbf{D}_{zw} = \begin{bmatrix} \mathbf{D}_v\mathbf{D}_P\mathbf{D}_d & \mathbf{0} \\ \mathbf{0} & \mathbf{0} \end{bmatrix} \quad \mathbf{D}_{zu} = \begin{bmatrix} \mathbf{D}_v\mathbf{D}_P \\ \mathbf{D}_u \end{bmatrix} \quad \mathbf{D}_{yw} = \begin{bmatrix} \mathbf{D}_P\mathbf{D}_d & \mathbf{D}_n \end{bmatrix} \quad \mathbf{D}_{yu} = \mathbf{D}_P \tag{3.82}$$

3.5 $\mathcal{H}_\infty$ controller

The $\mathcal{H}_\infty$ control theory is generally formulated by considering the dynamical system represented in the LFT framework as shown in Figure 3.3, where the plant $\mathbf{G}$ and the controller $\mathbf{K}$ are assumed to be real, rational, and proper. Furthermore, it is assumed that the state-space model of $\mathbf{G}$ is available and its realisation is stabilisable and detectable.

The $\mathcal{H}_\infty$ control synthesis is an optimisation process, that implements a set of controllers that minimise the closed-loop gain between the uncontrolled exogenous inputs $\mathbf{w}$ and the performance parameters $\mathbf{z}$ in the $\mathcal{H}_\infty$ norm sense. In other words, a dynamic system $\mathbf{K}(s)$ is sought such that it stabilises the plant and robustly controls it, by minimising the value [34]:

$$||\mathbf{M}||_\infty = ||\mathcal{F}_l(\mathbf{G}, \mathbf{K})||_\infty = \sup_\omega \overline{\sigma}(\mathcal{F}_l(\mathbf{G}, \mathbf{K})(j\omega)) \tag{3.83}$$

A controller that satisfies such requirements is said to be an optimal $\mathcal{H}_\infty$ control. In general, optimal $\mathcal{H}_\infty$ controllers are not unique for multiple-input and multiple-output systems. In addition, finding an optimal $\mathcal{H}_\infty$ controller is generally both numerically and theoretically complicated. In practice, it is often not necessary to design an optimal controller and it is much cheaper to obtain controllers that are very close in the norm sense to the optimal ones, which are called suboptimal controllers. Suboptimal controllers might also have additional desirable properties over optimal ones, such as lower bandwidth.

Given a real number $\gamma > 0$, a suboptimal controller $\mathbf{K}(s)$ is then defined as a dynamical system that stabilises the nominal plant $\mathbf{G}(s)$ and such that [34]:

$$||\mathbf{M}||_\infty = ||\mathcal{F}_l(\mathbf{G}, \mathbf{K})||_\infty < \gamma \tag{3.84}$$

The general suboptimal $\mathcal{H}_\infty$ solution is obtained by considering the generic form of the plant $\mathbf{G}$ and its state-space realisation of the form:

$$\mathbf{G}(s) = \left[\begin{array}{c|cc} \mathbf{A} & \mathbf{B}_1 & \mathbf{B}_2 \\ \hline \mathbf{C}_1 & \mathbf{D}_{11} & \mathbf{D}_{12} \\ \mathbf{C}_2 & \mathbf{D}_{21} & \mathbf{D}_{22} \end{array}\right] = \left[\begin{array}{c|c} \mathbf{A} & \mathbf{B} \\ \hline \mathbf{C} & \mathbf{D} \end{array}\right] \tag{3.85}$$

which is compatible with the dimensions of $\mathbf{x}(t) \in \mathbb{R}^n$, $\mathbf{z}(t) \in \mathbb{R}^{n_z}$, $\mathbf{y}(t) \in \mathbb{R}^{n_y}$, $\mathbf{w}(t) \in \mathbb{R}^{n_w}$, and $\mathbf{u}(t) \in \mathbb{R}^{n_u}$.

Moreover, the performance vector $\mathbf{z}(t)$ can be partitioned into a vector $\mathbf{u}_f(t) \in \mathbb{R}^{n_u}$, which includes performances connected to the control variable $\mathbf{u}(t)$ via some weighting functions and with the same number of entries, along with a second vector $\mathbf{v}(t) \in \mathbb{R}^{n_v}$ that considers other relevant performance parameters. Similarly, vector $\mathbf{w}(t)$ can be divided into a part linked to external disturbances $\mathbf{d}(t) \in \mathbb{R}^{n_d}$ and a vector $\mathbf{n}(t) \in \mathbb{R}^{n_y}$ encompassing measurement noises of the same dimension of the output vector $\mathbf{y}(t)$.

For the purpose of this study the case $\mathbf{D}_{12} = \mathbf{I}$ and $\mathbf{D}_{22} = \mathbf{0}$ is considered to simplify the solution procedure.

In addition, the following assumptions are made [34]:

(1) The pair $(\mathbf{A}, \mathbf{B}_2)$ is stabilisable and the pair $(\mathbf{C}_2, \mathbf{A})$ is detectable;

(2) $\mathbf{D}_{21} = \begin{bmatrix}\mathbf{0}_{n_y \times n_d} & \mathbf{I}_{n_y}\end{bmatrix}$, in case this assumption is not satisfied and $\mathbf{D}_{21}$ has full row rank a normalisation procedure can be implemented to obtain an equivalent system satisfying the assumption;

(3) $\begin{bmatrix}\mathbf{A} - j\omega\mathbf{I}_n & \mathbf{B}_2 \\ \mathbf{C}_1 & \mathbf{D}_{12}\end{bmatrix}$ has full column rank for all ω;

(4) $\begin{bmatrix}\mathbf{A} - j\omega\mathbf{I}_n & \mathbf{B}_1 \\ \mathbf{C}_2 & \mathbf{D}_{21}\end{bmatrix}$ has full column rank for all ω.

The first assumption guarantees the existence of a stabilising controller. The second assumption means that the exogenous signal $\mathbf{w}(t)$ includes both plant disturbance and sensor noise, and that the sensor noise weighting function is normalised and nonsingular. The last two assumptions are necessary so that $\mathbf{G}(s)$ has no eigenvalues on the imaginary axis.

Due to the simplifications mentioned above, the state-space representation of the open-loop plant $\mathbf{G}$ can be written as:

$$\mathbf{G}(s) = \left[\begin{array}{c|cc} \mathbf{A} & \mathbf{B}_1 & \mathbf{B}_2 \\ \hline \mathbf{C}_1 & \mathbf{D}_{11} & \mathbf{I} \\ \mathbf{C}_2 & \mathbf{D}_{21} & \mathbf{0} \end{array}\right] \tag{3.86}$$

To obtain the solution for the suboptimal $\mathcal{H}_\infty$ controller,the real parameter γ shall be selected. Furthermore, several matrices need to be introduced [34]:

$$\mathbf{D}_{10} = \begin{bmatrix}\mathbf{D}_{11} & \mathbf{D}_{12}\end{bmatrix} \in \mathbb{R}^{n_z \times (n_w + n_u)} \tag{3.87}$$

$$\mathbf{D}_{01} = \begin{bmatrix}\mathbf{D}_{12} \\ \mathbf{D}_{22}\end{bmatrix} \in \mathbb{R}^{(n_z + n_y) \times n_w} \tag{3.88}$$

$$\mathbf{R} = \mathbf{D}_{10}^T \mathbf{D}_{10} - \begin{bmatrix}\gamma^2 \mathbf{I}_{n_w} & \mathbf{0}_{n_u} \\ \mathbf{0}_{n_u} & \mathbf{0}_{n_w}\end{bmatrix} \in \mathbb{R}^{(n_w + n_u) \times (n_w + n_u)} \tag{3.89}$$

$$\widetilde{\mathbf{R}} = \mathbf{D}_{01} \mathbf{D}_{01}^T - \begin{bmatrix}\gamma^2 \mathbf{I}_{n_z} & \mathbf{0}_{n_y} \\ \mathbf{0}_{n_y} & \mathbf{0}_{n_z}\end{bmatrix} \in \mathbb{R}^{(n_z + n_y) \times (n_z + n_y)} \tag{3.90}$$

$$\mathbf{H}_\infty = \begin{bmatrix}\mathbf{A} & \mathbf{0}_n \\ -\mathbf{C}_1^T \mathbf{C}_1 & -\mathbf{A}^T\end{bmatrix} - \begin{bmatrix}\mathbf{B} \\ -\mathbf{C}_1^T \mathbf{D}_{10}\end{bmatrix} \mathbf{R}^{-1} \begin{bmatrix}\mathbf{D}_{10}^T \mathbf{C}_1 & \mathbf{B}^T\end{bmatrix} \in \mathbb{R}^{2n \times 2n} \tag{3.91}$$

$$\mathbf{X}_\infty = \text{Ric}(\mathbf{H}_\infty) \in \mathbb{R}^{n\times n} \tag{3.92}$$

$$\mathbf{J}_\infty = \begin{bmatrix} \mathbf{A}^T & \mathbf{0}_n \\ -\mathbf{B}_1\mathbf{B}_1^T & -\mathbf{A} \end{bmatrix} - \begin{bmatrix} \mathbf{C}^T \\ -\mathbf{B}_1\mathbf{D}_{01}^T \end{bmatrix} \widetilde{\mathbf{R}}^{-1} \begin{bmatrix} \mathbf{D}_{01}\mathbf{B}_1^T & \mathbf{C} \end{bmatrix} \in \mathbb{R}^{2n\times 2n} \tag{3.93}$$

$$\mathbf{Y}_\infty = \text{Ric}(\mathbf{J}_\infty) \in \mathbb{R}^{n\times n} \tag{3.94}$$

$$\mathbf{F} = \begin{bmatrix} \mathbf{F}_{1\infty} \\ \mathbf{F}_{2\infty} \end{bmatrix} = -\mathbf{R}^{-1}(\mathbf{D}_{10}^T\mathbf{C}_1 + \mathbf{B}^T\mathbf{X}_\infty) \in \mathbb{R}^{(n_w+n_u)\times n} \tag{3.95}$$

$$\mathbf{L} = \begin{bmatrix} \mathbf{L}_{1\infty} & \mathbf{L}_{2\infty} \end{bmatrix} = -(\mathbf{B}_1\mathbf{D}_{01}^T + \mathbf{Y}_\infty\mathbf{C}^T)\widetilde{\mathbf{R}}^{-1} \in \mathbb{R}^{n\times(n_z+n_y)} \tag{3.96}$$

In particular $\mathbf{X}_\infty$ has been defined as the stabilising solution of the following algebraic Riccati equation associated to the Hamiltonian matrix $\mathbf{H}_\infty$:

$$\begin{aligned}(\mathbf{A}^T - \mathbf{C}_1^T\mathbf{D}_{10}\mathbf{R}^{-1}\mathbf{B}^T)\mathbf{X}_\infty + \mathbf{X}_\infty(\mathbf{A} - \mathbf{B}\mathbf{R}^{-1}\mathbf{D}_{10}^T\mathbf{C}_1) - \mathbf{X}_\infty\mathbf{B}\mathbf{R}^{-1}\mathbf{B}^T\mathbf{X}_\infty + \\ + \mathbf{C}_1^T\mathbf{C}_1 - \mathbf{C}_1^T\mathbf{D}_{10}\mathbf{R}^{-1}\mathbf{D}_{10}^T\mathbf{C}_1 = \mathbf{0}_n\end{aligned} \tag{3.97}$$

Likewise, $\mathbf{Y}_\infty$ is the stabilising solution of the following ARE associated to the Hamiltonian matrix $\mathbf{J}_\infty$:

$$\begin{aligned}(\mathbf{A} - \mathbf{B}_1\mathbf{D}_{01}^T\widetilde{\mathbf{R}}^{-1}\mathbf{C})\mathbf{Y}_\infty + \mathbf{Y}_\infty(\mathbf{A}^T - \mathbf{C}^T\widetilde{\mathbf{R}}^{-1}\mathbf{D}_{01}\mathbf{B}_1^T) - \mathbf{Y}_\infty\mathbf{C}^T\widetilde{\mathbf{R}}^{-1}\mathbf{C}\mathbf{Y}_\infty + \\ + \mathbf{B}_1\mathbf{B}_1^T - \mathbf{B}_1\mathbf{D}_{01}^T\widetilde{\mathbf{R}}^{-1}\mathbf{D}_{01}\mathbf{B}_1^T = \mathbf{0}_n\end{aligned} \tag{3.98}$$

Matrices $\mathbf{D} \in \mathbb{R}^{(n_z+n_y)\times(n_w+n_u)}$, $\mathbf{F}_{1\infty} \in \mathbb{R}^{n_w\times n}$, and $\mathbf{L}_{1\infty} \in \mathbb{R}^{n\times n_z}$ can be further partitioned as follows [34]:

$$\mathbf{D} = \begin{bmatrix} \mathbf{D}_{1111} & \mathbf{D}_{1112} & \mathbf{0}_{n_v\times n_u} \\ \mathbf{D}_{1121} & \mathbf{D}_{1122} & \mathbf{0}_{n_u} \\ \mathbf{0}_{n_y\times n_d} & \mathbf{I}_{n_y} & \mathbf{0}_{n_y\times n_u} \end{bmatrix} \tag{3.99}$$

$$\mathbf{F}_{1\infty}^T = \begin{bmatrix} \mathbf{F}_{11\infty}^T & \mathbf{F}_{12\infty}^T \end{bmatrix} \tag{3.100}$$

$$\mathbf{L}_{1\infty}^T = \begin{bmatrix} \mathbf{L}_{11\infty}^T \\ \mathbf{L}_{12\infty}^T \end{bmatrix} \tag{3.101}$$

where $\mathbf{D}_{1111} \in \mathbb{R}^{n_v\times n_d}$, $\mathbf{D}_{1112} \in \mathbb{R}^{n_v\times n_y}$, $\mathbf{D}_{1121} \in \mathbb{R}^{n_u\times n_d}$, $\mathbf{D}_{1122} \in \mathbb{R}^{n_u\times n_y}$, $\mathbf{F}_{11\infty}^T \in \mathbb{R}^{n\times n_d}$, $\mathbf{F}_{12\infty}^T \in \mathbb{R}^{n\times n_y}$, $\mathbf{L}_{11\infty}^T \in \mathbb{R}^{n_v\times n}$, and $\mathbf{L}_{12\infty}^T \in \mathbb{R}^{n_u\times n}$.

Once the above matrices are introduced, the suboptimal $\mathcal{H}_\infty$ control can be implemented by means of the following theorem:

Theorem for suboptimal $\mathcal{H}_\infty$ synthesis [15].
If $\mathbf{G}$ satisfies the assumptions (1) to (4), then:

(a) There exists a stabilising controller $\mathbf{K}(s)$ such that $||\mathcal{F}_l(\mathbf{G},\mathbf{K})||_\infty < \gamma$ if and only if:

- $\gamma > \overline{\sigma}(\mathbf{D}_{1121})$;

- $\mathbf{H}_\infty \in \text{dom(Ric)}$ with $\mathbf{X}_\infty = \text{Ric}(\mathbf{H}_\infty) \geq 0$;
- $\mathbf{J}_\infty \in \text{dom(Ric)}$ with $\mathbf{Y}_\infty = \text{Ric}(\mathbf{J}_\infty) \geq 0$;
- $\rho(\mathbf{X}_\infty \mathbf{Y}_\infty) < \gamma^2$.

(b) Given that the conditions of part (a) are satisfied, then all rational stabilising controllers $\mathbf{K}(s)$ satisfying $||\mathcal{F}_l(\mathbf{G}, \mathbf{K})||_\infty < \gamma$ are given by:

$$\mathbf{K} = \mathcal{F}_l(\mathbf{M}_\infty, \mathbf{Q}) \quad \text{for arbitrary } \mathbf{Q} \text{ such that } ||\mathbf{Q}||_\infty \tag{3.102}$$

where:

$$\mathbf{M}_\infty = \left[\begin{array}{c|cc} \hat{\mathbf{A}} & \hat{\mathbf{B}}_1 & \hat{\mathbf{B}}_2 \\ \hline \hat{\mathbf{C}}_1 & \hat{\mathbf{D}}_{11} & \hat{\mathbf{D}}_{12} \\ \hat{\mathbf{C}}_2 & \hat{\mathbf{D}}_{21} & \mathbf{0} \end{array}\right] \tag{3.103}$$

$$\hat{\mathbf{D}}_{11} = -\mathbf{D}_{1122} \tag{3.104}$$

$\hat{\mathbf{D}}_{12} \in \mathbb{R}^{n_u \times n_u}$ and $\hat{\mathbf{D}}_{21} \in \mathbb{R}^{n_y \times n_y}$ are any matrices (e.g. Cholesky factorisation) satisfying:

$$\hat{\mathbf{D}}_{12}\hat{\mathbf{D}}_{12}^T = \mathbf{I}_{n_u} - \frac{1}{\gamma^2}\mathbf{D}_{1121}\mathbf{D}_{1121}^T \tag{3.105}$$

$$\hat{\mathbf{D}}_{12}\hat{\mathbf{D}}_{12}^T = \mathbf{I}_{n_y} \tag{3.106}$$

and:

$$\hat{\mathbf{B}}_2 = \mathbf{Z}_\infty(\mathbf{B}_2 + \mathbf{L}_{12\infty})\hat{\mathbf{D}}_{12} \tag{3.107}$$

$$\hat{\mathbf{C}}_2 = -\hat{\mathbf{D}}_{21}(\mathbf{C}_2 + \mathbf{F}_{12\infty}) \tag{3.108}$$

$$\hat{\mathbf{B}}_1 = -\mathbf{Z}_\infty \mathbf{L}_{2\infty} + \hat{\mathbf{B}}_2 \hat{\mathbf{D}}_{12}^{-1}\hat{\mathbf{D}}_{11} \tag{3.109}$$

$$\hat{\mathbf{C}}_1 = \mathbf{F}_{2\infty} + \hat{\mathbf{D}}_{11}\hat{\mathbf{D}}_{21}^{-1}\hat{\mathbf{C}}_2 \tag{3.110}$$

$$\hat{\mathbf{A}} = \mathbf{A} + \mathbf{B}\mathbf{F} + \hat{\mathbf{B}}_1\hat{\mathbf{D}}_{21}^{-1}\hat{\mathbf{C}}_2 \tag{3.111}$$

where

$$\mathbf{Z}_\infty = \left(\mathbf{I}_n - \frac{1}{\gamma^2}\mathbf{Y}_\infty \mathbf{X}_\infty\right)^{-1} \tag{3.112}$$

3.6 $\mathcal{H}_\infty$ filtering

The filtering problem is a mathematical model which aims to find an estimate $\hat{\mathbf{z}}(t)$ of a specific quantity of interest $\mathbf{z}(t)$ related to the system, by means of the output measurement $\mathbf{y}(t)$ [34]. The filtering problem can be formulated and solved using the $\mathcal{H}_\infty$ theory, since it can be regarded as a particular case of the $\mathcal{H}_\infty$ control problem, in which there is no stability requirement, and the estimator $\mathbf{F}(s)$ does not generate any input $\mathbf{u}(t)$, in contrast with the $\mathcal{H}_\infty$ controller $\mathbf{K}(s)$. The block diagram of the generic filtering problem is depicted is Figure 3.9.

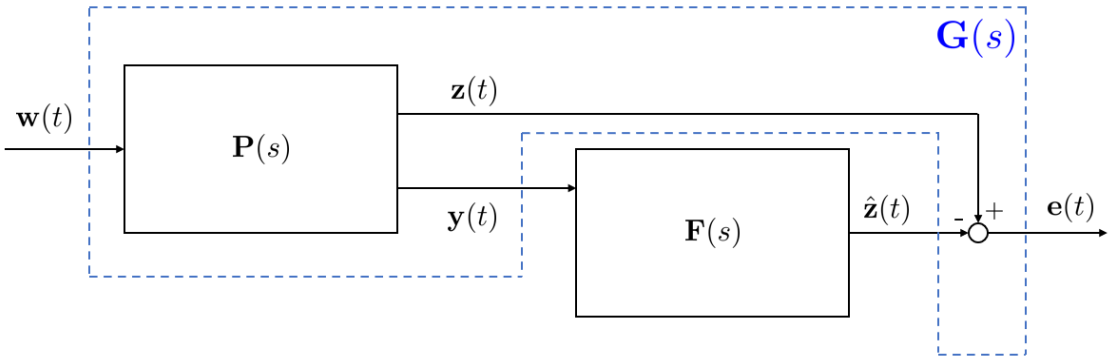

Figure 3.8: Block diagram representation of a generic system for filtering problems

A state-space representation of the dynamic system $\mathbf{P}(s)$ for which the estimate of the performance variable $\mathbf{z}(t)$ is sought can be written as:

$$\dot{\mathbf{x}}(t) = \mathbf{A}\mathbf{x}(t) + \mathbf{B}_w\mathbf{w}(t) \tag{3.113}$$
$$\mathbf{z}(t) = \mathbf{C}_z\mathbf{x}(t) + \mathbf{D}_{zw}\mathbf{w}(t) \tag{3.114}$$
$$\mathbf{y}(t) = \mathbf{C}_y\mathbf{x}(t) + \mathbf{D}_{yw}\mathbf{w}(t) \tag{3.115}$$

The quantity to be minimised is the estimation error, which is defined as:

$$\mathbf{e}(t) = \mathbf{z}(t) - \hat{\mathbf{z}}(t) = \mathbf{C}_z\mathbf{x}(t) + \mathbf{D}_{zw}\mathbf{w}(t) - \hat{\mathbf{z}}(t) \tag{3.116}$$

To obtain the solution of the $\mathcal{H}_\infty$ filtering problem, the system is rearranged so that it can be formulated in the LFT framework. The open-loop transfer function representing the system is then transformed into $\mathbf{G}(s)$ with exogenous input $\mathbf{w}(t)$, output measurement $\mathbf{y}(t)$, and performance vector to be minimised $\mathbf{e}(t)$. The input control variable is here replaced by the estimate $\hat{\mathbf{z}}(t)$, which is also the output of the $\mathcal{H}_\infty$ estimator $\mathbf{F}(s)$, as shown in Figure 3.9. Such variable does not influence the plant dynamics nor the output measured by the sensors. The only dependence of $\hat{\mathbf{z}}(t)$ can be seen in the definition of the performance variable $\mathbf{e}(t)$.

Using the above mentioned considerations, the block diagram in Figure 3.8 and the expression of $\mathbf{e}(t)$ in (3.116), the state-space formulation of the dynamics system $\mathbf{G}$ can be written as:

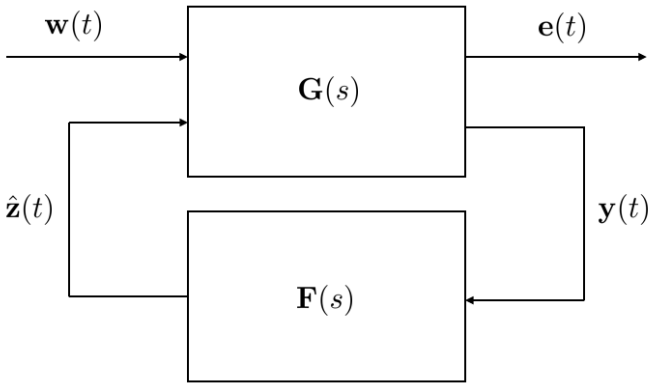

Figure 3.9: Lower LFT block diagram for estimation problems

$$\dot{\mathbf{x}}(t) = \mathbf{A}\mathbf{x}(t) + \mathbf{B}_w\mathbf{w}(t) \tag{3.117}$$
$$\mathbf{e}(t) = \mathbf{z}(t) - \hat{\mathbf{z}}(t) = \mathbf{C}_z\mathbf{x}(t) + \mathbf{D}_{zw}\mathbf{w}(t) + \mathbf{D}_{e\hat{z}}\hat{\mathbf{z}}(t) \tag{3.118}$$
$$\mathbf{y}(t) = \mathbf{C}_y\mathbf{x}(t) + \mathbf{D}_{yw}\mathbf{w}(t) \tag{3.119}$$

where $\mathbf{D}_{e\hat{z}} = -\mathbf{I}_{n_z}$ from the definition of the estimation error $\mathbf{e}(t)$.

Given a real number $\gamma > 0$, a suboptimal $\mathcal{H}_\infty$ estimator $\mathbf{F}(s)$ can then be defined as a dynamical system such that [34]:

$$||\mathbf{M}||_\infty = ||\mathcal{F}_l(\mathbf{G}, \mathbf{F})||_\infty < \gamma \tag{3.120}$$

where the gain of the closed-loop transfer function $\mathbf{M}$ from the exogenous variables $\mathbf{w}(t)$ to the estimation error vector $\mathbf{e}(t)$ is minimised in the $\mathcal{H}_\infty$ norm sense.

The general suboptimal $\mathcal{H}_\infty$ solution is obtained by considering the generic form of the plant $\mathbf{F}$ and its state-space realisation of the form:

$$\mathbf{F}(s) = \left[\begin{array}{c|cc} \mathbf{A} & \mathbf{B}_1 & \mathbf{0}_{n\times n_z} \\ \hline \mathbf{C}_1 & \mathbf{D}_{11} & -\mathbf{I}_{n_z} \\ \mathbf{C}_2 & \mathbf{D}_{21} & \mathbf{0}_{n_y\times n_z} \end{array}\right] = \left[\begin{array}{c|c} \mathbf{A} & \mathbf{B} \\ \hline \mathbf{C} & \mathbf{D} \end{array}\right] \tag{3.121}$$

which is compatible with the dimensions of $\mathbf{x}(t) \in \mathbb{R}^n$, $\mathbf{z}(t) \in \mathbb{R}^{n_z}$, $\mathbf{y}(t) \in \mathbb{R}^{n_y}$, $\mathbf{w}(t) \in \mathbb{R}^{n_w}$, and $\hat{\mathbf{z}}(t) \in \mathbb{R}^{n_z}$.

Thus the solution to the above filtering problem can be obtained from the $\mathcal{H}_\infty$ control solution setting $\mathbf{B}_2 = \mathbf{0}$, $\mathbf{D}_{12} = -\mathbf{I}$, and dropping the internal stability requirement.

The following theorem can be used in order to implement the suboptimal $\mathcal{H}_\infty$ estimator:

Theorem for suboptimal $\mathcal{H}_\infty$ estimator synthesis [34].

If the pair ($\mathbf{C}_2$, $\mathbf{A}$) is detectable and the matrix

$$\begin{bmatrix} \mathbf{A} - j\omega\mathbf{I}_n & \mathbf{B}_1 \\ \mathbf{C}_2 & \mathbf{D}_{21} \end{bmatrix} \tag{3.122}$$

has full row rank for all ω, $\mathbf{D}_{21}$ is normalised and $\mathbf{D}_{11}$ is partitioned conformably as:

$$\begin{bmatrix} \mathbf{D}_{11} \\ \mathbf{D}_{21} \end{bmatrix} = \begin{bmatrix} \mathbf{D}_{111} & \mathbf{D}_{112} \\ \mathbf{0}_{n_y\times n_d} & \mathbf{I}_{n_y} \end{bmatrix} \tag{3.123}$$

where $\mathbf{D}_{11} \in \mathbb{R}^{n_z \times n_w}$, $\mathbf{D}_{21} \in \mathbb{R}^{n_y \times n_w}$, $\mathbf{D}_{111} \in \mathbb{R}^{n_z \times n_d}$, and $\mathbf{D}_{112} \in \mathbb{R}^{n_z \times n_y}$, then there exists a real rational transfer function $\mathbf{F}(s)$ such that $||\mathcal{F}_l(\mathbf{G}, \mathbf{F})||_\infty < \gamma$ if and only if:

- $\overline{\sigma}(\mathbf{D}_{111}) < \gamma$;
- $\mathbf{J}_\infty \in \text{dom}(\text{Ric})$ with $\mathbf{Y}_\infty = \text{Ric}(\mathbf{J}_\infty) \geq 0$

where:

$$\widetilde{\mathbf{R}} = \begin{bmatrix} \mathbf{D}_{11} \\ \mathbf{D}_{21} \end{bmatrix} \begin{bmatrix} \mathbf{D}_{11} \\ \mathbf{D}_{21} \end{bmatrix}^T - \begin{bmatrix} \gamma^2 \mathbf{I}_{n_z} & \mathbf{0}_{n_z \times n_y} \\ \mathbf{0}_{n_y \times n_z} & \mathbf{0}_{n_y} \end{bmatrix} \tag{3.124}$$

$$\mathbf{J}_\infty = \begin{bmatrix} \mathbf{A}^T & \mathbf{0}_n \\ -\mathbf{B}_1\mathbf{B}_1^T & -\mathbf{A} \end{bmatrix} - \begin{bmatrix} \mathbf{C}_1^T & \mathbf{C}_2^T \\ -\mathbf{B}_1\mathbf{D}_{11}^T & -\mathbf{B}_1\mathbf{D}_{21}^T \end{bmatrix} \widetilde{\mathbf{R}}^{-1} \begin{bmatrix} \mathbf{D}_{11}\mathbf{B}_1^T & \mathbf{C}_1 \\ \mathbf{D}_{12}\mathbf{B}_1^T & \mathbf{C}_2 \end{bmatrix} \tag{3.125}$$

$$\mathbf{Y}_\infty = \text{Ric}(\mathbf{J}_\infty) \tag{3.126}$$

Moreover, if the above conditions are satisfied, than a rational filter $\mathbf{F}(s)$ satisfying $||\mathcal{F}_l(\mathbf{G}, \mathbf{F})||_\infty < \gamma$ is given by:

$$\hat{\mathbf{z}}(s) = \mathbf{F}(s)\mathbf{y}(s) = \left[\begin{array}{c|c} \mathbf{A} + \mathbf{L}_{2\infty}\mathbf{C}_2 + \mathbf{L}_{1\infty}\mathbf{D}_{112}\mathbf{C}_2 & -\mathbf{L}_{2\infty} + \mathbf{L}_{1\infty}\mathbf{D}_{112} \\ \hline \mathbf{C}_1 - \mathbf{D}_{112}\mathbf{C}_2 & \mathbf{D}_{112} \end{array}\right] \mathbf{y}(s) \tag{3.127}$$

where

$$\begin{bmatrix} \mathbf{L}_{1\infty} & \mathbf{L}_{2\infty} \end{bmatrix} = -\begin{bmatrix} \mathbf{B}_1\mathbf{D}_{11}^T + \mathbf{Y}_\infty\mathbf{C}_1^T & \mathbf{B}_1\mathbf{D}_{21}^T + \mathbf{Y}_\infty\mathbf{C}_2^T \end{bmatrix} \widetilde{\mathbf{R}}_1^{-1} \tag{3.128}$$

Chapter 4

Nonlinear estimation techniques

4.1 The extended Kalman filter

THE input disturbance to be evaluated can assume any shape and in the general case it is nonlinear. Therefore, a nonlinear estimation approach shall be considered in order to implement an estimator which is capable to provide evaluation of the quantities of interest in the general nonlinear case.

The Extended Kalman Filter (EKF) is the most common estimation technique for nonlinear systems [28]. It is the nonlinear version of the linear Kalman filter and operates by linearising the system and measurement equation about an estimate of the current mean and state covariance matrix.

The discrete-time extended Kalman filter can be derived for a general nonlinear system model of the form:

$$\mathbf{x}_k = \mathbf{f}_{k-1}(\mathbf{x}_{k-1}, \mathbf{u}_{k-1}, \mathbf{w}_{k-1}) \tag{4.1}$$
$$\mathbf{y}_k = \mathbf{h}_k(\mathbf{x}_k, \mathbf{v}_k) \tag{4.2}$$
$$\mathbf{w}_k \sim \mathcal{N}(\mathbf{0}, \mathbf{Q}_k) \tag{4.3}$$
$$\mathbf{v}_k \sim \mathcal{N}(\mathbf{0}, \mathbf{R}_k) \tag{4.4}$$

A first-order Taylor series expansion of the state equation around $\mathbf{x}_{k-1} = \hat{\mathbf{x}}_{k-1}^+$ and $\mathbf{w}_{k-1} = \mathbf{0}$ is performed to obtain the following relations [28]:

$$\mathbf{x}_k = \mathbf{f}_{k-1}(\hat{\mathbf{x}}_{k-1}^+, \mathbf{u}_{k-1}, \mathbf{0}) + \left.\frac{\partial \mathbf{f}_{k-1}}{\partial \mathbf{x}}\right|_{\hat{\mathbf{x}}_{k-1}^+} (\mathbf{x}_{k-1} - \hat{\mathbf{x}}_{k-1}^+) + \left.\frac{\partial \mathbf{f}_{k-1}}{\partial \mathbf{w}}\right|_{\hat{\mathbf{x}}_{k-1}^+} \mathbf{w}_{k-1} \tag{4.5}$$
$$= \mathbf{f}_{k-1}(\hat{\mathbf{x}}_{k-1}^+, \mathbf{u}_{k-1}, \mathbf{0}) + \mathbf{F}_{k-1}(\mathbf{x}_{k-1} - \hat{\mathbf{x}}_{k-1}^+) + \mathbf{L}_{k-1}\mathbf{w}_{k-1} \tag{4.6}$$
$$= \mathbf{F}_{k-1}\mathbf{x}_{k-1} + \left(\mathbf{f}_{k-1}(\hat{\mathbf{x}}_{k-1}^+, \mathbf{u}_{k-1}, \mathbf{0}) - \mathbf{F}_{k-1}\hat{\mathbf{x}}_{k-1}^+\right) + \mathbf{L}_{k-1}\mathbf{w}_{k-1} \tag{4.7}$$
$$= \mathbf{F}_{k-1}\mathbf{x}_{k-1} + \widetilde{\mathbf{u}}_{k-1} + \widetilde{\mathbf{w}}_{k-1} \tag{4.8}$$

$\mathbf{F}_{k-1}$ and $\mathbf{L}_{k-1}$ are defined by the above equation. The known signal $\widetilde{\mathbf{u}}_k$ and the noise signal $\widetilde{\mathbf{w}}_k$ are defined as [28]:

$$\widetilde{\mathbf{u}}_k = \mathbf{f}_k(\hat{\mathbf{x}}_k^+, \mathbf{u}_k, \mathbf{0}) - \mathbf{F}_k\hat{\mathbf{x}}_k^+ \tag{4.9}$$
$$\widetilde{\mathbf{w}}_k \sim \mathcal{N}(\mathbf{0}, \mathbf{L}_k\mathbf{Q}_k\mathbf{L}_k^T) \tag{4.10}$$

Likewise, the measurement equation is linearised around $\mathbf{x}_k = \hat{\mathbf{x}}_k^-$ and $\mathbf{v}_k = \mathbf{0}$ to obtain the relations:

$$\mathbf{y}_k = \mathbf{h}_k(\hat{\mathbf{x}}_k^-, \mathbf{0}) + \left.\frac{\partial \mathbf{h}_k}{\partial \mathbf{x}}\right|_{\hat{\mathbf{x}}_k^-} (\mathbf{x}_k - \hat{\mathbf{x}}_k^-) + \left.\frac{\partial \mathbf{h}_k}{\partial \mathbf{v}}\right|_{\hat{\mathbf{x}}_k^-} \mathbf{v}_k \tag{4.11}$$

$$= \mathbf{h}_k(\hat{\mathbf{x}}_k^-, \mathbf{0}) + \mathbf{H}_k(\mathbf{x}_k - \hat{\mathbf{x}}_k^-) + \mathbf{M}_k\mathbf{v}_k \tag{4.12}$$

$$= \mathbf{H}_k\mathbf{x}_k + \left(\mathbf{h}_k(\hat{\mathbf{x}}_k^-, \mathbf{0}) - \mathbf{H}_k\hat{\mathbf{x}}_k^-\right) + \mathbf{M}_k\mathbf{v}_k \tag{4.13}$$

$$= \mathbf{H}_k\mathbf{x}_k + \mathbf{z}_k + \widetilde{\mathbf{v}}_k \tag{4.14}$$

$\mathbf{H}_k$ and $\mathbf{M}_k$ are defined by the above equation. The known signal $\mathbf{z}_k$ and the noise signal $\widetilde{\mathbf{v}}_k$ are defined as:

$$\mathbf{z}_k = \mathbf{h}_k(\hat{\mathbf{x}}_k^-, \mathbf{0}) - \mathbf{H}_k\hat{\mathbf{x}}_k^- \tag{4.15}$$

$$\widetilde{\mathbf{v}}_k \sim \mathcal{N}(\mathbf{0}, \mathbf{M}_k\mathbf{R}_k\mathbf{M}_k^T) \tag{4.16}$$

A linear state-space system equation and a linear measurement equation have thus been derived. This means that the standard linear Kalman filter equations can be implemented to estimate the state. This results in the following equations for the discrete-time extended Kalman filter:

$$\mathbf{P}_k^- = \mathbf{F}_{k-1}\mathbf{P}_{k-1}^+\mathbf{F}_{k-1}^T + \mathbf{L}_{k-1}\mathbf{Q}_{k-1}\mathbf{L}_{k-1}^T \tag{4.17}$$

$$\mathbf{K}_k = \mathbf{P}_k^-\mathbf{H}_k^T(\mathbf{H}_k\mathbf{P}_k^-\mathbf{H}_k^T + \mathbf{M}_k\mathbf{R}_k\mathbf{M}_k^T)^{-1} \tag{4.18}$$

$$\hat{\mathbf{x}}_k^- = \mathbf{f}_{k-1}(\hat{\mathbf{x}}_{k-1}^+, \mathbf{u}_{k-1}, \mathbf{0}) \tag{4.19}$$

$$\mathbf{z}_k = \mathbf{h}_k(\hat{\mathbf{x}}_{k-1}^-, \mathbf{0}) - \mathbf{H}_k\hat{\mathbf{x}}_k^- \tag{4.20}$$

$$\hat{\mathbf{x}}_k^+ = \hat{\mathbf{x}}_k^- + \mathbf{K}_k(\mathbf{y}_k - \mathbf{H}_k\hat{\mathbf{x}}_k^- - \mathbf{z}_k) \tag{4.21}$$

$$= \hat{\mathbf{x}}_k^- + \mathbf{K}_k\left(\mathbf{y}_k - \mathbf{h}_k(\hat{\mathbf{x}}_k^-, \mathbf{0})\right) \tag{4.22}$$

$$\mathbf{P}_k^+ = (\mathbf{I} - \mathbf{K}_k\mathbf{H}_k)\mathbf{P}_k^-(\mathbf{I} - \mathbf{K}_k\mathbf{H}_k)^T + \mathbf{K}_k\mathbf{R}_k\mathbf{K}_k^T \tag{4.23}$$

4.1.1 The discrete-time extended Kalman filter algorithm

The discrete-time EKF can be summarised as follows [28]:

(i) The system and measurement equations are given as:

$$\mathbf{x}_k = \mathbf{f}_{k-1}(\mathbf{x}_{k-1}, \mathbf{u}_{k-1}, \mathbf{w}_{k-1}) \tag{4.24}$$

$$\mathbf{y}_k = \mathbf{h}_k(\mathbf{x}_k, \mathbf{v}_k) \tag{4.25}$$

$$\mathbf{w}_k \sim \mathcal{N}(\mathbf{0}, \mathbf{Q}_k) \tag{4.26}$$

$$\mathbf{v}_k \sim \mathcal{N}(\mathbf{0}, \mathbf{R}_k) \tag{4.27}$$

(ii) The filter is initialized as follows:

$$\hat{\mathbf{x}}_0^+ = E[\mathbf{x}_0] \tag{4.28}$$
$$\mathbf{P}_0^+ = E[(\mathbf{x}_0 - \hat{\mathbf{x}}_0^+)(\mathbf{x}_0 - \hat{\mathbf{x}}_0^+)^T] \tag{4.29}$$

(iii) For $k = 1, 2, ...$ the following is performed.

(a) The following partial derivative matrices are computed:

$$\mathbf{F}_{k-1} = \left.\frac{\partial \mathbf{f}_{k-1}}{\partial \mathbf{x}_{k-1}}\right|_{\hat{\mathbf{x}}_{k-1}^+} \tag{4.30}$$
$$\mathbf{L}_{k-1} = \left.\frac{\partial \mathbf{f}_{k-1}}{\partial \mathbf{w}_{k-1}}\right|_{\hat{\mathbf{x}}_{k-1}^+} \tag{4.31}$$

(b) The time update of the state estimate and estimation-error covariance are performed as follows:

$$\mathbf{P}_k^- = \mathbf{F}_{k-1}\mathbf{P}_{k-1}^+\mathbf{F}_{k-1}^T + \mathbf{L}_{k-1}\mathbf{Q}_{k-1}\mathbf{L}_{k-1}^T \tag{4.32}$$
$$\hat{\mathbf{x}}_k^- = \mathbf{f}_{k-1}(\hat{\mathbf{x}}_{k-1}^+, \mathbf{u}_{k-1}, \mathbf{0}) \tag{4.33}$$

(c) The following partial derivative matrices are computed:

$$\mathbf{H}_k = \left.\frac{\partial \mathbf{h}_k}{\partial \mathbf{x}_k}\right|_{\hat{\mathbf{x}}_k^-} \tag{4.34}$$
$$\mathbf{M}_k = \left.\frac{\partial \mathbf{h}_k}{\partial \mathbf{v}_k}\right|_{\hat{\mathbf{x}}_k^-} \tag{4.35}$$

(d) The measurement update of the state estimate and estimation-error covariance are performed as follows:

$$\mathbf{K}_k = \mathbf{P}_k^-\mathbf{H}_k^T(\mathbf{H}_k\mathbf{P}_k^-\mathbf{H}_k^T + \mathbf{M}_k\mathbf{R}_k\mathbf{M}_k^T)^{-1} \tag{4.36}$$
$$\hat{\mathbf{x}}_k^+ = \hat{\mathbf{x}}_k^- + \mathbf{K}_k\Big(\mathbf{y}_k - \mathbf{h}_k(\hat{\mathbf{x}}_k^-, \mathbf{0})\Big) \tag{4.37}$$
$$\mathbf{P}_k^+ = (\mathbf{I} - \mathbf{K}_k\mathbf{H}_k)\mathbf{P}_k^-(\mathbf{I} - \mathbf{K}_k\mathbf{H}_k)^T + \mathbf{K}_k\mathbf{R}_k\mathbf{K}_k^T \tag{4.38}$$

It can be noted that other equivalent expressions can be used for $\mathbf{K}_k$ and $\mathbf{P}_k^+$.

4.2 The unscented Kalman filter

As stated previously, the extended Kalman filter is the most widely applied state estimation algorithm for nonlinear systems. However, the EKF can be difficult to tune and often gives unreliable estimates if the system nonlinearities are severe. This is because the EKF relies on linearisation to propagate the mean and covariance of the state. A

more accurate alternative is the Unscented Kalman Filter (UKF), which is an extension of the Kalman filter that reduces the linearisation errors of the EKF. The use of the UKF can provide significant improvements over the EKF [28].

The problem with nonlinear systems is that it is difficult to transform a probability density function through a general nonlinear function. The extended Kalman filter works on the principle that a linearised transformation of means and covariances is approximately equal to the true nonlinear transformation, but in some cases this approximation may be unsatisfactory.

An unscented transformation is based on two fundamental principles. First, it is easy to perform a nonlinear transformation on a single point (rather than an entire pdf). Second, it is not too hard to find a set of individual points in the state space whose sample pdf approximates the true pdf of a state vector.

Taking these two ideas together, if the mean $\overline{\mathbf{x}}$ and covariance $\mathbf{P}$ of a vector $\mathbf{x}$ are known, a set of deterministic vectors called sigma points can be selected, such that their ensemble mean and covariance are equal to $\overline{\mathbf{x}}$ and $\mathbf{P}$. The known nonlinear function is then applied to each deterministic vector to obtain transformed vectors. The ensemble mean and covariance of the transformed vectors will give a good estimate of the true mean and covariance of $\mathbf{y}$.

Suppose that $\mathbf{x}$ is an $n \times 1$ vector that is transformed by a nonlinear function $\mathbf{y} = \mathbf{h}(\mathbf{x})$. $2n$ sigma points $\mathbf{x}^{(i)}$ are selected as follows [28]:

$$\mathbf{x}^{(i)} = \overline{\mathbf{x}} + \widetilde{\mathbf{x}}^{(i)} \quad i = 1, ..., 2n \tag{4.39}$$

$$\widetilde{\mathbf{x}}^{(i)} = \left(\sqrt{n\mathbf{P}}\right)_i^T \quad i = 1, ..., n \tag{4.40}$$

$$\widetilde{\mathbf{x}}^{(n+i)} = -\left(\sqrt{n\mathbf{P}}\right)_i^T \quad i = 1, ..., n \tag{4.41}$$

where $\sqrt{n\mathbf{P}}$ is the matrix square root of $n\mathbf{P}$ such that $(\sqrt{n\mathbf{P}})^T(\sqrt{n\mathbf{P}}) = n\mathbf{P}$, and $(\sqrt{n\mathbf{P}})_i$ is the i-th row of $\sqrt{n\mathbf{P}}$.

It can be demonstrated that by choosing the values of sigma points as defined above, the approximated mean matches the true mean correctly up to the third order, whereas linearisation only matches the true mean up to the first order. The greatest advantage of the unscented transformation (relative to linearisation) is then the increased accuracy of the transformation of the mean.

4.2.1 The unscented transformation

(i) An n-element vector $\mathbf{x}$ with known mean $\overline{\mathbf{x}}$ and covariance $\mathbf{P}$ is considered [28]. Given a known nonlinear transformation $\mathbf{y} = \mathbf{h}(\mathbf{x})$, the mean and covariance of $\mathbf{y}$, denoted as $\overline{\mathbf{y}}_u$ and $\mathbf{P}_u$, shall be estimated.

(ii) $2n$ sigma point vectors $\mathbf{x}^{(i)}$ are formed as follows:

$$\mathbf{x}^{(i)} = \overline{\mathbf{x}} + \widetilde{\mathbf{x}}^{(i)} \quad i = 1, ..., 2n \tag{4.42}$$

$$\widetilde{\mathbf{x}}^{(i)} = \left(\sqrt{n\mathbf{P}}\right)_i^T \quad i = 1, ..., n \tag{4.43}$$

$$\widetilde{\mathbf{x}}^{(n+i)} = -\left(\sqrt{n\mathbf{P}}\right)_i^T \quad i = 1, ..., n \tag{4.44}$$

where $\sqrt{n\mathbf{P}}$ is the matrix square root of $n\mathbf{P}$ such that $(\sqrt{n\mathbf{P}})^T\sqrt{n\mathbf{P}} = n\mathbf{P}$, and $(\sqrt{n\mathbf{P}})_i$ is the i-th row of $\sqrt{n\mathbf{P}}$.

(iii) The sigma points are transformed as follows:

$$\mathbf{y}^{(i)} = \mathbf{h}(\mathbf{x}^{(i)}) \quad i = 1, ..., 2n \tag{4.45}$$

(iv) The mean and covariance of $\mathbf{y}$ are approximated as follows:

$$\overline{\mathbf{y}}_u = \frac{1}{2n} \sum_{i=1}^{2n} \mathbf{y}^{(i)} \tag{4.46}$$

$$\mathbf{P}_u = \frac{1}{2n} \sum_{i=1}^{2n} \left(\mathbf{y}^{(i)} - \overline{\mathbf{y}}_u\right)\left(\mathbf{y}^{(i)} - \overline{\mathbf{y}}_u\right)^T \tag{4.47}$$

The unscented transformation can be generalised to give the unscented Kalman filter. Indeed, the Kalman filter algorithm attempts to propagate the mean and covariance of a system using a time update and a measurement update. If the system is linear, then the mean and covariance can be exactly updated with the Kalman filter. If the filter is nonlinear, then the mean and covariance can be approximately updated with the extended Kalman filter. However, the EKF is based on linearisation, and previously it was shown that unscented transformations are more accurate than linearisation for propagating means and covariances. Therefore, the EKF equations are simply replaced with unscented transformations to obtain the UKF algorithm.

4.2.2 The unscented Kalman filter algorithm

The UKF can be summarised as follows [28]:

(i) The n-state discrete-time nonlinear system with additive noise is given by:

$$\mathbf{x}_k = \mathbf{f}(\mathbf{x}_{k-1}, \mathbf{u}_{k-1}, t_{k-1}) + \mathbf{w}_{k-1} \tag{4.48}$$

$$\mathbf{y}_k = \mathbf{h}(\mathbf{x}_k, t_k) + \mathbf{v}_k \tag{4.49}$$

$$\mathbf{w}_k \sim \mathcal{N}(\mathbf{0}, \mathbf{Q}_k) \tag{4.50}$$

$$\mathbf{v}_k \sim \mathcal{N}(\mathbf{0}, \mathbf{R}_k) \tag{4.51}$$

(ii) The UKF is initalized as follows:

$$\hat{\mathbf{x}}_0^+ = E[\mathbf{x}_0] \tag{4.52}$$

$$\mathbf{P}_0^+ = E[(\mathbf{x}_0 - \hat{\mathbf{x}}_0^+)(\mathbf{x}_0 - \hat{\mathbf{x}}_0^+)^T] \tag{4.53}$$

(iii) The following time-update equations are used to propagate the state estimate and covariance from one measurement to the next:

(a) To propagate from time step $k-1$ to k, the sigma points $\mathbf{x}_{k-1}^{(i)}$ are first chosen; the current best guess for the mean and covariance of $\mathbf{x}_k$ are respectively $\hat{\mathbf{x}}_{k-1}^+$ and $\mathbf{P}_{k-1}^+$:

$$\hat{\mathbf{x}}_{k-1}^{(i)} = \hat{\mathbf{x}}_{k-1}^{+} + \widetilde{\mathbf{x}}^{(i)} \quad i = 1, ..., 2n \tag{4.54}$$

$$\widetilde{\mathbf{x}}^{(i)} = \left(\sqrt{n\mathbf{P}_{k-1}^{+}}\right)_i^T \quad i = 1, ..., n \tag{4.55}$$

$$\widetilde{\mathbf{x}}^{(n+i)} = -\left(\sqrt{n\mathbf{P}_{k-1}^{+}}\right)_i^T \quad i = 1, ..., n \tag{4.56}$$

(b) The known nonlinear system equation $\mathbf{f}(\cdot)$ is used to transform the sigma points into $\hat{\mathbf{x}}_k^{(i)}$ vectors:

$$\hat{\mathbf{x}}_k^{(i)} = \mathbf{f}(\hat{\mathbf{x}}_{k-1}^{(i)}, \mathbf{u}_{k-1}, t_{k-1}) \tag{4.57}$$

(c) The $\hat{\mathbf{x}}_k^{(i)}$ vectors are combined to obtain the *a priori* state estimate at time k:

$$\hat{\mathbf{x}}_k^{-} = \frac{1}{2n}\sum_{i=1}^{2n}\hat{\mathbf{x}}_k^{(i)} \tag{4.58}$$

(d) The *a priori* error covariance is estimated as seen in the unscented transformation. However, $\mathbf{Q}_{k-1}$ should be added to the end of the equation to take the process noise into account:

$$\mathbf{P}_k^{-} = \frac{1}{2n}\sum_{i=1}^{2n}\left(\hat{\mathbf{x}}_k^{(i)} - \hat{\mathbf{x}}_k^{-}\right)\left(\hat{\mathbf{x}}_k^{(i)} - \hat{\mathbf{x}}_k^{-}\right)^T + \mathbf{Q}_{k-1} \tag{4.59}$$

(iv) After the time-update equations construction, the measurement-update equations are implemented.

(a) The sigma points $\mathbf{x}_k^{(i)}$ are chosen; the current best guess for the mean and covariance of $\mathbf{x}_k$ are now respectively $\hat{\mathbf{x}}_k^{-}$ and $\mathbf{P}_k^{-}$:

$$\hat{\mathbf{x}}_k^{(i)} = \hat{\mathbf{x}}_k^{-} + \widetilde{\mathbf{x}}^{(i)} \quad i = 1, ..., 2n \tag{4.60}$$

$$\widetilde{\mathbf{x}}^{(i)} = \left(\sqrt{n\mathbf{P}_k^{-}}\right)_i^T \quad i = 1, ..., n \tag{4.61}$$

$$\widetilde{\mathbf{x}}^{(n+i)} = -\left(\sqrt{n\mathbf{P}_k^{-}}\right)_i^T \quad i = 1, ..., n \tag{4.62}$$

This step can be omitted if desired. That is, instead of generating new sigma points, the ones that were obtained from the time update can be reused. This will save computational effort but will sacrifice performance.

(b) The known nonlinear measurement equation $\mathbf{h}(\cdot)$ is used to transform the sigma points into $\hat{\mathbf{y}}_k^{(i)}$ vectors (predicted measurements):

$$\hat{\mathbf{y}}_k^{(i)} = \mathbf{h}(\hat{\mathbf{x}}_k^{(i)}, t_k) \tag{4.63}$$

(c) The $\hat{\mathbf{y}}_k^{(i)}$ vectors are combined to obtain the predicted measurement at time k:

$$\hat{\mathbf{y}}_k = \frac{1}{2n}\sum_{i=1}^{2n}\hat{\mathbf{y}}_k^{(i)} \tag{4.64}$$

(d) The covariance of the predicted measurement is estimated as shown in the unscented transformation. However, $\mathbf{R}_k$ should be added to the end of the equation to take the measurement noise into account:

$$\mathbf{P}_{\mathbf{y}} = \frac{1}{2n}\sum_{i=1}^{2n}\left(\hat{\mathbf{y}}_k^{(i)} - \hat{\mathbf{y}}_k^{-}\right)\left(\hat{\mathbf{y}}_k^{(i)} - \hat{\mathbf{y}}_k^{-}\right)^T + \mathbf{R}_k \tag{4.65}$$

(e) The cross covariance between $\hat{\mathbf{x}}_k^-$ and $\hat{\mathbf{y}}_k$ is estimated:

$$\mathbf{P}_{\mathbf{xy}} = \frac{1}{2n}\sum_{i=1}^{2n}\left(\hat{\mathbf{x}}_k^{(i)} - \hat{\mathbf{x}}_k^{-}\right)\left(\hat{\mathbf{y}}_k^{(i)} - \hat{\mathbf{y}}_k^{-}\right)^T \tag{4.66}$$

(f) The measurement update of the state estimate can be performed using the normal Kalman filter equations [28]:

$$\mathbf{K}_k = \mathbf{P}_{\mathbf{xy}}\mathbf{P}_{\mathbf{y}}^{-1} \tag{4.67}$$
$$\hat{\mathbf{x}}_k^+ = \hat{\mathbf{x}}_k^- + \mathbf{K}_k(\mathbf{y}_k - \hat{\mathbf{y}}_k) \tag{4.68}$$
$$\mathbf{P}_k^+ = \mathbf{P}_k^- - \mathbf{K}_k\mathbf{P}_{\mathbf{y}}\mathbf{K}_k^T \tag{4.69}$$

The algorithm above assumes that the process and measurement equations are linear with respect to the noise. In general, the process and measurement equations may have noise that enters the process and measurement equations nonlinearly. That is:

$$\mathbf{x}_k = \mathbf{f}(\mathbf{x}_{k-1}, \mathbf{u}_{k-1}, \mathbf{w}_{k-1}, t_{k-1}) \tag{4.70}$$
$$\mathbf{y}_k = \mathbf{h}(\mathbf{x}_k, \mathbf{v}_k, t_k) \tag{4.71}$$

In this case, the UKF algorithm presented above is not rigorous because it treats the noise as additive. To handle this situation, the noise can be augmented onto the state vector:

$$\mathbf{x}_k^{aug} = \begin{bmatrix}\mathbf{x}_k \\ \mathbf{w}_k \\ \mathbf{v}_k\end{bmatrix} \tag{4.72}$$

Then the UKF can be used to estimate the augmented state $\mathbf{x}_k^{aug}$. The UKF is initialized as:

$$\hat{\mathbf{x}}_0^{aug\,+} = \begin{bmatrix}E[\mathbf{x}_0] \\ \mathbf{0} \\ \mathbf{0}\end{bmatrix} \tag{4.73}$$

$$\mathbf{P}_0^{aug\,+} = \begin{bmatrix}E[(\mathbf{x}_0 - \hat{\mathbf{x}}_0)(\mathbf{x}_0 - \hat{\mathbf{x}}_0)^T] & 0 & 0 \\ 0 & \mathbf{Q}_0 & 0 \\ 0 & 0 & \mathbf{R}_0\end{bmatrix} \tag{4.74}$$

Then the UKF algoritm presented above can be used, with the only exception that $\mathbf{Q}_{k-1}$ and $\mathbf{R}_k$ shall be removed from the equations, since the augmented mean and covariance are being estimated.

4.3 The particle filter

The particle filter is a statistical, brute-force approach to estimation that often works well for problems that are difficult for the conventional Kalman filter, i.e. systems that are highly nonlinear [28].

As discussed previously, the extended Kalman filter is the most widely applied state estimation algorithm for nonlinear systems. However, the EKF can be difficult to tune and often gives unreliable estimates if the system nonlinearities are severe. This is because the EKF relies on linearisation to propagate the mean and covariance of the state. On the contrary, the unscented Kalman filter reduces linearisation errors. The UKF can provide significant improvements in estimation accuracy over the EKF. However, the UKF is still only an approximated nonlinear estimator. The EKF estimates the mean of a nonlinear system with first-order accuracy, and the UKF improves this by providing an estimate with higher-order accuracy. However, this simply defers the inevitable divergence that will occur when the system or measurement nonlinearities become too severe.

The particle filter is a completely nonlinear state estimator. The price that must be paid for the high performance of the particle filter is an increased level of computational effort. There may be problems for which the improved performance of the particle filter is worth the increased computational effort. There may be other applications for which the improved performance is not worth the extra computational effort. These trade-offs are problem-dependent and must be investigated on an individual basis [28].

The particle filter was invented to numerically implement the Bayesian estimator. At the beginning of the estimation problem, a given number N of state vectors based on the initial pdf $p(\mathbf{x}_0)$ (which is assumed to be known) are randomly generated. These state vectors are called particles and are denoted as $\mathbf{x}_{0,i}^{+}$ $(i = 1, ..., N)$. At each time step $k = 1, 2, ...$, the particles are propagated to the next time step using the process equation $\mathbf{f}(\cdot)$:

$$\mathbf{x}_{k,i}^{-} = \mathbf{f}_{k-1}(\mathbf{x}_{k-1,i}^{+}, \mathbf{w}_{k-1,i}) \quad i = 1, ..., N \tag{4.75}$$

where each $\mathbf{w}_{k-1,i}$ noise vector is randomly generated on the basis of the known pdf of $\mathbf{w}_{k-1}$. After the measurement at time k is received, the conditional relative likelihood of each particle $\mathbf{x}_{k,i}^{-}$ is computed. That is, the pdf $p(\mathbf{y}_k|\mathbf{x}_{k,i}^{-})$ is evaluated. This can be done if the nonlinear measurement equation and the pdf of the measurement noise are known. For example, if an m-dimensional measurement equation is given as $\mathbf{y}_k = \mathbf{h}(\mathbf{x}_k) + \mathbf{v}_k$ and $\mathbf{v}_k \sim \mathcal{N}(\mathbf{0}, \mathbf{R})$ then a relative likelihood q_i that the measurement is equal to a specific measurement $\mathbf{y}^*$, given the premise that $\mathbf{x}_k$ is equal to the particle $\mathbf{x}_{k,i}^{-}$, can be computed as follows [28]:

$$q_i = P[(\mathbf{y}_k = \mathbf{y}^*)|(\mathbf{x}_k = \mathbf{x}_{k,i}^-)] \tag{4.76}$$
$$= P[\mathbf{v}_k = \mathbf{y}^* - \mathbf{h}(\mathbf{x}_{k,i}^-)] \tag{4.77}$$
$$\sim \frac{1}{(2\pi)^{m/2}|\mathbf{R}|^{1/2}} \exp\left(\frac{-\big(\mathbf{y}^* - \mathbf{h}(\mathbf{x}_{k,i}^-)\big)^T \mathbf{R}^{-1} \big(\mathbf{y}^* - \mathbf{h}(\mathbf{x}_{k,i}^-)\big)}{2}\right) \tag{4.78}$$

The symbol $\sim$ in the above equation means that the probability is not really given by the expression on the right side, but that the probability is directly proportional to the right side. So if this equation is used for all the particle $\mathbf{x}_{k,i}^-$ $(i = 1, ..., N)$, then the relative likelihoods that the state is equal to each particle will be correct.

The relative likelihoods obtained before are then normalized as follows:

$$q_i = \frac{q_i}{\sum_{j=1}^N q_j} \tag{4.79}$$

This ensures that the sum of all the likelihoods is equal to one. Next, the particles are resampled from the computed likelihoods. That is, a brand new set of particles $\mathbf{x}_{k,i}^+$ that are randomly generated on the basis of the relative likelihoods q_i are computed. This can be done several different ways. One straightforward (but not necessarily efficient) way is the following [28]. For $i = 1, ..., N$, the following two steps are performed.

(i) A random number r that is uniformely distributed on [0, 1] is generated.

(ii) The likelihoods q_i are accumulated into a sum, one at a time, until the accumulated sum is greater than r. That is, if $\sum_{m=1}^{j-1} q_m < r$ but $\sum_{m=1}^{j} q_m \geq r$, the new particle $\mathbf{x}_{k,i}^+$ is then set equal to the old particle $\mathbf{x}_{k,j}^-$.

It can be shown that using this resampling technique, the ensemble pdf of the new particles $\mathbf{x}_{k,i}^+$ tends to the pdf $p(\mathbf{x}_k|\mathbf{Y}_k)$ as the number of samples N approaches ∞. The resampling step can be summarised as follows:

$$\mathbf{x}_{k,i}^+ = \mathbf{x}_{k,j}^- \quad \text{with probability } q_j \quad (i, j = 1, ..., N) \tag{4.80}$$

The computational effort of the particle filter is often a bottleneck to its implementation. More efficient resampling methods can be implemented. For example, the *a priori* samples $\mathbf{x}_{k,j}^-(j = 1, ..., N)$ could be accepted as *a posteriori* samples with a probability that is proportional to q_j. However, in this case additional logic must be incorporated to maintain a constant sample size N.

A set of particles $\mathbf{x}_{k,i}^+$ that are distributed according to the pdf $p(\mathbf{x}_k|\mathbf{y}_k)$ have then been generated. Any desired statistical measure of this pdf can be computed. For example, the expected value $E[(\mathbf{x}_k|\mathbf{Y}_k)]$ can be approximated as the algebraic mean of the particles:

$$E[(\mathbf{x}_k|\mathbf{Y}_k)] = \frac{1}{N} \sum_{i=0}^{N} \mathbf{x}_{k,i}^+ \tag{4.81}$$

4.3.1 The particle filter algorithm

The particle filter can be summarised as follows [28]:

(i) The system and measurement equations are given as follows:

$$\mathbf{x}_k = \mathbf{f}_{k-1}(\mathbf{x}_{k-1}, \mathbf{w}_{k-1}) \tag{4.82}$$
$$\mathbf{y}_k = \mathbf{h}_k(\mathbf{x}_k, \mathbf{v}_k) \tag{4.83}$$

where $\{\mathbf{w}_k\}$ and $\{\mathbf{v}_k\}$ are independent white noise processes with known pdfs.

(ii) Assuming that the pdf of the initial state $p(\mathbf{x}_0)$ is known, N initial particles are randomly generated on the basis of the pdf $p(\mathbf{x}_0)$. These particles are denoted $\mathbf{x}_{0,i}^+$ $(i = 1, ..., N)$. The parameter N is chosen by the user as a trade-off between computational effort and estimation accuracy.

(iii) For $k = 1, 2, ...$, the following is performed.

(a) The time propagation step to obtain *a priori* particles $\mathbf{x}_{k,i}^-$ using the known process equation and the known pdf of the process noise is carried out:

$$\mathbf{x}_{k,i}^- = \mathbf{f}_{k-1}(\mathbf{x}_{k-1,i}^+, \mathbf{w}_{k-1,i}) \quad i = 1, ..., N \tag{4.84}$$

where each $\mathbf{w}_{k-1,i}$ noise vector is randomly generated on the basis of the known pdf of $\mathbf{w}_{k-1}$.

(b) The relative likelihood q_i of each particle $\mathbf{x}_{k,i}^-$ conditioned on the measurement $\mathbf{y}_k$ is computed. This is done by evaluating the pdf $p(\mathbf{y}_k|\mathbf{x}_{k,i}^-)$ on the basis of the nonlinear measurement equation and the pdf of the measurement noise.

(c) The relative likelihoods obtained in the previous step are scaled as follows:

$$q_i = \frac{q_i}{\sum_{j=1}^{N} q_j} \tag{4.85}$$

The sum of all the likelihoods is now equal to one.

(d) A set of *a posteriori* particles $\mathbf{x}_{k,i}^+$ are generated on the basis of the relative likelihoods q_i. This is called resampling step.

(e) The set of particles $\mathbf{x}_{k,i}^+$ that are distributed according to the pdf $p(\mathbf{x}_k|\mathbf{Y}_k)$ is now available and any desired statistical measure of this pdf can be computed, such as the mean and the covariance.

One of the main implementation issues that arises in the application of particle filters is sample impoverishment [28]. It occurs when the region of state space in which the pdf $p(\mathbf{y}_k|\mathbf{x}_k)$ has significant values does not overlap with the pdf $p(\mathbf{x}_k|\mathbf{Y}_{k-1})$. This means that if all of the *a priori* particles are distributed according to $p(\mathbf{x}|\mathbf{Y}_{k-1})$, and the computed pdf $p(\mathbf{y}_k|\mathbf{x}_k)$ is then used to resample the particles, only a few particles will be resampled to become *a posteriori* particles. This is because only a few of the *a priori* particles will be in a region of the state space where the computed pdf $p(\mathbf{y}_k|\mathbf{x}_k)$ has a significant value. This means that the resampling process will select only a few distinct *a priori* particles to become *a posteriori* particles. Eventually, all of the particles will collapse to the same value. This problem will be exacerbated if the measurements are not consistent with the process model (modeling errors). This can be overcome by a brute-force method of simply increasing the number of particles N, but this can in turn quickly lead to unreasonable computational demands, and often simply delays the inevitable sample impoverishment.

Chapter 5

Harmonic estimation of a linear system with one degree of freedom

5.1 System description

Any structure can be very roughly approximated as a one-dimensional system with only one degree of freedom. Such system is made up of a moving concentrated mass with structure stiffness and damping characteristics modeled as a spring and a damper respectively. Despite the extremely simplistic approach, this modeling choice can provide some insightful information before dealing with more complex systems. Since the purpose of the study is the estimation of disturbances acting on a system, a harmonic exogenous variable is considered as the uncontrolled input, as shown in Figure 5.1.

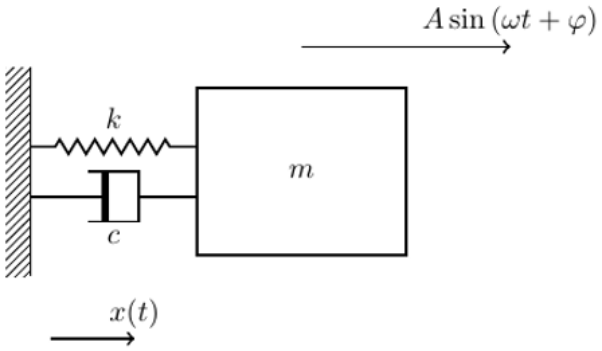

Figure 5.1: Physical model of a one-dimensional system with one degree of freedom

In particular, the quantities of interest are the amplitude A, the frequency ω, and the initial phase φ of the disturbance, which are assumed to be constant. The value of such quantities, along with the ones related to the system properties and the initial conditions of the system, are listed in table 5.1.

The motion of the system is described by the function $x(t)$, which represents the mass position over time and can be derived in time to obtain the mass velocity $\dot{x}(t)$ and the acceleration $\ddot{x}(t)$. The system equation of motion can then be described by the following equation:

$$m\ddot{x}(t) + c\dot{x}(t) + kx(t) = A\sin(\omega t + \varphi) \tag{5.1}$$

In addition, the system is equipped with a velocity sensor which provides data about the variable $\dot{x}(t)$ that in turn are used to estimate the disturbance amplitude and fre-

	System parameter	Value
m	Body mass [kg]	2
k	Spring constant [N/m]	1
c	Damping coefficient [Nm/s]	0.5
ω_0	Natural frequency [rad/s]	0.7071
ξ	Damping ratio [-]	0.1768
x_0	Initial position [m]	0
$\dot{x}_0$	Initial velocity [m/s]	1
A	Disturbance amplitude [N]	10
ω	Disturbance frequency [rad/s]	0.3
φ	Disturbance initial phase [deg]	0
$\omega_d \in [\omega_1 \quad \omega_2]$	Assumed disturbance frequency range [rad/s]	$[0.1 \quad 1]$
ω_n	Assumed noise frequency [rad/s]	$\gg 100$
$\lvert n(t) \rvert$	Assumed average noise amplitude [m/s]	10^{-2}

Table 5.1: One dimensional system parameters

quency by means of specific estimation techniques. The choice of introducing this particular sensor is explained by the fact that in the real system, the disturbance acting on the satellite and generated by the gearbox is required to be estimated from information delivered by on-board gyroscopes. Any sensor is intrinsically corrupted by some noise $n(t)$, which in this example is assumed to be white.

The output equation of the one-dimensional system can then be written as:

$$y(t) = \dot{x}(t) + n(t) \tag{5.2}$$

The motion of the mass can be computed analytically by solving the differential equation (5.1), whose solution for $\varphi = 0$ is given by the following expression:

$$\begin{aligned} x(t) = e^{-\xi\omega_0 t}[a\cos(\omega_d t) + b\sin(\omega_d t)] + \\ + \frac{A/m}{\sqrt{(2\xi\omega_0\omega)^2 + (\omega^2 - \omega_0^2)^2}} \cos\left[\omega t - \arctan\left(\frac{m\omega^2 - k}{c\omega}\right) + \pi\right] \end{aligned} \tag{5.3}$$

where $\omega_d = \omega_0\sqrt{1-\xi^2}$, while a and b depend on the initial conditions and can be computed as:

$$a = x_0 + \frac{Ac\omega}{(c\omega)^2 + (m\omega^2 - k)^2} \tag{5.4}$$

$$b = \frac{1}{\omega_d}\left[\dot{x}_0 + a\xi\omega_0 + \frac{A\omega(m\omega^2 - k)}{(c\omega)^2 + (m\omega^2 - k)^2}\right] \tag{5.5}$$

A simulation of both position $x(t)$ and velocity $\dot{x}(t)$ of the mass over time is depicted in Figure 5.2.

5.2 Direct estimation

The estimation of the harmonic disturbance acting on the system can be obtained by evaluating the singular quantities that characterise such disturbance, i.e. the amplitude

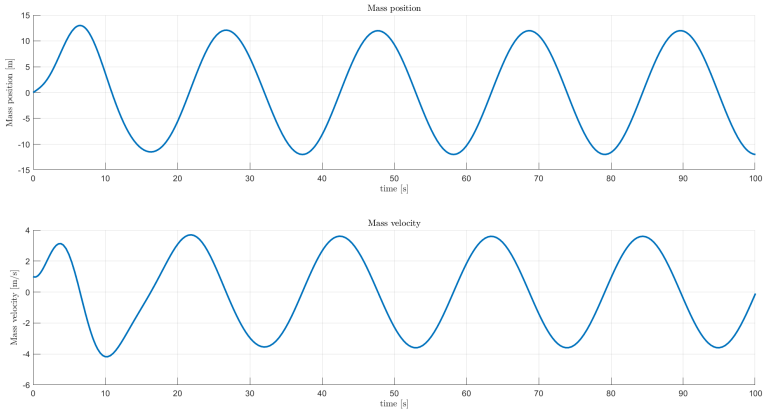

Figure 5.2: Mass position and velocity over time

A, the frequency ω, and the phase φ. A discrete-time estimation approach as defined in chapter 4 can be carried out by introducing a state vector $\mathbf{x}(t)$ which includes the states of the system involved in its dynamics as well as the quantities of interest mentioned above as follows:

$$\mathbf{x}(t) = \begin{Bmatrix} x(t) \\ v(t) \\ A \\ \omega \\ \varphi \end{Bmatrix} \tag{5.6}$$

where $v(t) = \dot{x}(t)$ is the mass velocity, while A, ω and φ are assumed to be constant.

The estimator will then produce an estimate $\hat{\mathbf{x}}(t)$ at each time step based on knowledge of the system dynamic model and the information provided by the sensor. Despite the system linearity, the estimation technique to be used must be nonlinear owing to the presence of nonlinearities introduced by the exogenous input. In particular, this is due to the fact that the state $\mathbf{x}(t)$ to be estimated encompasses some quantities which are related to the nonlinear disturbance. The state dynamics as defined in equation (5.1) can then be represented in the following form:

$$\dot{\mathbf{x}}(t) = \mathbf{f}(\mathbf{x}, t) = \begin{Bmatrix} v(t) \\ -\frac{k}{m}x(t) - \frac{c}{m}v(t) + \frac{A}{m}\sin(\omega t + \varphi) \\ 0 \\ 0 \\ 0 \end{Bmatrix} \tag{5.7}$$

Before proceeding with the actual estimation implementation, the observability of the system with the available measurement shall be computed in order to make sure that data delivered by sensors are sufficient to retrieve entire information of the quantities of interest. As described in section 3.1.1, the observability check for linear systems can be performed by computing the rank of the observability matrix $\mathcal{O}$: if its rank is equal to the number of the state variables n, then the system is observable, and thus the current state can be estimated using only the information from outputs $\mathbf{y}(\mathbf{x})$. If the global system is nonlinear, a similar approach can be used to check local observability, where $\mathcal{O}$ is computed by means of Lie derivatives, which give a representation of all the information that can be inferred from the outputs over time [17].

To construct the observability matrix $\mathcal{O}$, Lie derivatives up to the $(n-1)$-th order shall be computed. For this specific application, the Lie derivatives of order zero and of higher order k are defined as:

$$\mathcal{L}_{\mathbf{f}}^{0} = \mathbf{y}(\mathbf{x}) \tag{5.8}$$

$$\mathcal{L}_{\mathbf{f}}^{k} = \frac{d^k}{dt^k}\mathbf{y}(\mathbf{x}) = \frac{\partial \mathcal{L}_{\mathbf{f}}^{k-1}}{\partial \mathbf{x}}\mathbf{f}(\mathbf{x}) \tag{5.9}$$

Accordingly, the Lie derivative of order zero associated to the one-dimensional system at hand in case of perfect measurement with no additional noise is computed as:

$$\mathcal{L}_{\mathbf{f}}^{0} = y(\mathbf{x}) = v(t) \tag{5.10}$$

while the first order Lie derivative is obtained as shown in the following expression:

$$\begin{aligned}\mathcal{L}_{\mathbf{f}}^{1} = \dot{y}(\mathbf{x}) = \frac{dy(\mathbf{x})}{dt} = \frac{\partial \mathcal{L}_{\mathbf{f}}^{0}}{\partial \mathbf{x}}\mathbf{f}(\mathbf{x}) = \begin{bmatrix}\frac{\partial v}{\partial x} & \frac{\partial v}{\partial v} & \frac{\partial v}{\partial A} & \frac{\partial v}{\partial \omega} & \frac{\partial v}{\partial \varphi}\end{bmatrix}\mathbf{f}(\mathbf{x}) \\ = \begin{bmatrix}0 & 1 & 0 & 0 & 0\end{bmatrix}\mathbf{f}(\mathbf{x}) = -\frac{k}{m}x(t) - \frac{c}{m}v(t) + \frac{A}{m}\sin(\omega t + \varphi)\end{aligned} \tag{5.11}$$

Analogously, the Lie derivatives up to the 4-th order are computed and gathered into a single vector $\boldsymbol{\phi}$ as follows:

$$\boldsymbol{\phi} = \begin{bmatrix}\boldsymbol{\phi}_1 \\ \boldsymbol{\phi}_2 \\ \boldsymbol{\phi}_3 \\ \boldsymbol{\phi}_4 \\ \boldsymbol{\phi}_5\end{bmatrix} = \begin{bmatrix}\mathcal{L}_{\mathbf{f}}^{0} \\ \mathcal{L}_{\mathbf{f}}^{1} \\ \mathcal{L}_{\mathbf{f}}^{2} \\ \mathcal{L}_{\mathbf{f}}^{3} \\ \mathcal{L}_{\mathbf{f}}^{4}\end{bmatrix} = \begin{bmatrix}y(\mathbf{x}) \\ \frac{\partial \mathcal{L}_{\mathbf{f}}^{0}}{\partial \mathbf{x}}\mathbf{f}(\mathbf{x}) \\ \frac{\partial \mathcal{L}_{\mathbf{f}}^{1}}{\partial \mathbf{x}}\mathbf{f}(\mathbf{x}) \\ \frac{\partial \mathcal{L}_{\mathbf{f}}^{2}}{\partial \mathbf{x}}\mathbf{f}(\mathbf{x}) \\ \frac{\partial \mathcal{L}_{\mathbf{f}}^{3}}{\partial \mathbf{x}}\mathbf{f}(\mathbf{x})\end{bmatrix}$$

$$= \begin{bmatrix} v(t) \\ -\frac{k}{m}x(t) - \frac{c}{m}v(t) + \frac{A}{m}\sin(\omega t + \varphi) \\ -\frac{k}{m}v(t) - \frac{c}{m}\left[-\frac{k}{m}x(t) - \frac{c}{m}v(t) + \frac{A}{m}\sin(\omega t + \varphi)\right] \\ \frac{ck}{m^2}v(t) + \left(-\frac{k}{m} + \frac{c^2}{m^2}\right)\left[-\frac{k}{m}x(t) - \frac{c}{m}v(t) + \frac{A}{m}\sin(\omega t + \varphi)\right] \\ -\frac{k}{m}\left(-\frac{k}{m} + \frac{c^2}{m^2}\right)v(t) + \left[\frac{ck}{m^2} - \frac{c}{m}\left(-\frac{k}{m} + \frac{c^2}{m^2}\right)\right]\left[-\frac{k}{m}x(t) - \frac{c}{m}v(t) + \frac{A}{m}\sin(\omega t + \varphi)\right] \end{bmatrix} \tag{5.12}$$

The observability matrix in the nonlinear case is then obtained as the jacobian of $\boldsymbol{\phi}$ with respect to the state vector $\mathbf{x}(t)$:

$$\mathcal{O} = \frac{\partial \boldsymbol{\phi}}{\partial \mathbf{x}} = \begin{bmatrix}\frac{\partial \boldsymbol{\phi}_1}{\partial x} & \frac{\partial \boldsymbol{\phi}_1}{\partial v} & \frac{\partial \boldsymbol{\phi}_1}{\partial A} & \frac{\partial \boldsymbol{\phi}_1}{\partial \omega} & \frac{\partial \boldsymbol{\phi}_1}{\partial \varphi} \\ \frac{\partial \boldsymbol{\phi}_2}{\partial x} & \frac{\partial \boldsymbol{\phi}_2}{\partial v} & \frac{\partial \boldsymbol{\phi}_2}{\partial A} & \frac{\partial \boldsymbol{\phi}_2}{\partial \omega} & \frac{\partial \boldsymbol{\phi}_2}{\partial \varphi} \\ \frac{\partial \boldsymbol{\phi}_3}{\partial x} & \frac{\partial \boldsymbol{\phi}_3}{\partial v} & \frac{\partial \boldsymbol{\phi}_3}{\partial A} & \frac{\partial \boldsymbol{\phi}_3}{\partial \omega} & \frac{\partial \boldsymbol{\phi}_3}{\partial \varphi} \\ \frac{\partial \boldsymbol{\phi}_4}{\partial x} & \frac{\partial \boldsymbol{\phi}_4}{\partial v} & \frac{\partial \boldsymbol{\phi}_4}{\partial A} & \frac{\partial \boldsymbol{\phi}_4}{\partial \omega} & \frac{\partial \boldsymbol{\phi}_4}{\partial \varphi} \\ \frac{\partial \boldsymbol{\phi}_5}{\partial x} & \frac{\partial \boldsymbol{\phi}_5}{\partial v} & \frac{\partial \boldsymbol{\phi}_5}{\partial A} & \frac{\partial \boldsymbol{\phi}_5}{\partial \omega} & \frac{\partial \boldsymbol{\phi}_5}{\partial \varphi}\end{bmatrix} =$$

$$= \begin{bmatrix} 0 & 1 & 0 & 0 & 0 \\ -\frac{k}{m} & -\frac{c}{m} & \frac{1}{m}\sin(\omega t + \varphi) & \frac{At}{m}\cos(\omega t + \varphi) & \frac{A}{m}\cos(\omega t + \varphi) \\ \frac{ck}{m^2} & -\frac{k}{m} + \frac{c^2}{m^2} & -\frac{c}{m^2}\sin(\omega t + \varphi) & -\frac{Act}{m^2}\cos(\omega t + \varphi) & -\frac{Ac}{m^2}\cos(\omega t + \varphi) \\ -\alpha\frac{k}{m} & \frac{ck}{m^2} - \alpha\frac{c}{m} & \frac{\alpha}{m}\sin(\omega t + \varphi) & \frac{At\alpha}{m}\cos(\omega t + \varphi) & \frac{A\alpha}{m}\cos(\omega t + \varphi) \\ -\beta\frac{k}{m} & -\alpha\frac{k}{m} - \beta\frac{c}{m} & \frac{\beta}{m}\sin(\omega t + \varphi) & \frac{At\beta}{m}\cos(\omega t + \varphi) & \frac{A\beta}{m}\cos(\omega t + \varphi) \end{bmatrix} \tag{5.13}$$

where $\alpha = -\frac{k}{m} + \frac{c^2}{m^2}$ and $\beta = \frac{ck}{m} - \alpha\frac{c}{m}$.

It is easy to verify that the fourth column is equal to the last one multiplied by t, which means that the two columns are linearly dependent and that the rank of the matrix will never be full for any value of the variables. A more detailed computation reveals that the observability matrix has $\text{rank}(\mathcal{O}) = 2 \neq n = 5$, for any value of m, c, k, ω, A, φ, and t different from zero. This conclusion means that the system is not fully observable and that the data provided by the velocity sensor are not sufficient to infer complete information of the state variables over time. By integrating the system with an additional sensor measuring the mass position $x(t)$, this result changes only slightly – the rank of $\mathcal{O}$ becomes 3 – but it still remains different from the total number of the variables in the state. This outcome is particularly relevant, since it emphasises the impossibility to produce an estimate of the exogenous disturbance over time by directly evaluating the parameters that characterise the disturbance itself. Moreover, this result has been derived for the most elementary system with only one degree of freedom, which is excited by an input force modeled as a simple harmonic. It is natural to presume that the same behaviour would then occur for more complex systems as well.

Therefore a different approach shall be introduced to overcome this issue. In the following, an estimator made up of two different parts will be used, as shown in Figure 5.3. In particular, the first part of the overall estimator will be system-based, whereas the second one will be input-based. Several benefits are obtained by using the structure of this last approach. Since it is only based on the system, the first part of the estimator will be constructed in order to be a linear filter. In fact, as already mentioned, the nonlinearity of the system is contained only in the disturbance input. This brings a great advantage, as all the mathematical formulations developed in a linear framework (which are, in general, easier than the nonlinear case and more mature) can be exploited. For instance, the linear $\mathcal{H}_\infty$ theory to construct a robust estimator can now be used. The purpose of this part of the estimator will then be the generation of an estimate $\hat{d}(t)$ of the input disturbance $d(t)$ over time, by considering only the system dynamics and from the information deriving from the sensors.

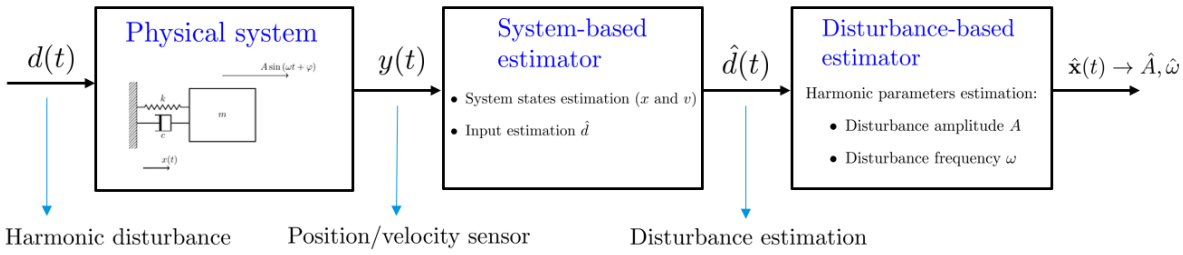

Figure 5.3: Block representation of the estimator made up of two components in series

As regards the second part of the filter, it only relies on the structure of the input. A simple Fast Fourier Transform (FFT) can be used to capture the spectral content of the disturbance. Alternatively, a nonlinear estimation technique can be implemented by introducing a new state with less variables, as the physical states of the system – i.e. $x(t)$ and $v(t)$ – are now already embedded in the first part of the estimator and because the filter is only input-dependent. Furthermore, no robustness requirements shall be satisfied in this segment, whose objective is to produce estimates of the input amplitude $\hat{A}$ and frequency $\hat{\omega}$.

5.3 Robust $\mathcal{H}_\infty$ estimation

The objective of the first part of the estimator is to produce a robust estimate of the input disturbance from knowledge of the system dynamics and the information provided by sensors. Since the system at hand is linear, the linear $\mathcal{H}_\infty$ theory described in chapter 3 can be applied. Figure 5.4 shows the block diagram representing the role of each subsystem and the interaction of the variables involved in the estimation process. In particular, the mass-spring-damper system dynamics is defined in the nominal plant block with transfer function $P(s)$ to be determined, and the disturbance input $d(t)$ acting on the structure contributes to generate the output variable $y_P(t) = v(t)$ which is a measure of the mass velocity provided by the sensor. Such quantity is corrupted by the sensor noise $n(t)$ and is used as the input information of the $\mathcal{H}_\infty$ filter with transfer function $F(s)$ to produce an estimate $\hat{d}(t)$ of the disturbance $d(t)$. This estimate is then compared to the real input variable to compute an estimation error $e(t)$ which corresponds to the performance variable to be minimised.

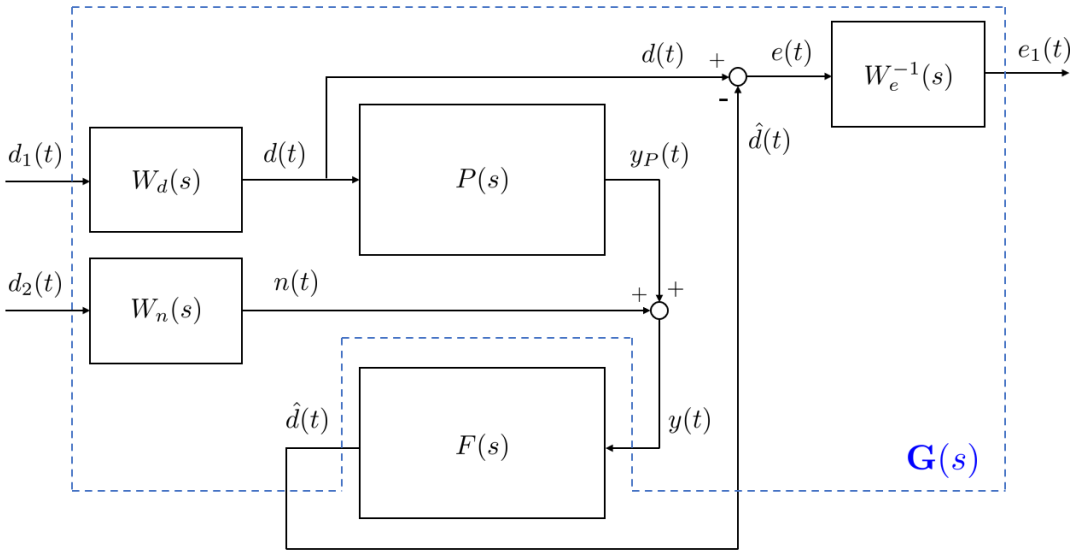

Figure 5.4: One-dimensional system block diagram

The main purpose of this section is then the synthesis of a robust estimator $F(s)$ using the $\mathcal{H}_\infty$ theory, which minimises the worst-case gain of the closed-loop system with the exogenous variables $d(t)$ and $n(t)$ as input and the performance parameter $e(t)$ as the output in the $\mathcal{H}_\infty$ norm sense. In addition, the weighting functions $W_d(s)$, $W_n(s)$, and $W_e^{-1}(s)$ are introduced to this purpose. They allow to perform the analysis with normalised quantities $d_1(t)$, $d_2(t)$ and $e_1(t)$ while producing a modulation of the input and output variables both in amplitude and in frequency. The weighting functions W_d and W_n are designed from the available information of the input quantities, while the weighting function $W_e^{-1}(s)$ is usually computed by means of an iterative process to obtain the optimal minimising solution.

Nominal plant

By defining a new state vector $\mathbf{x}_P(t)$ with respect to the linear one-dimensional system at hand as:

$$\mathbf{x}_P(t) = \begin{Bmatrix} x(t) \\ v(t) \end{Bmatrix} \tag{5.14}$$

it is possible to describe the plant and the output dynamics described by equations (5.1) and (5.2) in a state-space representation as follows:

$$\begin{gathered} \dot{\mathbf{x}}_P(t) = \begin{Bmatrix} \dot{x}(t) \\ \dot{v}(t) \end{Bmatrix} = \begin{bmatrix} 0 & 1 \\ -\frac{k}{m} & -\frac{c}{m} \end{bmatrix} \mathbf{x}_P(t) + \begin{bmatrix} 0 \\ \frac{1}{m} \end{bmatrix} d(t) \\ y_P(t) = \begin{bmatrix} 0 & 1 \end{bmatrix} \mathbf{x}_P(t) \end{gathered} \tag{5.15}$$

or, in a more compact form:

$$\begin{aligned} \dot{\mathbf{x}}_P(t) &= \mathbf{A}_P \mathbf{x}_P(t) + \mathbf{B}_P d(t) \\ y_P(t) &= \mathbf{C}_P \mathbf{x}_P(t) \end{aligned} \tag{5.16}$$

where temporarily no additional noise from the sensor has been taken into account. The plant transfer function $P(s)$ can be computed as follows:

$$P(s) = \left[\begin{array}{c|c} \mathbf{A}_P & \mathbf{B}_P \\ \hline \mathbf{C}_P & \mathbf{0} \end{array}\right] = \mathbf{C}_P(s\mathbf{I} - \mathbf{A}_P)^{-1}\mathbf{B}_P = \frac{s}{ms^2 + cs + k} \tag{5.17}$$

Weighting functions

The weighting functions referring to exogenous inputs are usually constructed from the available information of such variables in terms of their frequency content, for instance from data obtained by the related Power Spectral Density (PSD) or from aprioristic knowledge or prediction of the process. On the other hand, the weighting functions regarding the performance quantities can be designed in order to introduce a penalty in a specific frequency range, which in turn produces more relevance in the disturbance estimation during the $\mathcal{H}_\infty$ filter design within the selected interval. Therefore, they play a crucial role during the design process and the final form of the estimator $F(s)$ will be highly dependent on the adopted estimation strategy embedded in the weighting functions.

The weighting functions are physically circuits or devices simulating a desired dynamic process that can be represented in a state-space form or as transfer functions. In the latter case, a common design approach consists in modelling the dynamics as signal processing filters which remove certain frequencies and allow other to pass according to the input frequency content or the output desirable performance. A relevant example is the Butterworth filter, which is a type of signal processing filter designed to have a frequency response as flat as possible in the pass-band. As any other filter, in the case of a low-pass filter it is characterised by a cut-off frequency ω_c from which the input of the filter begins to be attenuated, and a roll-off rate which represents the steepness of attenuation of the higher frequencies. In particular, the low-pass Butterworth filter transfer function is defined as follows:

$$H(s) = \frac{G_0}{B_n(\tilde{s})} \tag{5.18}$$

where G_0 is the DC gain or static gain, i.e. the value of the transfer function at low frequency, while $B_n(\tilde{s})$ is the normalised Butterworth polynomial of order n evaluated at frequency $\tilde{s} = s/\omega_c$.

The Butterworth normalised polynomial of order n are defined as follows [33]:

$$B_n(\tilde{s}) = \prod_{k=1}^{n/2}\left[\tilde{s}^2 - 2\tilde{s}\cos\left(\frac{2k+n-1}{2n}\pi\right) + 1\right] \quad \text{for } n = \text{even} \tag{5.19}$$

$$B_n(\tilde{s}) = (\tilde{s}+1)\prod_{k=1}^{(n-1)/2}\left[\tilde{s}^2 - 2\tilde{s}\cos\left(\frac{2k+n-1}{2n}\pi\right) + 1\right] \quad \text{for } n = \text{odd} \tag{5.20}$$

Table 5.2 lists the normalised Butterworth polyinomials up to order 6 approximated to four decimal places.

Order n	$B_n(\tilde{s})$
1	$\tilde{s}+1$
2	$\tilde{s}^2 + 1.4142\tilde{s} + 1$
3	$(\tilde{s}+1)(\tilde{s}^2+\tilde{s}+1)$
4	$(\tilde{s}^2 + 0.7654\tilde{s} + 1)(\tilde{s}^2 + 1.8478\tilde{s} + 1)$
5	$(\tilde{s}+1)(\tilde{s}^2 + 0.6180\tilde{s} + 1)(\tilde{s}^2 + 1.6180\tilde{s} + 1)$
6	$(\tilde{s}^2 + 0.5176\tilde{s} + 1)(\tilde{s}^2 + 1.4142\tilde{s} + 1)(\tilde{s}^2 + 1.9319\tilde{s} + 1)$

Table 5.2: Butterworth polynomials up to order 6

The other types of Butterworth filters, such as the high-pass filter, the band-pass filter and the stop-band filter can be obtained by modifying the basic low-pass Butterworth filter.

Noise weighting function W_n

The characteristics of the sensor noise are shown in table 5.1, which contains the predicted amplitude of the signal and its frequency range of action. Since no detailed information is available, the weighting function $W_n(s)$ can be modeled as a high-pass filter with cut-off frequency ω_c equal to the smallest accessible value of the noise frequency and a constant pass-band with amplitude equal to the theoretical value of 10^{-2} m/s as listed in table 5.1. The Butterworth filter is chosen to be of second order, with a roll-off rate of 40 dB/decade. As no stringent requirements at low frequency are present because of the confidence in the information $\omega_c \gg 100$ rad/s, the static gain G_0 is selected so that the frequencies lower than the cut-off frequency are attenuated of only 20 dB with respect to the pass-band.

Furthermore, from the requirements listed above, the transfer function of weighting function $W_n(s)$ relative to the sensor noise needs to be constructed such that it contains two poles at cut-off frequency $\omega_c = 100$ and two zeros at frequency $10\sqrt{10}$. By using the Butterworth polynomials of order $n = 2$, the transfer function can then be computed as:

$$W_n(s) = 10^{-3}\frac{\frac{s^2}{(10\sqrt{10})^2} + 1.4142\frac{s}{10\sqrt{10}} + 1}{\frac{s^2}{100^2} + 1.4142\frac{s}{100} + 1} = \frac{10^{-5}s^2 + 0.0004472s + 0.01}{0.001s^2 + 0.14142s + 10} \tag{5.21}$$

In addition, the Bode magnitude plot for the transfer function W_n is shown in Figure 5.5.

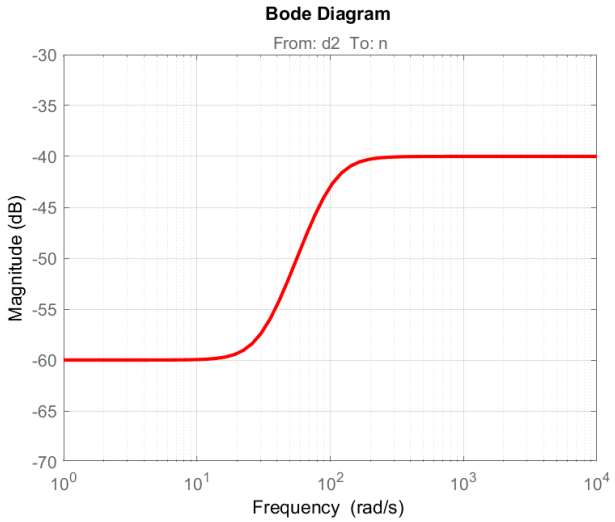

Figure 5.5: Bode magnitude plot of the noise weighting function W_n

Disturbance weighting function W_d

The disturbance weighting function is modelled as a Butterworth band-pass filter, whose bandwidth and amplitude are defined by the aprioristic knowledge of the disturbance process as listed in table 5.1. If there is great confidence that the maximum amplitude of the exogenous input is 10 N and the spectral components are included in the frequency range 0.1-1 rad/s, a 5th order band-pass Butterworth filter can be constructed so that the transfer function has a Bode magnitude plot as shown in Figure 5.6, with 5 zeros on the origin, 5 poles at frequency $\omega_1 = 0.1$ rad/s, 5 other poles at frequency $\omega_2 = 1$ rad/s and a null DC gain to attenuate as much as possible all the frequencies out of the bandwidth.

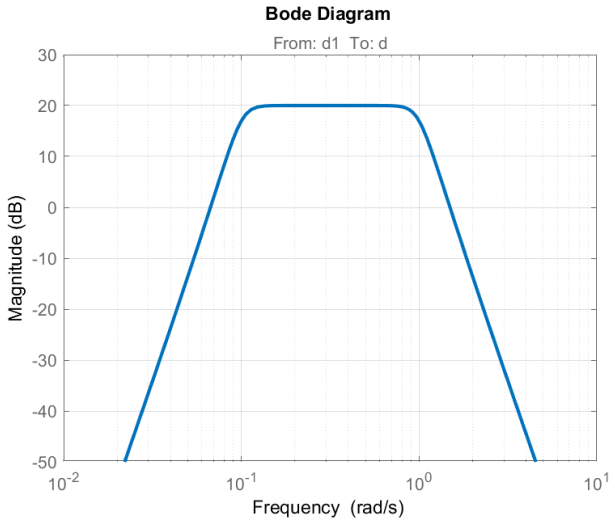

Figure 5.6: Bode magnitude plot of the disturbance weighting function W_d

Performance weighting function W_e

The performance weighting function can be designed by considering its inverse transfer function $W_e^{-1}(s)$. The task of $W_e^{-1}(s)$ is to add a penalty term at specific frequency ranges of interest. In this particular case, since the objective of the estimator is the eval-

uation of the input disturbance $d(t)$ whose frequency content is assumed to be known, the transfer function $W_e^{-1}(s)$ is modeled as a band-pass filter with a bandwidth which contains the presumed frequencies of $d(t)$. Out of the pass-band, the input of $W_e^{-1}(s)$ will neither be amplified nor attenuated as there is no interest in the estimation at such frequencies, which means that the static gain and the gain at high frequency will be 0 dB. As regards the amplitude of the pass-band for a suboptimal $\mathcal{H}_\infty$ estimator, it is usually computed by means of an iterative process in order to obtain the maximum possible magnitude, while guaranteeing that the worst-case gain of the closed-loop function will always be satisfied. In the case of normalised inputs and outputs this entails that the parameter γ introduced in equation (3.120) is less than one. The weighting function $W_e^{-1}(s)$ which produces a value $\gamma = 0.9999$ is depicted in Figure 5.7.

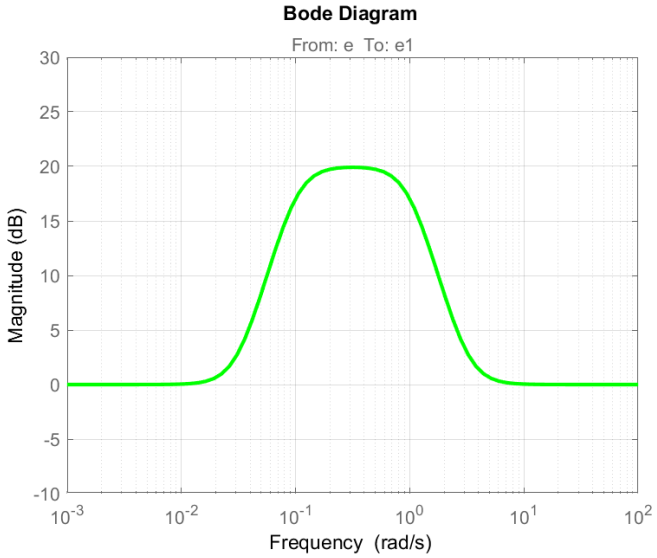

Figure 5.7: Bode magnitude plot of the inverse performance weighting function W_e^{-1}

Global system

With reference to the block diagram in Figure 5.4, the only transfer function to be determined is now the $\mathcal{H}_\infty$ estimator. The approach described in section 3.6 for the synthesis of $F(s)$ can be carried out. The system shall then be represented in an LFT form by introducing the vector $\mathbf{w}(t)$ encompassing the normalised exogenous variables as follows:

$$\mathbf{w}(t) = \begin{Bmatrix} d_1(t) \\ d_2(t) \end{Bmatrix} \tag{5.22}$$

In addition, the outputs of the plant $\mathbf{G}(s)$ described in an LFT framework are the normalised performance variable $e_1(t)$ and the noisy measurement $y(t) = y_P(t) + n(t)$ provided by the velocity sensor. A third input of the system $\mathbf{G}(s)$ is the estimation of the disturbance $\hat{d}(t)$ generated by the estimator $F(s)$. The two outputs shall now be related to the three inputs to construct the system transfer function $\mathbf{G}(s)$. In particular, as shown from the block diagram in Figure 5.4, the normalised estimation error $e_1(t)$ in the Laplace domain can be related to the input parameters as follows:

$$e_1(s) = W_e^{-1} e = W_e^{-1}(d - \hat{d}) = W_e^{-1} W_d d_1 - W_e^{-1}\hat{d} \tag{5.23}$$

Similarly, the noisy output generated by the velocity sensor can be written in the Laplace domain as:

$$y(s) = y_P + n = Pd + W_n d_2 = PW_d d_1 + W_n d_2 \tag{5.24}$$

The system transfer function $\mathbf{G}(s)$ can finally be expressed in the LFT form as follows:

$$\begin{aligned} \begin{Bmatrix} e_1 \\ y \end{Bmatrix} &= \mathbf{G}(s) \begin{Bmatrix} \mathbf{w} \\ \hat{d} \end{Bmatrix} = \\ &= \left[\begin{array}{c|c} \mathbf{G}_{11} & G_{12} \\ \hline \mathbf{G}_{21} & G_{22} \end{array}\right] \begin{Bmatrix} \mathbf{w} \\ \hat{d} \end{Bmatrix} = \left[\begin{array}{cc|c} W_e^{-1} W_d & 0 & -W_e^{-1} \\ \hline PW_d & W_n & 0 \end{array}\right] \begin{Bmatrix} d_1 \\ d_2 \\ \hat{d} \end{Bmatrix} \end{aligned} \tag{5.25}$$

The block diagram representation in the LFT form is shown in Figure 5.8.

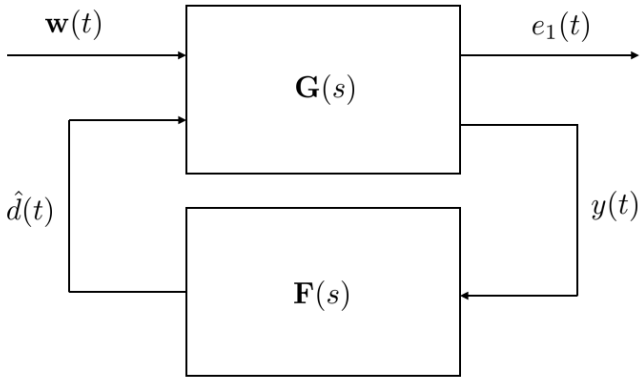

Figure 5.8: One dimensional system LFT block diagram

The closed-loop transfer function $\mathbf{M}(s)$ from the exogenous input vector $\mathbf{w}(t)$ to the normalised performance value $e_1(t)$ can now be obtained as described in section 3.4:

$$\begin{aligned} \mathbf{M}(s) &= \mathcal{F}_l(\mathbf{G}, F) = \mathbf{G}_{11} + G_{12}F(1 - G_{22}F)^{-1}\mathbf{G}_{21} \\ &= \begin{bmatrix} W_e^{-1} W_d & 0 \end{bmatrix} - W_e^{-1} F \begin{bmatrix} PW_d & W_n \end{bmatrix} \\ &= \begin{bmatrix} W_e^{-1} W_d & 0 \end{bmatrix} - \begin{bmatrix} W_e^{-1} FPW_d & W_e^{-1} FW_n \end{bmatrix} \\ &= \begin{bmatrix} W_e^{-1}(1 - FP)W_d & -W_e^{-1} FW_n \end{bmatrix} \end{aligned} \tag{5.26}$$

The normalised estimation error $e_1(t)$ can then be expressed in the Laplace domain as:

$$\begin{aligned} e_1(s) = \mathbf{M}(s) \begin{Bmatrix} d_1(s) \\ d_2(s) \end{Bmatrix} &= \begin{bmatrix} M_1(s) & M_2(s) \end{bmatrix} \begin{Bmatrix} d_1(s) \\ d_2(s) \end{Bmatrix} \\ &= \begin{bmatrix} W_e^{-1}(1 - FP)W_d & -W_e^{-1} FW_n \end{bmatrix} \begin{Bmatrix} d_1(s) \\ d_2(s) \end{Bmatrix} \end{aligned} \tag{5.27}$$

It is interesting to note that the estimator transfer function $F(s)$ shall be designed such that it minimises both $M_1(s)$ and $M_2(s)$ in terms of the $\mathcal{H}_\infty$ norm at the same

time. However, such requirements are in contrast with one another. In particular, to obtain noise rejection and thus minimise $M_2(s)$, the estimator $F(s)$ should have the lowest possible value (zero as the limit value to accomplish complete noise filtering), but on the other hand the estimation error $e(t)$ would show the following behaviour:

$$e_1(s) = W_e^{-1} W_d d_1(s) \;\rightarrow\; e(s) = d(s) \;\rightarrow\; d(s) - \hat{d}(s) = d(s) \tag{5.28}$$

which entails that the estimated value $\hat{d}(t)$ by the filter $F(s)$ will always be null and thus the estimator is not producing any estimate. Likewise, the minimisation of $M_1(s)$ with no additional constraint would generate an estimator $F(s)$ that amplifies the noise $n(t)$. The optimal solution must then take into consideration both $d_1(t)$ and $d_2(t)$ to ensure minimisation of the $\mathcal{H}_\infty$ norm of $\mathbf{M}(s)$ while accounting for the effect produced by both the inputs on the performance variable $e_1(t)$.

In this context, the crucial role played by the weighting functions $W_d(s)$, $W_n(s)$ and $W_e(s)$ is clearly visible. As already mentioned, the design of the transfer function $F(s)$ is highly dependent on the selection of such weighting functions. In this example, the input disturbance $d(t)$ acts on the system only within a specific bandwidth whose frequencies are lower with respect to the ones related to the sensor noise $n(t)$. By selecting the weighting function accordingly and consistently with this information, the filter design is extremely simplified, since it will tend to minimise $M_1(s)$ within the bandwidth specified by $W_d(s)$ and simultaneously minimise $M_2(s)$ at higher frequencies where the noisy components dominate as defined in $W_n(s)$. By means of this distinction over the different frequencies, the design of $F(s)$ will no longer be in contrast with the two minimisation requirements.

Figure 5.9 shows the estimator transfer function $F(s)$ computed using the approach described in section 3.6. It can be observed that at lower frequencies $F(s)$ shows a similar behaviour of the inverse transfer function of the plant $P^{-1}(s)$ to minimise the contribution $(1-FP)$ which appears in $M_1(s)$. In particular, there is a major attenuation at ω_0 corresponding to the resonance frequency of the mass-spring-damper system to limit the effects of such response. On the contrary, starting from the lower limit of ω_n and toward higher frequencies, the estimator $F(s)$ assumes values which tend to zero to attenuate the response produced by the sensor noise. The above observations are then validated by the behaviour of the transfer function $F(s)$ over frequency.

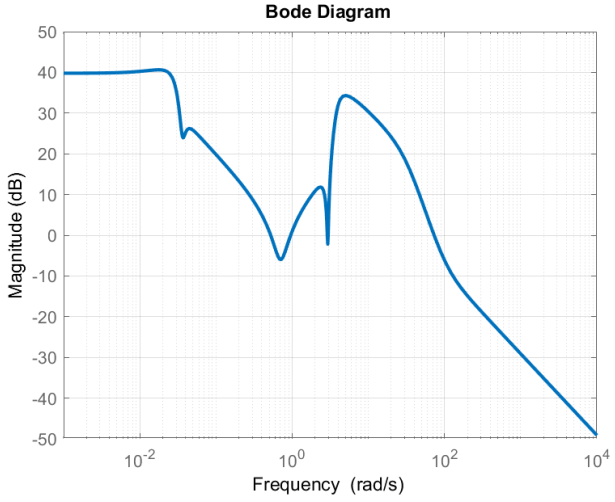

Figure 5.9: Bode magnitude plot of the $\mathcal{H}_\infty$ estimator F

Furthermore, the Bode magnitude plot of the closed-loop transfer function $\mathbf{M}(s)$ depicted in Figure 5.10 shows that as expected the response of the closed-loop system attenuates both the inputs $d_1(t)$ and $d_2(t)$ at any frequency. The highest peak of the overall response is present in the transfer function $M_2(s)$ at low frequency. This is due to the less stringent constraint that is placed in the system by means of the weighting function $W_n(s)$. However, this outcome does not invalidate the design. On the contrary, the design results are validated as the closed-loop transfer function achieves the objective to filter the sensor noise only at high frequency, where the noise components are supposed to lie.

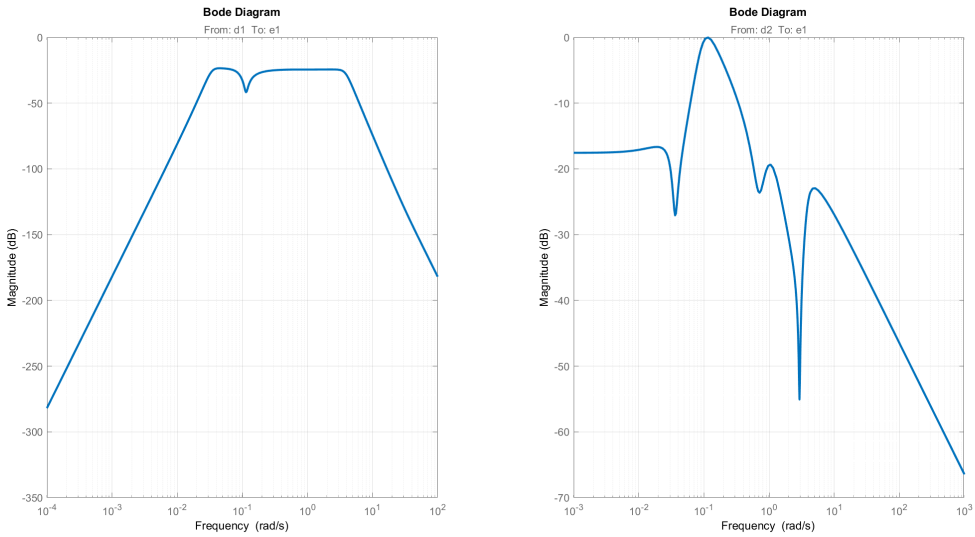

Figure 5.10: Bode magnitude plot of the closed-loop system $\mathbf{M}$

To conclude, from the values of the magnitude of the transfer function $\mathbf{M}(s)$, it is also possible to compute the steady-state estimation accuracy of the developed $\mathcal{H}_\infty$ filter. In particular, the Bode magnitude plot related to the transfer function $M_1(s)$ shows an attenuation of about -25 dB ≈ 0.06 at steady-state within the predicted bandwidth of the input disturbance. Similarly, the weighting function W_e has an attenuation value of about -42 dB ≈ 0.008 within the frequency range 0.1-1 rad/s, while the inverse of the disturbance weighting function $W_d^{-1}(s)$ has a value of -20 dB at steady-state. By neglecting the effect generated by the sensor noise, the steady-state estimation error can then be computed as follows:

$$\begin{aligned} e(j\omega_d) &= W_e(j\omega_d)e_1(j\omega_d) \\ &= W_e(j\omega_d)M_1(j\omega_d)d_1(j\omega_d) \\ &= W_e(j\omega_d)M_1(j\omega_d)W_d^{-1}(j\omega_d)d(j\omega_d) \\ &\approx 0.008 \cdot 0.06 \cdot 0.1 d(j\omega_d) \approx 5 \cdot 10^{-5} d(j\omega_d) \end{aligned} \tag{5.29}$$

which means that:

$$e(j\omega_d) = d(j\omega_d) - \hat{d}(j\omega_d) \approx 5 \cdot 10^{-5} d(j\omega_d) \;\rightarrow\; \hat{d}(j\omega_d) \approx 0.99995 d(j\omega_d) \tag{5.30}$$

The comparison between the disturbance estimation $\hat{d}(t)$ and the actual input $d(t)$ of the system is depicted in Figure 5.11.

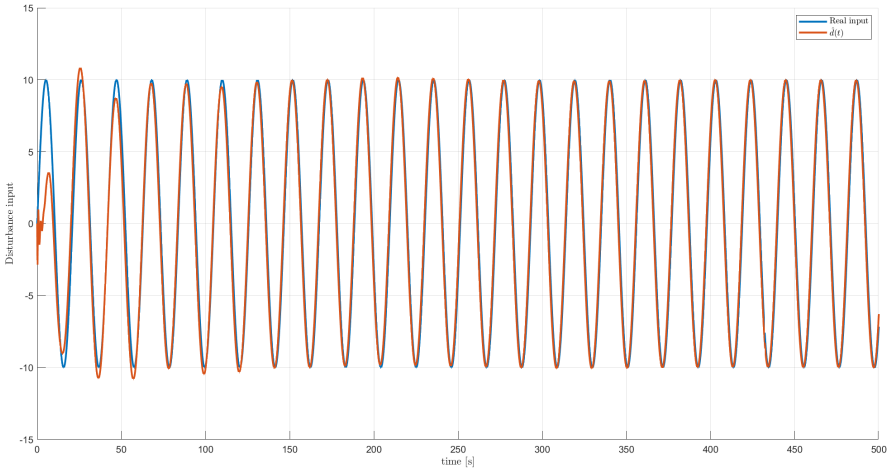

Figure 5.11: Estimated disturbance and actual input signal comparison

Moreover, Figure 5.12 shows a similar comparison where the input disturbance is now the sum of two harmonics with different frequencies included in the bandwidth ω_d. The result validates the estimator $F(s)$, which produces precise estimates of the exogenous input $d(t)$ as long as it is made of harmonic components within the predicted bandwidth.

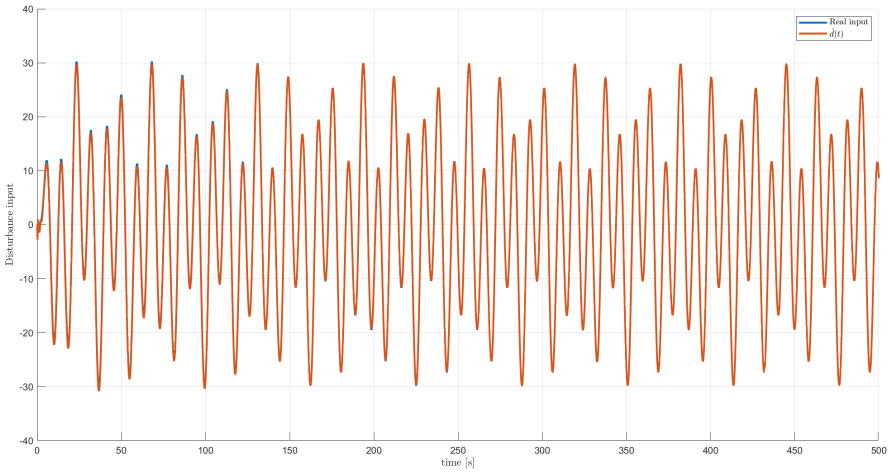

Figure 5.12: Estimated disturbance with input signal generated as the sum of two harmonics

5.4 Disturbance spectral estimation

Once the input disturbance is robustly estimated, two different approaches for the estimation of the amplitude and frequency of the harmonics generating such input signal can be introduced and compared.

The Fast Fourier Transform (FFT) is a method that guarantees rapid evaluation of the quantities of interest and relies on computation of the discrete Fourier transform. It is computationally cheap and does not need any prior information of the input sig-

nal. However, it may suffer from spectral leakage and presents some problems when the frequency of the input is time-dependent. The second approach uses the nonlinear estimation techniques described in chapter 4. In particular the extended Kalman filter is considered, since in this case it achieves the results obtained with the other nonlinear approaches with a similar accuracy and lower computational effort. The EKF requires information about the shape of the input signal. In addition, it shall be correctly initialised to obtain reliable results. Nonetheless, it is able to reconstruct the input disturbance even in the case of amplitude or frequency variations over time.

Due to the distinct features of the two techniques, several signals with different characteristics are considered as input signals for both the FFT and EKF, in order to investigate the behaviour of the two approaches in multiple situations. An accurate comparison is then carried out and their strong and weak points are explored.

5.4.1 Disturbance as a single harmonic

In this section, the comparison between the EKF and the FFT for the estimation of amplitude and frequency of a single harmonic is considered. The input signal is assumed to have a constant amplitude $A = 12$ N and constant frequency $f = 0.3$ Hz (period $T = 10/3$ s), as shown in Figure 5.13.

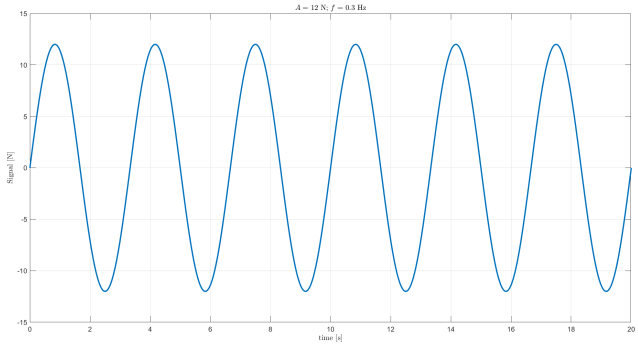

Figure 5.13: Input signal – single harmonic

For amplitude and frequency estimation of the input signal, a fast Fourier transform is carried out with different time windows; the signal is simulated over a time period of 200 s. As shown in Figure 5.14, if the time window is shorter than 10 s, the estimation of both the amplitude and frequency is poor. However, a time window of 10 s is sufficient to get a precise estimate of the two quantities. In particular, the signal spectrum gets narrower as the time window gets larger, and thus when more information is available.

Nonetheless, it can be noted that the signal spectrum that derives from a time window of 12 s gives again poor results. Unlike the other time windows for which $t_{window} \geq 10$ s, the one with value 12 s is the only case whose value is not a multiple of the harmonic period (i.e, $t_{window}/T \neq k$, with $k \in \mathbb{N}$). Therefore, the FFT does not correctly operate over a complete sinusoidal period and a phenomenon called spectral leakage occurs, with a resulting degradation of the spectrum, and thus of the frequency and amplitude estimation.

In the current case, $f = 0.3 \in \mathbb{Q}$; however, whenever this is not the case (e.g. when $f \in \mathbb{R}$ but $f \notin \mathbb{Q}$), the spectral leakage may become a more relevant issue, since it might not be trivial to find a suitable time window to avoid this phenomenon. A solution to

this problem is the use of specific window or tapering functions. However such functions generate in turn a degradation in the amplitude estimation.

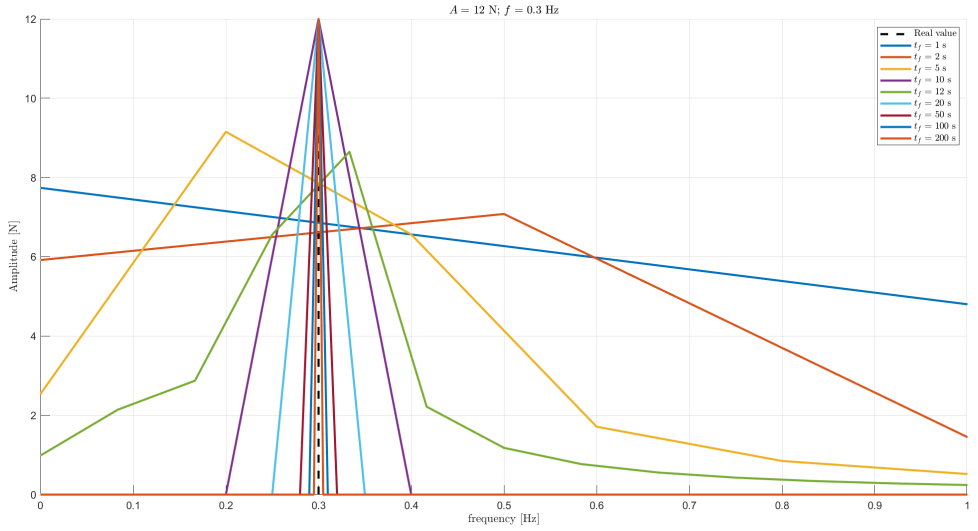

Figure 5.14: FFT estimation – one single harmonic

The main concern regarding the estimation through the EKF is its initialisation. In this case, different values for the initial frequency estimate $\hat{\omega}_0$ have been selected, and they all give good results. By keeping the same value for $\mathbf{P}_0$, the more $\hat{\omega}_0$ is close to the real value, the shorter is the time required for the EKF to reach steady-state, and thus the real frequency. The EKF frequency estimation in the case $\hat{\omega}_0 = 3$ rad/s ($\hat{f}_0 = 3/2\pi \approx 0.4775$ Hz), along with the harmonic amplitude estimation, is shown in Figure 5.15. It is clear that the EKF performs well for the estimation of the two quantities; in addition, the correct value is rapidly retrieved.

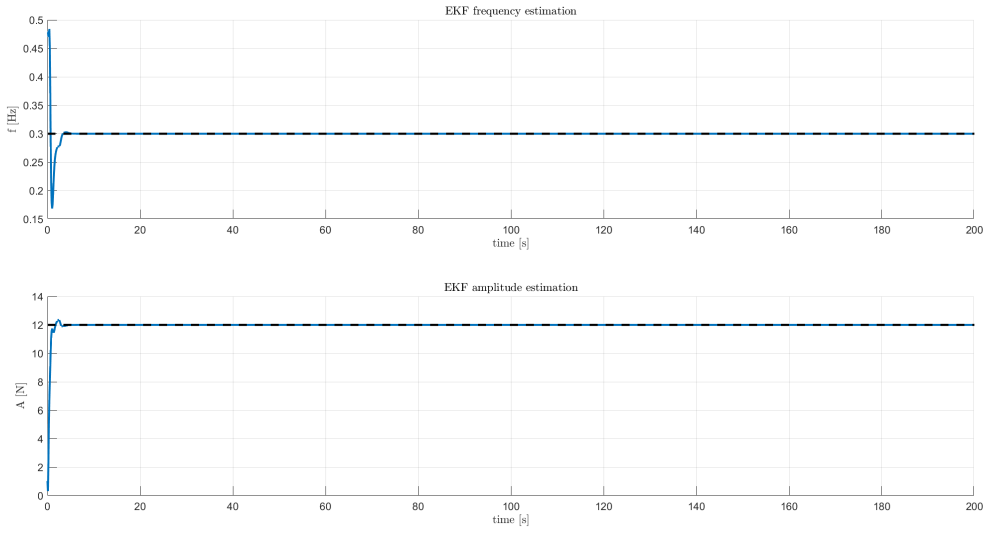

Figure 5.15: EKF estimation – one single harmonic

A comparison of the error between the two filters' estimates for both amplitude and frequency are reported in Figure 5.16. It is visible that for the EKF the estimation is

real-time, whereas the FFT is only considered for specific time intervals. This means that for the FFT estimation, the x-axis represents the length of the time window and not the time evolution of the estimation error as for the EKF. As already pointed out, the estimation error for the FFT is zero for time windows where no spectral leakage arises (e.g., $t_{window} = 10$ s is already a good choice); however, increasing the observation time does not entail better evaluation. Therefore, in this case the EKF performs better, since it reaches the correct values in less time and presents no problems regarding the time window.

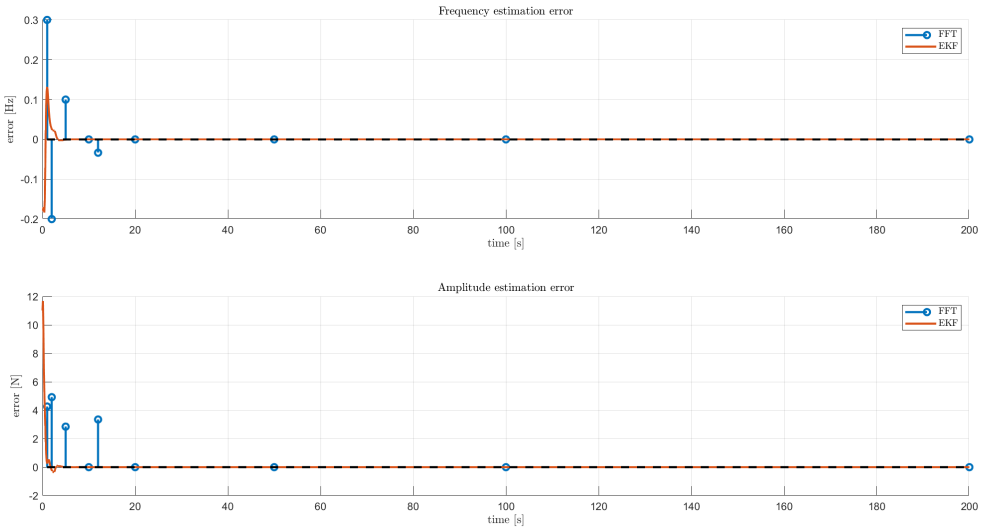

Figure 5.16: FFT and EKF estimation comparison – one single harmonic

5.4.2 Disturbance as the sum of two harmonics

In a general case, any signal can be decomposed as a series of harmonics with different amplitudes and frequencies. Therefore, a relevant example for the investigation of the estimation behaviour of the EKF and the FFT is the case of the sum of more sinusoidal signals. For instance, in this section an input signal generated by the sum of two harmonics with different frequency and amplitude is considered (Figure 5.17). The two frequencies and the two amplitudes of the harmonics are $A_1 = 12$ N, $f_1 = 0.3$ Hz and $A_2 = 8$ N, $f_2 = 0.7$ Hz respectively.

The problem involves now the estimation of four different quantities. In particular, the EKF requires knowledge of the shape of the input signal as well as the number of the harmonics that generate it to perform a correct estimation. Furthermore, the number of state variables becomes larger and the computational effort will increase as well.

As the regards the FFT estimation, the same considerations made in the case of the single harmonic still hold in this situation. The spectral analysis generates two peaks, one for each harmonic of the input signal, with different amplitudes. Similarly to the previous case, for the values of t_{window} considered in Figure 5.18, when the time window is equal or greater than 10 s (with the only exception of $t_{window} = 12$ s, due to spectral leakage) the FFT estimation is able to reconstruct the four quantities of interest with great precision.

Concerning the EKF implementation, when more harmonics are considered, the

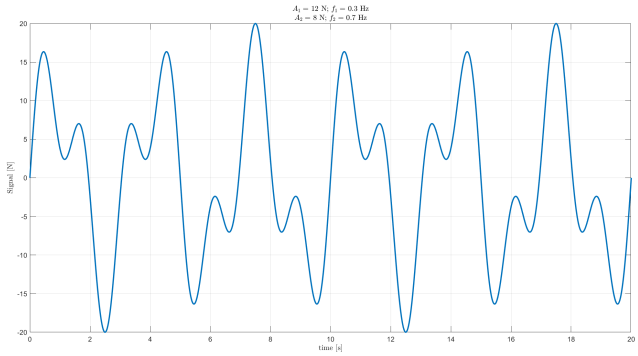

Figure 5.17: Input signal – sum of two harmonics

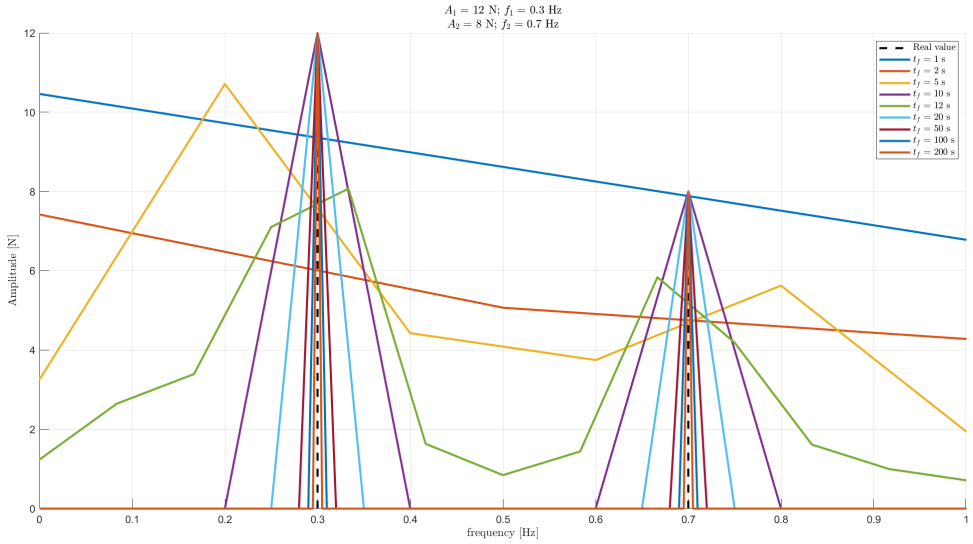

Figure 5.18: FFT estimation – sum of two harmonics

choice of the initial frequency estimates $\hat{\omega}_{0_i}$ are particularly crucial. If $\hat{\omega}_{0_i}$ are selected to be close to both frequencies (for instance by selecting both the initial estimates as the average value of the real frequencies), the estimation over time may oscillate between the values of the two harmonics, with a resulting degradation of the other states' estimation as well. In this simple case, where only two harmonics are considered, it is reasonable to initialize $\hat{\omega}_{0_1}$ and $\hat{\omega}_{0_2}$ such that one has value greater than the highest harmonic, while the second one has a value lower than the smallest one; however, this approach assumes knowledge of the real values for both the frequencies. An alternative is to select a value close to zero for $\hat{\omega}_{0_1}$ and a large value for $\hat{\omega}_{0_2}$.

Figure 5.19 shows the EKF estimation over time for both amplitude and frequency with $\hat{\omega}_{0_1} = 1$ rad/s ($\hat{f}_{0_1} \approx 0.1592$ Hz) and $\hat{\omega}_{0_2} = 5$ rad/s ($\hat{f}_{0_2} \approx 0.7958$ Hz). It is clear that the choice of the initial state vector $\mathbf{x}_0$ results in correct and precise estimation for all the quantities of interest. In addition, very short time to get steady-state values is required.

A comparison of the estimation error generated by the two filters for both amplitude and frequency are reported in Figure 5.20. Once again, both the approaches produce small estimation errors, but present different results depending on the selected time window or on the initialization of the state vector.

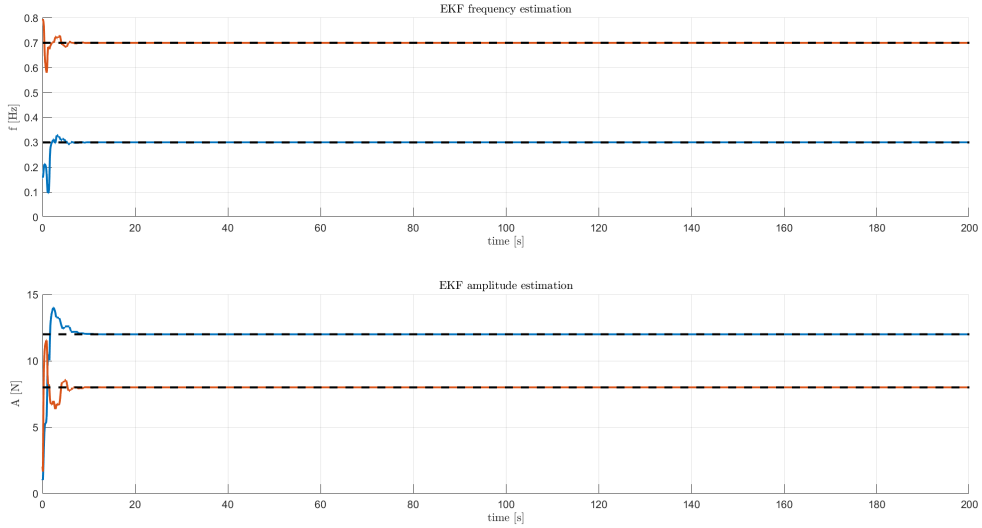

Figure 5.19: EKF estimation – sum of two harmonics

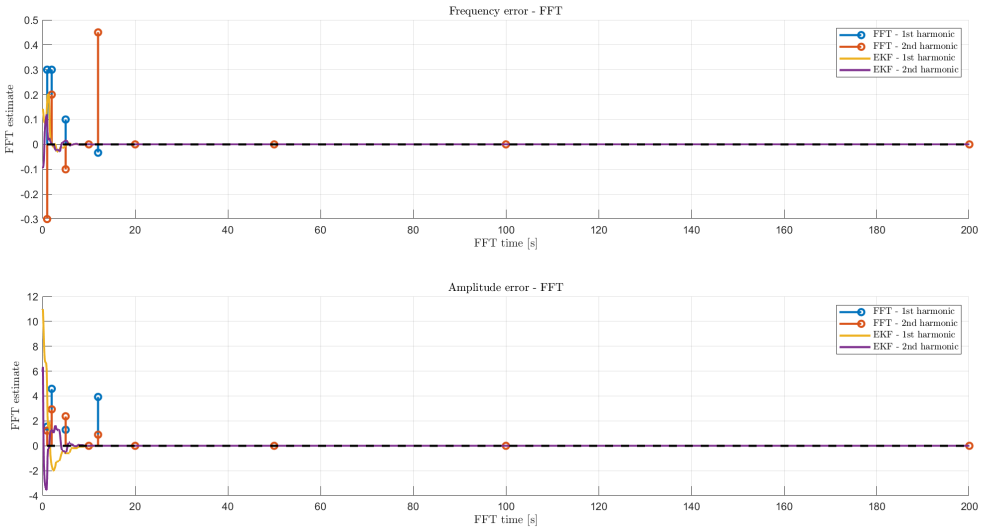

Figure 5.20: FFT and EKF estimation comparison – sum of two harmonics

5.4.3 Disturbance as one harmonic with amplitude varying in time

Another peculiar input condition to be examined is the case of a single harmonic with a linear time-varying amplitude. It is assumed that the amplitude profile over time increases linearly up to 3 times its initial value until it reaches time $t_c = 60$ s, and decreases to its original value at $t_f = 200$ s, as depicted in Figure 5.21. The initial and final value of the amplitude is $A_0 = 12$ N, with a peak of $A_{max} = 36$ N at time t_c: this produces a modulated signal, whose evolution over time is reported in Figure 5.22.

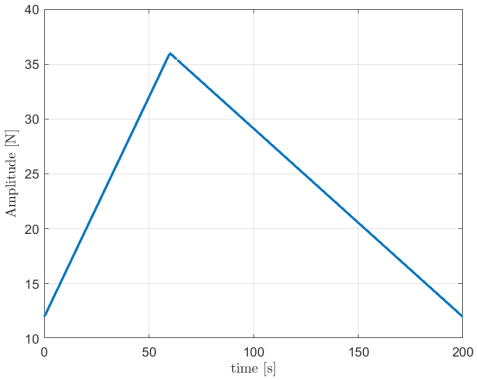

Figure 5.21: Amplitude time evolution

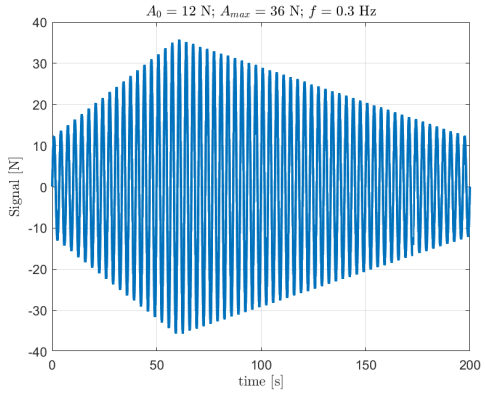

Figure 5.22: Time-varying amplitude harmonic

Because of the form of the signal, the FFT shall be performed different times, since the information contained in each time interval will be different. This leads to the definition of an additional parameter Δt, which represents the time between the beginning of two different time intervals, and thus estimations. A small value of Δt means that several FFT are performed over the entire time in which the simulation is carried out. In addition, it produces a greater computational effort; however, it may be required if the signal has a significantly fast variation over small time intervals. To sum up, amplitude (or frequency, as it will be discussed later) variations in time entail the introduction of additional quantities that shall be carefully selected.

As regards the EKF, the only knowledge of a harmonic input with time-dependent amplitude is not sufficient to compute the time-update equation for the dynamic system which is needed in the algorithm, but the complete shape of the amplitude variation $A(t)$ is required. Nonetheless, in the following the EKF estimation is carried out by assuming that the harmonic has constant amplitude and frequency, similarly to the first case considered in this chapter. Interestingly, it will be shown that the EKF is able to reconstruct the correct behaviour of $A(t)$ as well as the other state variables, despite no information about the time-varying amplitude is included in the algorithm. This has an effect on the estimation error, which will present a degradation with respect to the previous cases, however it makes the EKF a more robust approach that guarantees accurate estimation even in the case in which the input signal behaviour is not perfectly known beforehand.

As previously mentioned, since the amplitude changes in time, the FFT shall be carried out different times in order to capture the harmonic variation. A time interval after which the FFT is performed with respect to the previous estimation shall be selected. In this case, a time interval $\Delta t = t_{window}$ is chosen. Different time windows of 10 s, 12 s, 20 s, and 50 s are considered and shown in Figures from 5.23 to 5.26 respectively.

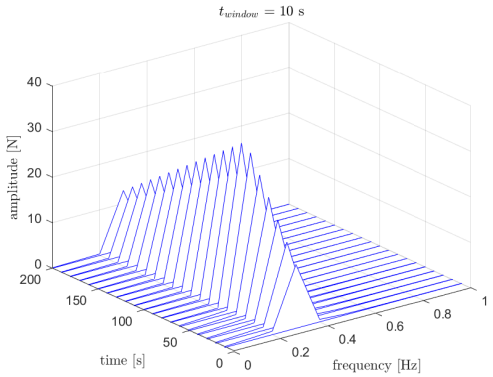

Figure 5.23: FFT estimation with $t_{window} = \Delta t = 10$ s

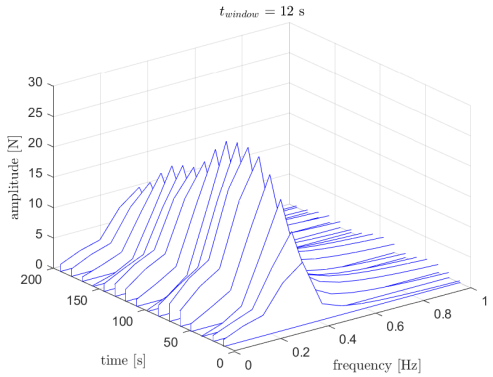

Figure 5.24: FFT estimation with $t_{window} = \Delta t = 12$ s

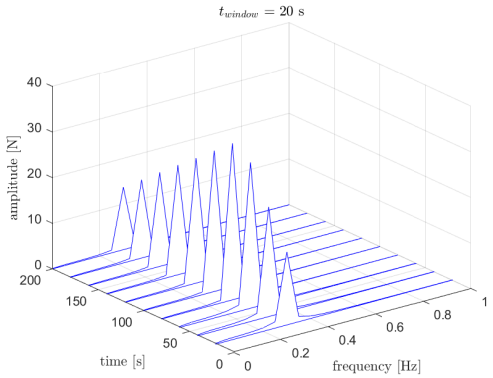

Figure 5.25: FFT estimation with $t_{window} = \Delta t = 20$ s

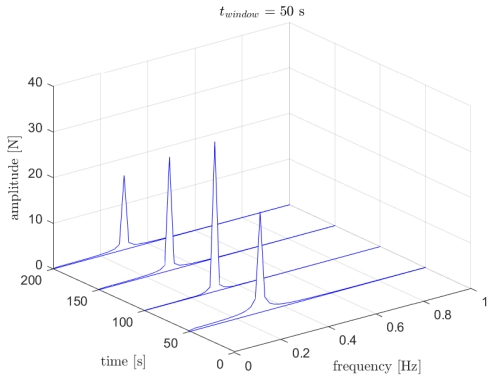

Figure 5.26: FFT estimation with $t_{window} = \Delta t = 50$ s

It can be noted that the amplitude evolution is recovered, and the same problems occurring in the simple case with constant amplitude for $t_{window} = 12$ s are still present, with small contributions at low and high frequency in the amplitude spectrum. Figure 5.27 shows the behaviour of both amplitude and frequency for the different values of t_{window}.

The EKF estimation for amplitude and frequency is shown in Figure 5.28. The filter is initialized using the same values of the case with constant amplitude. From the figure it can be noted that the EKF is able to recover the time variation of the amplitude, even if the algorithm does not include information about its variation and it has been implemented considering the case with constant amplitude.

Figure 5.29 shows the comparison between the estimation error for the FFT and the EKF. The frequency is well estimated with both the approaches and for all the time windows considered, with the only exception of $t_{window} = 12$ s. As regards the amplitude, the EKF performs better than the FFT, for which narrower windows give better results.

5.4.4 Disturbance as one harmonic with frequency varying in time

Similarly to the previous signal, the case of a single harmonic with frequency varying in time is now considered. The initial frequency is $f_0 = 0.3$ Hz, with a linearly decreasing profile up to time $t_c = 60$ s ($f_{min} = 0.03$ Hz), where the frequency increases until it

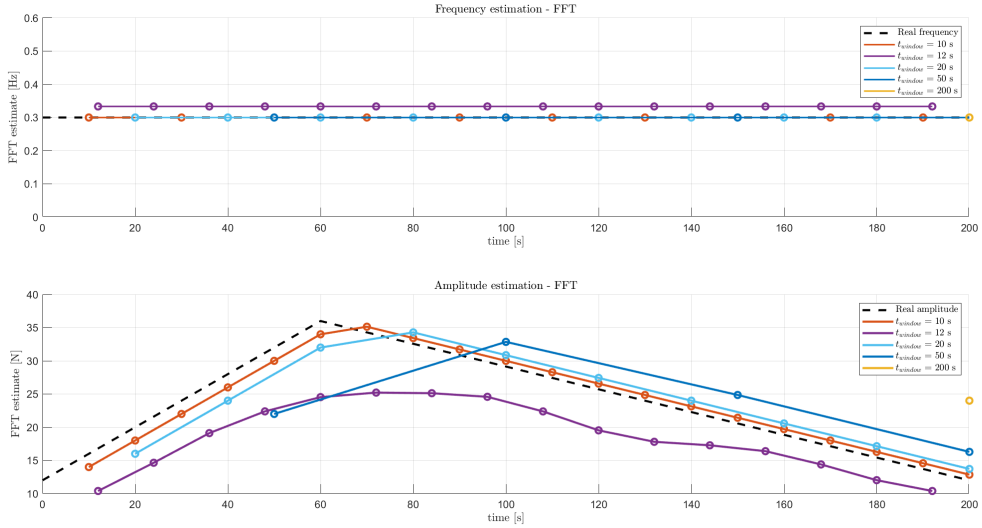

Figure 5.27: FFT estimation – time-varying amplitude

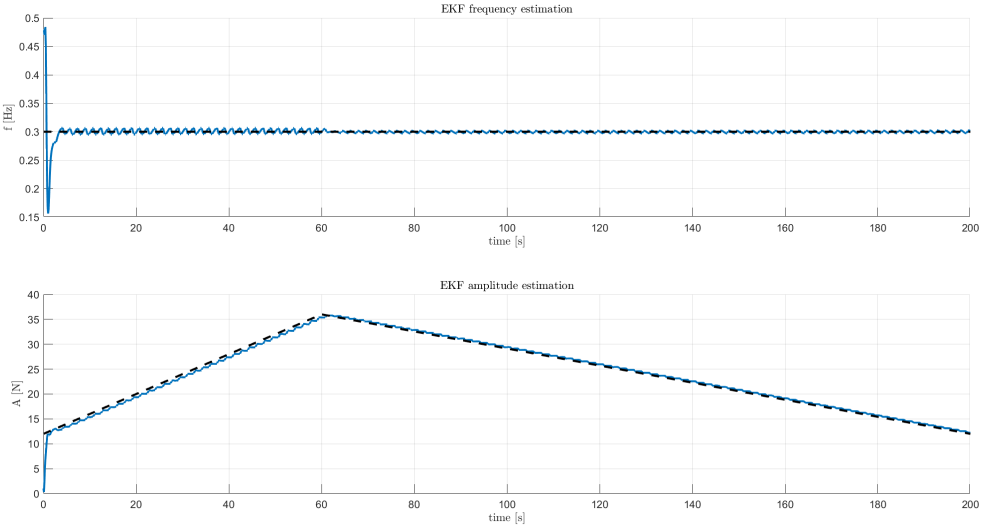

Figure 5.28: EKF estimation – time-varying amplitude

reaches f_0 at t_f. The frequency time evolution is shown in Figure 5.30. The input signal is depicted in Figure 5.31, where the frequency variation in time is clearly visible.

Analogously to the previous case, multiple FFTs shall be carried out after each time interval Δt, since the frequency content of the input signal changes over time. In particular, since the frequency $f(t)$ is now a function of time, it is reasonable to select a small value for Δt. This is due to the mathematical definition of the FFT, that relies on the Fourier transform. The information contained in the time window over which the FFT is performed includes several different frequencies. As a consequence, it may happen that the amplitude spectrum will not generate a unique peak, but more peaks or a flat-like shape encompassing the different frequencies that are present within the same time interval. A possible solution is then the choice of a narrow Δt.

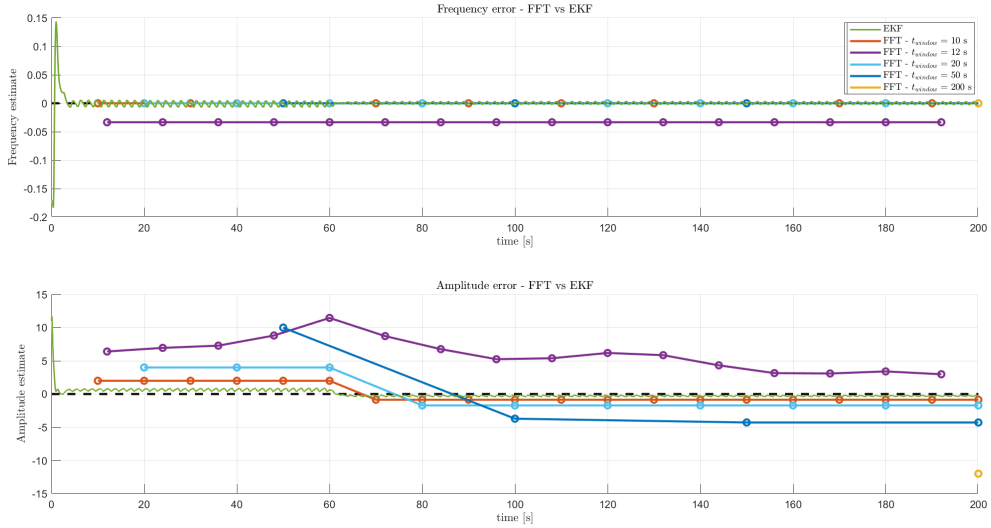

Figure 5.29: FFT and EKF estimation comparison – time-varying amplitude

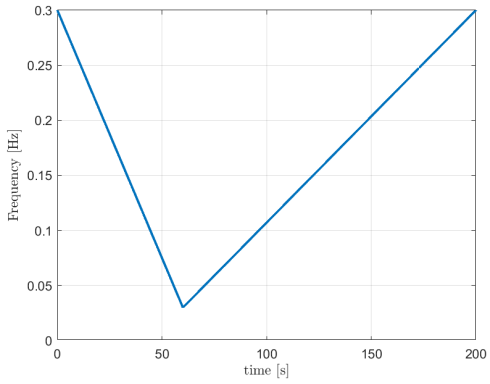

Figure 5.30: Frequency time evolution

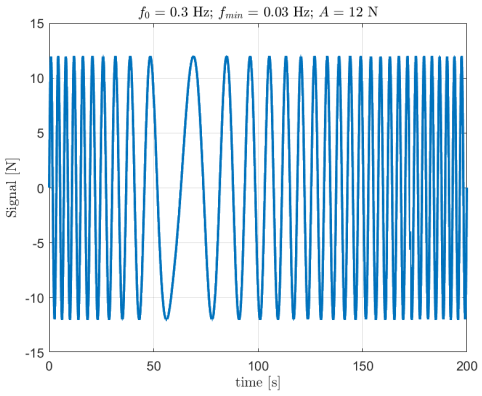

Figure 5.31: Time-varying frequency harmonic

The FFT estimation is performed similarly to the amplitude time-varying case. However, in the following for each time window a time interval $\Delta t = 5$ s is considered. The results are reported in Figures from 5.32 to 5.35.

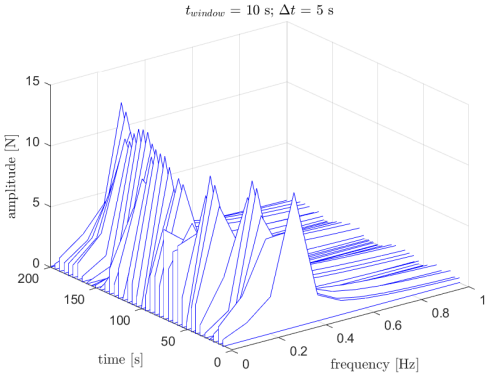

Figure 5.32: FFT estimation with $t_{window} = 10$ s

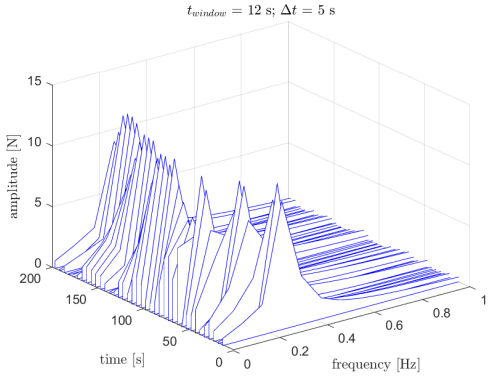

Figure 5.33: FFT estimation with $t_{window} = 12$ s

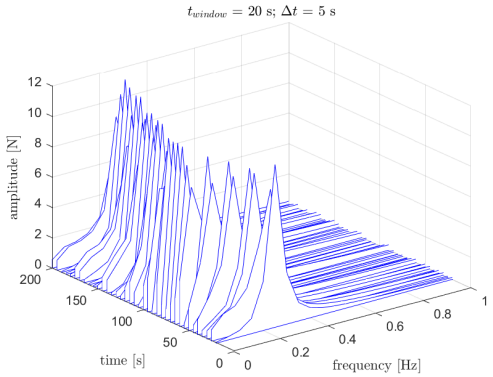

Figure 5.34: FFT estimation with $t_{window} = 20$ s

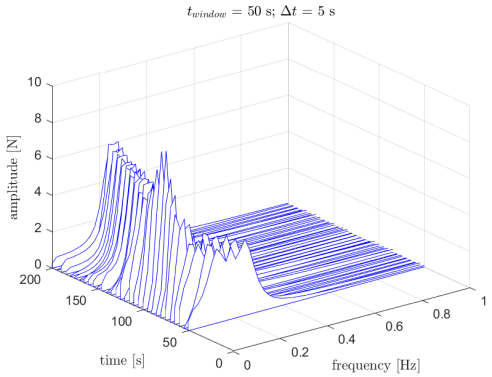

Figure 5.35: FFT estimation with $t_{window} = 50$ s

As previously mentioned, since the frequency changes over time, in each time interval Δt where the FFT is performed, more frequencies of the same harmonic are present. This is reflected in the amplitude spectra, that often do not include a single peak, as it occurred in the time-varying amplitude. This behaviour has here a more relevant effect on amplitude and frequency evaluation with respect to the case of time-varying amplitude and generates much greater estimation errors.

The EKF is again initialized using the same values of the case with constant frequency. From Figure 5.36, it can be noted that the EKF is able to recover the time variation of the frequency, even if it does not include information about its variation and it has been implemented considering the case with constant frequency, exactly as the case with amplitude changing in time.

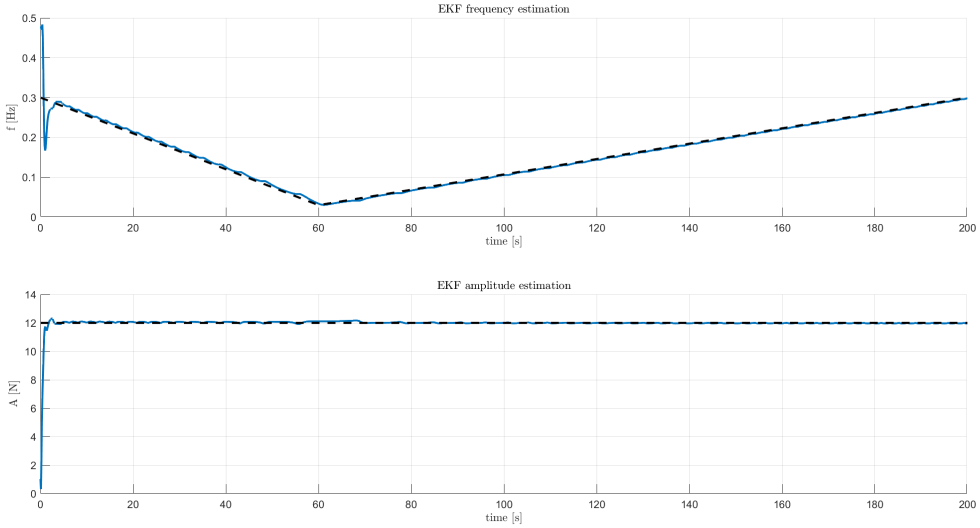

Figure 5.36: EKF estimation – time-varying frequency

The estimation error for the FFT and the EKF in the time-varying frequency case is depicted in Figure 5.37. It is clear that the FFT does not perform well and tends to oscillate for both the amplitude and frequency estimation errors. On the contrary, the EKF produces small errors for both the quantities to be estimated.

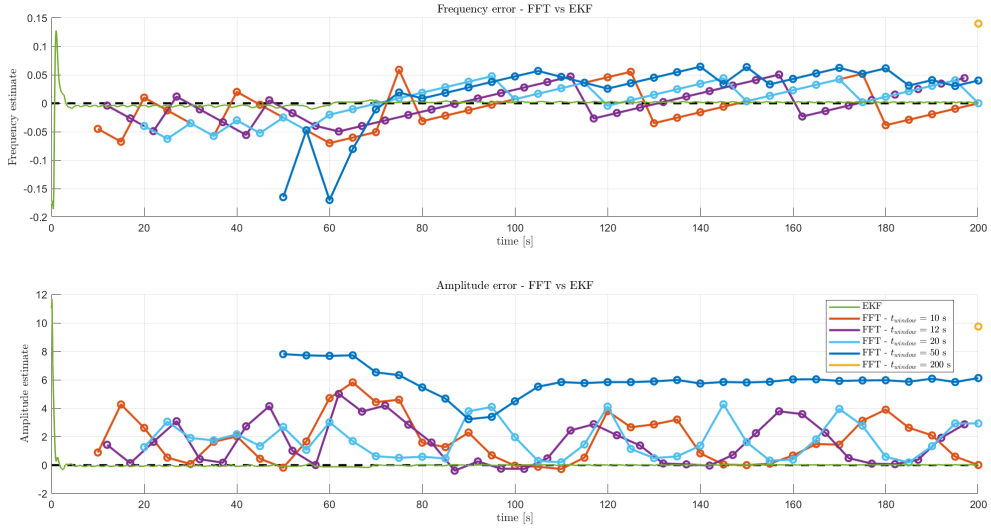

Figure 5.37: FFT and EKF estimation comparison – time-varying frequency

5.4.5 Disturbance as one harmonic with amplitude and frequency varying in time

This last case considers once again the input disturbance to be a single harmonic, but unlike the previous examples the perturbation generated by the gearbox varies both in amplitude and in frequency over time, as shown in Figure 5.38. This example can be viewed as an integration of the two previous cases. In fact, the same considerations as before still hold.

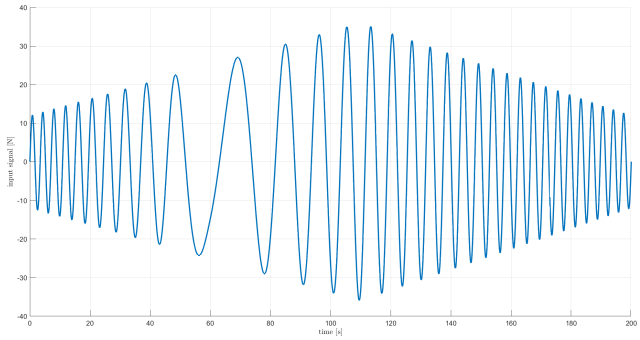

Figure 5.38: Time-varying amplitude and frequency harmonic

Short time windows for the implementation of the FFT approach are selected to generate better estimates of the disturbance frequency and amplitude due to their variation over time. A shorter time window t_{window} improves the estimation accuracy, but increases the computational effort. In addition, since the frequency changes over time, the amplitude spectrum does not generate a unique peak for the same time window because of the numerous frequency components within the time interval. The same effect is generated by the amplitude variation, which degrades even further the estimation.

This example validates again the superiority of the estimation produced by the EKF in the case of a single harmonic whose characteristic parameters change over time. The

EKF frequency and amplitude estimation are depicted in Figure 5.39. The filter is once again implemented by assuming that the input disturbance has constant parameters, nonetheless the EKF is able to recover accurately their variation over time in real-time by means of the information provided by the upstream robust $\mathcal{H}_\infty$ estimator.

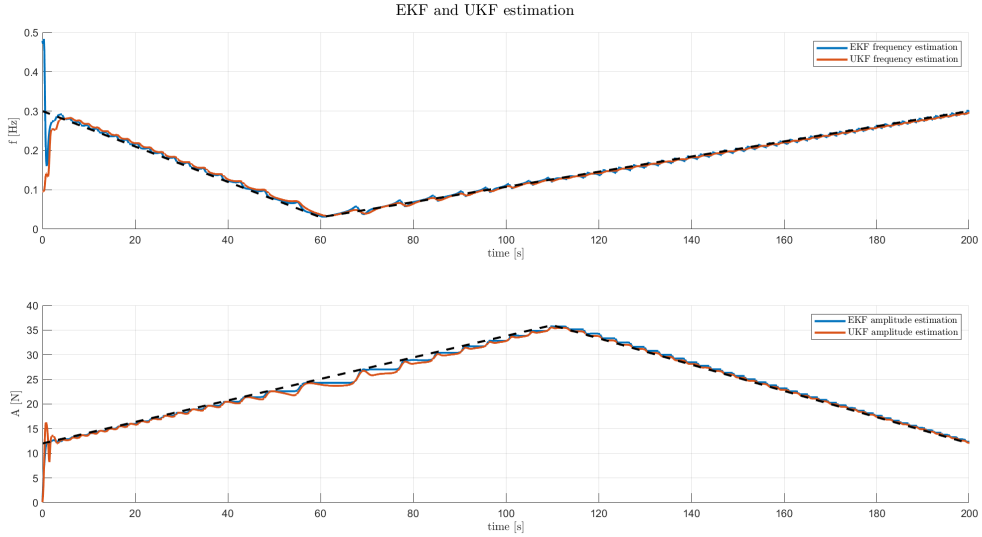

Figure 5.39: EKF and UKF estimation – time-varying amplitude and frequency

Furthermore, the UKF is implemented for the estimation of this last example. The red line in Figure 5.39 reconstructs the amplitude and frequency variation over time by using the UKF as nonlinear estimation technique. There is no relevant difference with the EKF estimation and this conclusion can be observed in Figure 5.40 as well, which represents the estimation error of all the implemented approaches, including the FFT with time interval $\Delta t = 2$ s. The similar behaviour of the UKF with respect to the EKF demonstrates that the latter method is particularly suitable for the cases investigated so far, as it reduces the computational burden of the UKF and produces analogous results.

To sum up, table 5.3 shows the main features of the two estimation methods treated in this chapter. It can be noted that both of them have advantages and drawbacks depending on the shape of the input signal. A careful analysis of the specific case at hand shall then be performed before making the final choice of the optimal estimation technique.

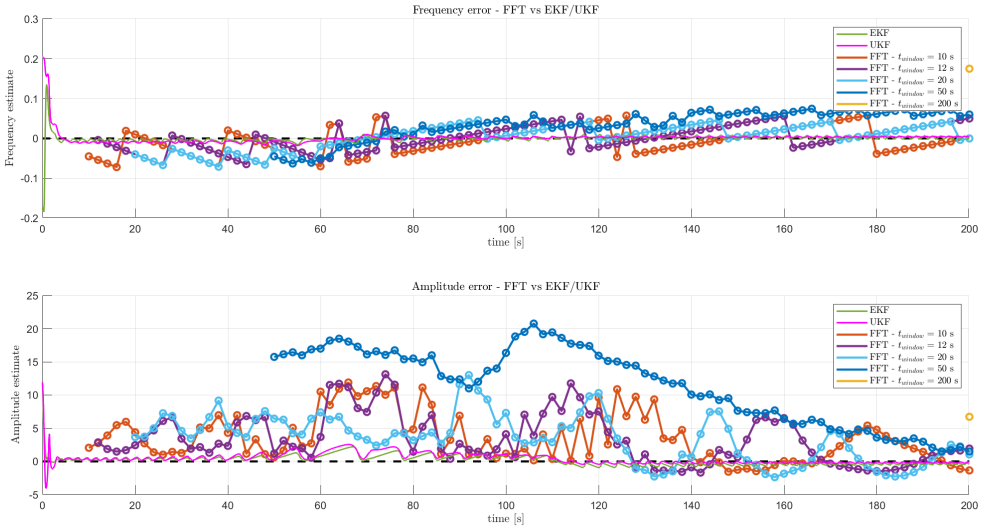

Figure 5.40: FFT, EKF and UKF estimation comparison – time-varying amplitude and frequency

EKF	**FFT**
real-time estimation	*a posteriori* estimation
information about the shape of the input signal required	no prior information about the signal required
number of harmonics generating the signal required	spectral leakage may occur, depending on t_{window}
must be reasonably initialized - reasonable choice of $\hat{\mathbf{x}}_0$, $\mathbf{P}_0$, $\mathbf{Q}$	a time window must be reasonably selected
able to capture input amplitude and frequency variations	poor performance if input frequency varies over time

Table 5.3: Comparison between EKF and FFT estimation techniques

Chapter 6

Solar array drive mechanism disturbance estimation

6.1 Sentinel-2 state-space representation

THE dynamic model of Sentinel-2A has been extensively described in chapter 2 by means of the satellite dynamics toolbox embedded with the solar array drive mechanism (SDT+). The block diagram of such system is represented in Figure 2.7, which shows the connection of the subsystems and the detailed relations of all variables involved in the satellite dynamics.

Since the spacecraft is assumed to have small angular velocities $\dot{\boldsymbol{\omega}}$ as external perturbations and thus motion are typically small during the operational phase, the overall dynamics of Sentinel-2 can be considered to be linear. Accordingly, the global system can be described in a state-space representation, which is particularly useful for the subsequent development of the estimator. To obtain this result, equations derived in chapter 2 are reported here and rearranged in a state-space representation for each subsystem, and then integrated together to generate the description of the overall system.

Satellite hub

The dynamics of the spacecraft hub is obtained by introducing the following state:

$$\mathbf{x}_{HUB}(t) = \begin{Bmatrix} \mathbf{v}_G \\ \boldsymbol{\omega} \end{Bmatrix}_{\mathcal{R}_B} = \begin{Bmatrix} v_{x,G} \\ v_{y,G} \\ v_{z,G} \\ \omega_x \\ \omega_y \\ \omega_z \end{Bmatrix}_{\mathcal{R}_B} \tag{6.1}$$

which encompasses the angular velocities $\boldsymbol{\omega}$ and the translational velocities of the hub's centre of mass $\mathbf{v}_G$ expressed in the frame $\mathcal{R}_B$ rigidly attached to the satellite base. The input vector can be expressed as:

$$\mathbf{u}_{HUB}(t) = \left\{ \begin{bmatrix} \mathbf{F} \\ T_{HUB} \\ T_{y,P} \\ T_{z,P} \end{bmatrix}_{\mathcal{R}_A} \right\} \tag{6.2}$$

$$\left\{ \begin{bmatrix} \mathbf{F}_{ext} \\ \mathbf{T}_{ext,G} \end{bmatrix}_{\mathcal{R}_B} \right\}$$

where $\mathbf{F}$ and $\mathbf{T}_P = [T_{x,P}\ T_{y,P}\ T_{z,P}]^T = [-T_{HUB}\ T_{y,P}\ T_{z,P}]^T$ are the forces and torques generated by the appendage at the connection point P on the satellite rigid base expressed in the reference frame $\mathcal{R}_A$, whereas $\mathbf{F}_{ext}$ and $\mathbf{T}_{ext,G}$ are respectively the external forces and torques acting on the hub's centre of mass G written in the frame $\mathcal{R}_B$. Furthermore, the output vector is defined as:

$$\mathbf{y}_{HUB}(t) = \left\{ \begin{bmatrix} \mathbf{v}_G \\ \boldsymbol{\omega} \end{bmatrix}_{\mathcal{R}_B} \begin{bmatrix} \mathbf{a}_G \\ \dot{\boldsymbol{\omega}} \end{bmatrix}_{\mathcal{R}_B} \begin{bmatrix} \mathbf{a}_P \\ \dot{\boldsymbol{\omega}} \end{bmatrix}_{\mathcal{R}_A} \right\} \tag{6.3}$$

The state dynamics and the output equations can then be computed as:

$$\dot{\mathbf{x}}_{HUB}(t) = \mathbf{0}_{6\times6}\mathbf{x}_{HUB}(t) + \begin{bmatrix} \mathbf{D}_B^{-1}\boldsymbol{\tau}_{PG}^T\mathbf{R}_{HUB}^T\mathbf{I}_{T_x} & \mathbf{D}_B^{-1} \end{bmatrix} \mathbf{u}_{HUB}(t) \tag{6.4}$$

$$\mathbf{y}_{HUB}(t) = \begin{bmatrix} \mathbf{I}_6 \\ \mathbf{0}_6 \\ \mathbf{0}_6 \end{bmatrix} \mathbf{x}_{HUB}(t) + \begin{bmatrix} \mathbf{0}_6 & \mathbf{0}_6 \\ \mathbf{D}_B^{-1}\boldsymbol{\tau}_{PG}^T\mathbf{R}_{HUB}^T\mathbf{I}_{T_x} & \mathbf{D}_B^{-1} \\ \mathbf{R}_{HUB}\boldsymbol{\tau}_{PG}\mathbf{D}_B^{-1}\boldsymbol{\tau}_{PG}^T\mathbf{R}_{HUB}^T\mathbf{I}_{T_x} & \mathbf{R}_{HUB}\boldsymbol{\tau}_{PG}\mathbf{D}_B^{-1} \end{bmatrix} \mathbf{u}_{HUB}(t) \tag{6.5}$$

where $\mathbf{D}_B^{-1}$ is the linear inverse dynamic model of the spacecraft base, $\boldsymbol{\tau}_{PG}$ is the kinematic model from point G to the appendage connection point P and can be computed as:

$$\boldsymbol{\tau}_{PG} = \begin{bmatrix} \mathbf{I}_3 & [\mathbf{r}_{PG}]^\wedge \\ \mathbf{0}_3 & \mathbf{I}_3 \end{bmatrix} \tag{6.6}$$

and $\mathbf{r}_{PG} = -\mathbf{r}_{GP}$. In addition, $\mathbf{R}_{HUB}$ is a 6×6 block matrix defined as:

$$\mathbf{R}_{HUB} = \begin{bmatrix} \mathbf{R}_{B/A} & \mathbf{0}_3 \\ \mathbf{0}_3 & \mathbf{R}_{B/A} \end{bmatrix} \tag{6.7}$$

where $\mathbf{R}_{B/A}$ is the rotation matrix from the hub's frame $\mathcal{R}_B$ to frame $\mathcal{R}_A$. To conclude, $\mathbf{I}_{T_x} = \text{diag}(1, 1, 1, -1, 1, 1)$ is a diagonal matrix which changes the sign of the torque T_{HUB} applied at connection point P around the direction of the solar array rotational axis.

More compactly, the dynamics of the satellite hub is then rewritten as:

$$\begin{aligned} \dot{\mathbf{x}}_{HUB}(t) &= \mathbf{A}_{HUB}\mathbf{x}_{HUB}(t) + \mathbf{B}_{HUB}\mathbf{u}_{HUB}(t) \\ \mathbf{y}_{HUB}(t) &= \mathbf{C}_{HUB}\mathbf{x}_{HUB}(t) + \mathbf{D}_{HUB}\mathbf{u}_{HUB}(t) \end{aligned} \tag{6.8}$$

where $\mathbf{A}_{HUB}$, $\mathbf{B}_{HUB}$, $\mathbf{C}_{HUB}$, and $\mathbf{D}_{HUB}$ are defined by equations (6.4) and (6.5).

Stepper motor

The stepper motor dynamics expressed as state-state representation is described by the following equations:

$$\dot{\mathbf{x}}_m(t) = \begin{bmatrix} 0 & 1 \\ -\frac{K_0}{J_r} & -\frac{C_0}{J_r} \end{bmatrix} \begin{Bmatrix} \theta_r \\ \dot{\theta}_r \end{Bmatrix} + \begin{bmatrix} 0 & 0 & 0 \\ \frac{1}{J_r} & -1 & \frac{K_m I \gamma}{J_r} \end{bmatrix} \begin{Bmatrix} T_{i/r} \\ [\dot{\omega}_x]_{\mathcal{R}_A} \\ i \end{Bmatrix} \tag{6.9}$$

$$\mathbf{y}_m(t) = \begin{Bmatrix} \ddot{\theta}_i \\ T_{HUB} \end{Bmatrix} = \begin{bmatrix} -\frac{K_0}{J_r} & -\frac{C_0}{J_r} \\ -K_0 & -C_0 \end{bmatrix} \begin{Bmatrix} \theta_r \\ \dot{\theta}_r \end{Bmatrix} + \begin{bmatrix} \frac{1}{J_r} & 0 & \frac{K_m I \gamma}{J_r} \\ 0 & 0 & K_m I \gamma \end{bmatrix} \begin{Bmatrix} T_{i/r} \\ [\dot{\omega}_x]_{\mathcal{R}_A} \\ i \end{Bmatrix} \tag{6.10}$$

or, more compactly:

$$\begin{aligned} \dot{\mathbf{x}}_m(t) &= \mathbf{A}_m \mathbf{x}_m(t) + \mathbf{B}_m \mathbf{u}_m(t) \\ \mathbf{y}_m(t) &= \mathbf{C}_m \mathbf{x}_m(t) + \mathbf{D}_m \mathbf{u}_m(t) \end{aligned} \tag{6.11}$$

Gearbox

The state-space representation of the gearbox dynamics in terms of state dynamics and output equations can be written as follow:

$$\dot{\mathbf{x}}_g(t) = \begin{bmatrix} 0 & 1 \\ -\frac{K_g}{J_o} & -\frac{C_g}{J_o} \end{bmatrix} \begin{Bmatrix} \delta\theta \\ \delta\dot{\theta} \end{Bmatrix} + \begin{bmatrix} 0 & 0 & 0 \\ \frac{1}{J_o} & -\frac{1}{N_g} & \frac{1}{J_o} \end{bmatrix} \begin{Bmatrix} T_{SA/o} \\ \ddot{\theta}_i \\ T_{PERT} \end{Bmatrix} \tag{6.12}$$

$$\mathbf{y}_g(t) = \begin{Bmatrix} \ddot{\theta}_o \\ T_{i/r} \\ \delta\theta \end{Bmatrix} = \begin{bmatrix} -\frac{K_g}{J_o} & -\frac{C_g}{J_o} \\ \frac{K_g}{N_g} & \frac{C_g}{N_g} \\ 1 & 0 \end{bmatrix} \begin{Bmatrix} \delta\theta \\ \delta\dot{\theta} \end{Bmatrix} + \begin{bmatrix} \frac{1}{J_o} & 0 & \frac{1}{J_o} \\ 0 & -J_i & -\frac{1}{N_g} \\ 0 & 0 & 0 \end{bmatrix} \begin{Bmatrix} T_{SA/o} \\ \ddot{\theta}_i \\ T_{PERT} \end{Bmatrix} \tag{6.13}$$

or, alternatively:

$$\begin{aligned} \dot{\mathbf{x}}_g(t) &= \mathbf{A}_g \mathbf{x}_g(t) + \mathbf{B}_g \mathbf{u}_g(t) \\ \mathbf{y}_g(t) &= \mathbf{C}_g \mathbf{x}_g(t) + \mathbf{D}_g \mathbf{u}_g(t) \end{aligned} \tag{6.14}$$

Solar array

The solar array dynamics can be described in a state-space representation using the following relations:

$$\dot{\mathbf{x}}_{SA}(t) = \begin{bmatrix} \mathbf{0}_n & \mathbf{I}_n \\ -\operatorname{diag}(\omega_i^2) & -\operatorname{diag}(2\xi_i\omega_i) \end{bmatrix} \begin{Bmatrix} \boldsymbol{\eta} \\ \dot{\boldsymbol{\eta}} \end{Bmatrix} + \begin{bmatrix} \mathbf{0}_{n\times 6} \\ -\mathbf{L}_P \end{bmatrix} \begin{Bmatrix} \mathbf{a}_P \\ \dot{\boldsymbol{\omega}} \end{Bmatrix}_{\mathcal{R}_{SA}} \tag{6.15}$$

$$\mathbf{y}_{SA}(t) = \begin{Bmatrix} \mathbf{F} \\ \mathbf{T}_C \end{Bmatrix}_{\mathcal{R}_{SA}} = \begin{bmatrix} \mathbf{L}_P^T \operatorname{diag}(\omega_i^2) & \mathbf{L}_P^T \operatorname{diag}(2\xi_i\omega_i) \end{bmatrix} \begin{Bmatrix} \boldsymbol{\eta} \\ \dot{\boldsymbol{\eta}} \end{Bmatrix} + (\mathbf{D}_A^P - \mathbf{L}_P^T \mathbf{L}_P) \begin{Bmatrix} \mathbf{a}_P \\ \dot{\boldsymbol{\omega}} \end{Bmatrix}_{\mathcal{R}_{SA}} \tag{6.16}$$

or, more compactly:

$$\begin{aligned} \dot{\mathbf{x}}_{SA}(t) &= \mathbf{A}_{SA} \mathbf{x}_{SA}(t) + \mathbf{B}_{SA} \mathbf{u}_{SA}(t) \\ \mathbf{y}_{SA}(t) &= \mathbf{C}_{SA} \mathbf{x}_{SA}(t) + \mathbf{D}_{SA} \mathbf{u}_{SA}(t) \end{aligned} \tag{6.17}$$

Rotation from $\mathcal{R}_A$ to $\mathcal{R}_{SA}$

The translational and rotational accelerations of connection point P are obtained from the transported dynamic model of the hub integrated with the dynamics of the solar array driving mechanism along the direction of the appendage rotation axis. Such quantities are conveniently expressed in the reference frame $\mathcal{R}_A$ centred at point P and rigidly attached to the satellite base. On the contrary, the dynamic model of the solar array is computed at its centre of mass C and then transported at connection point P, both more suitably expressed in the frame $\mathcal{R}_{SA}$ fixed with respect to the appendage. Therefore, a rotation matrix is introduced to move from reference frame $\mathcal{R}_A$ to $\mathcal{R}_{SA}$ to work with all the variable in the same frame. The rotation is dependent on the desired configuration of the solar array, which is commanded during the orbital motion to collect and generate maximum power from the sun. The dependence of rotational angle $\theta(t)$ on time is depicted in Figure 2.4 and coincides with the rotation to be performed to move from frame $\mathcal{R}_{SA}$ to $\mathcal{R}_A$. Such rotation can be expressed in a state-space representation, which – by the way it is defined – will involve only an input-output relation dependent on angle $\theta(t)$ as follows:

$$\mathbf{y}_{R1}(t) = \begin{Bmatrix} \mathbf{a}_P \\ \dot{\boldsymbol{\omega}} \end{Bmatrix}_{\mathcal{R}_{SA}} = \begin{bmatrix} \mathbf{R}_x^T(\theta) & \mathbf{0}_3 \\ \mathbf{0}_3 & \mathbf{R}_x^T(\theta) \end{bmatrix} \begin{Bmatrix} \mathbf{a}_P \\ \ddot{\theta}_o \\ \dot{\omega}_y \\ \dot{\omega}_z \end{Bmatrix}_{\mathcal{R}_A} \tag{6.18}$$

that can be written more concisely as:

$$\mathbf{y}_{R1}(t) = \mathbf{D}_{R1}(\theta)\mathbf{u}_{R1}(t) \tag{6.19}$$

Rotation from $\mathcal{R}_{SA}$ to $\mathcal{R}_A$

Analogously, forces and torques obtained by means of the linear dynamic model of the solar array are expressed in the reference frame $\mathcal{R}_{SA}$ rigidly attached to the appendage. Such quantities are more conveniently used in the frame $\mathcal{R}_A$ fixed with respect to the satellite base and thus a rotation is usually performed. The rotation depends again on the solar array configuration $\theta(t)$ and can be computed as the inverse rotation of the previous one as follows:

$$\mathbf{y}_{R2}(t) = \begin{Bmatrix} \mathbf{F} \\ T_{SA/o,P} \\ T_{y,P} \\ T_{z,P} \end{Bmatrix}_{\mathcal{R}_A} = \begin{bmatrix} \mathbf{R}_x(\theta) & \mathbf{0}_3 \\ \mathbf{0}_3 & \mathbf{R}_x(\theta) \end{bmatrix} \begin{Bmatrix} \mathbf{F} \\ \mathbf{T}_P \end{Bmatrix}_{\mathcal{R}_{SA}} \tag{6.20}$$

or, more compactly:

$$\mathbf{y}_{R2}(t) = \mathbf{D}_{R2}(\theta)\mathbf{u}_{R2}(t) \tag{6.21}$$

Global system

The state variables introduced for each subsystem can be gathered into an augmented state $\mathbf{x}(t)$ defined as:

$$\mathbf{x}(t) = \begin{Bmatrix} \mathbf{x}_{HUB} \\ \mathbf{x}_m \\ \mathbf{x}_g \\ \mathbf{x}_{SA} \end{Bmatrix} = \begin{Bmatrix} \mathbf{v}_G \\ \boldsymbol{\omega} \\ \theta_r \\ \dot{\theta}_r \\ \delta\theta \\ \delta\dot{\theta} \\ \boldsymbol{\eta} \\ \dot{\boldsymbol{\eta}} \end{Bmatrix} \tag{6.22}$$

such that the entire satellite dynamics is represented by a single augmented system which encompasses all the subsystems. Such augmented system can be expressed in a state-space representation as follows:

$$\begin{aligned} \dot{\mathbf{x}}(t) &= \mathbf{A}(\theta)\mathbf{x}(t) + \mathbf{B}(\theta)\mathbf{u}(t) \\ \mathbf{y}(t) &= \mathbf{C}(\theta)\mathbf{x}(t) + \mathbf{D}(\theta)\mathbf{u}(t) \end{aligned} \tag{6.23}$$

It is important to note that both the state dynamic equation and the output equation depend on the variable θ which defines the configuration of the solar array. As already mentioned, the evolution of angle $\theta(t)$ over time is well-known, since it is a design parameter that depends on the spacecraft position along the orbit with respect to the sun. Nonetheless, the variation of θ influences the global dynamics of the system in terms of time variation in the construction of all the matrices in the state-space representation of the system itself. This entails that the global system is not a linear time-invariant system, since the time-invariance assumption is no longer valid. However, it is still possible to define a Linear Parameter Varying (LPV) model of the system valid for any value of θ as described by Alazard and Cumer in [1], which preserves the time-invariance of the system and allows to carry out the pertinent analysis by means of the existing tools for time-invariant systems. This is a powerful approach to be used as it greatly simplifies the treatment of the problem at hand.

Using the augmented system described in equation 6.23, the external input variables of the system are then:

$$\mathbf{u}(t) = \begin{Bmatrix} \mathbf{F}_{ext} \\ \mathbf{T}_{ext,G} \\ i \\ T_{PERT} \end{Bmatrix} \tag{6.24}$$

whereas the relevant output quantities that can be inferred from the system dynamics are:

$$\mathbf{y}(t) = \begin{Bmatrix} \mathbf{v}_G \\ \boldsymbol{\omega} \\ \mathbf{a}_G \\ \dot{\boldsymbol{\omega}} \\ \delta\theta \end{Bmatrix} \tag{6.25}$$

6.2 Gearbox perturbation characterisation

Any perturbation at SADM level is related to phenomena resulting in small variations of the output shaft angular velocity $\dot{\theta}_o$ with respect to its theoretical and desired configuration. In the gearbox case, the generated disturbances are ascribed to damages

and imperfections of its components. In particular, sources of such perturbations are produced by several causes, including gear teeth geometry errors (such as profile, spacing, and runout errors from the manufacturing process), elastic deformation, imperfect mounting or alignment, lubrication. Therefore, the accurate analysis and modeling of the disturbances with respect to the theoretical configuration is complicated by the numerous error sources that arise during operation and may be difficult to predict. Penaud et al. developed a general model [24] for the kinematic analysis of geared mechanisms, that can be used to compute and characterise such disturbances. Starting from the kinematic model of the gearbox and from the parameters of its constituents, it is then possible to compute the frequency f_i of the i-th contact damage in any gear pairs of any mechanism which is likely to be generated by the error sources. Each damage can generate some harmonic disturbance torque involving the fundamental frequency of the single damage $\omega_{d_i} = 2\pi f_i$ and the related higher frequency harmonics with $f_{i_k} = kf_i$, for $k = 2, 3, ..., N_h$, as described in [1]. The overall perturbation can be computed as:

$$T_{PERT} = \sum_{i=1}^{n_d} \sum_{k=1}^{N_h} A_{i_k} \sin\left(k\omega_{d_i} t + \varphi_{i_k}\right) \tag{6.26}$$

where n_d is the total number of damages in the gearbox, N_h is the number of harmonics for each damage, while the magnitude A_{i_k} and the phase φ_{i_k} depend on the shape of the damage.

By inserting the Sentinel-2 gearbox kinematic model into the toolbox mentioned above (Figure 2.5), 6 main damages in the mechanism and the relative fundamental frequencies are identified and reported in table 6.1. It is interesting to note that all of them depend on the angular velocity $\dot{\theta}_o$ (ω_{SA} in the table) of the shaft that makes the solar array rotate and increase as $\dot{\theta}_o$ grows.

Damage i	$\widetilde{\omega}_{d_i} = \omega_{d_i}/\omega_{SA}$	Gear pair
1	13616	(2,3)
2	184	(2,3)
3	197.3	(2,3)
4	14800	(3,4)
5	197.3	(3,4)
6	185	(3,4)

Table 6.1: Contact damage frequencies in Sentinel-2 gearbox mechanism

To compare simulation results with real data, analyses on IMU rate measurements from Sentinel-2 telemetry were performed. In particular, a detailed frequency domain analysis was carried out to identify the spectral contributions to the rate error signal. A remarkable outcome is the value of the lowest spectral contribution, which can be approximated as $\omega_0 = N_g\omega_{SA} = 184\omega_{SA}$, where N_g is the transmission ratio of Sentinel-2 gearbox. The approximated value can thus be computed during the forward operational mode of the solar array and the frequency value $f_0 = 0.0307$ Hz is obtained, compared to the slightly different actual value of 0.0327 Hz. Therefore, the transmission ratio N_g plays a significant role for the disturbance generation, and can be physically viewed as the number of times that the disturbance repeats over one SADM output revolution, which equivalently means that it repeats about once for each full stepper motor shaft revolution. A second disturbance is obtained from telemetry data in a similar manner

with gain value 197 with respect to ω_{SA}. Again, this value was computed from the kinematic analysis of the gearbox and listed in table 6.1. In particular, this second disturbance repeats 197 to 198 times over one SADM output shaft revolution, or once for each full step motor shaft revolution.

In addition, almost all higher frequency spectral contributions can be associated with a multiple of either one of the two previous fundamental frequencies, i.e. $f_{i_k} = kf_i$.

Amplitudes of higher harmonics tend to decrease as k gets larger. Therefore, the first components may be strong enough to generate a non-negligible perturbation, while higher harmonics create significant disturbance only if approaching a solar array resonance frequency. These considerations are essential for the gearbox modeling and the estimation of the associated disturbances.

Another important factor for the amplitude and phase computation of all the frequency components is the disturbance shape. From telemetry data it can be shown that the i-th disturbance associated to the i-th gearbox damage can be accurately approximated as a sawtooth signal of the form:

$$T_{PERT_i}(t) = \sum_{k=1}^{N_h} -\frac{2a}{k\pi}(-1)^k \sin\left(k\omega_{d_i} t\right) \tag{6.27}$$

where N_h is the number of harmonics considered to generate the signal, $a = 0.5$, and ω_{d_i} is the i-th harmonic fundamental frequency. In particular, for $N_h = 60$, the single contributions of damages #2 and #3 are shown in Figure 6.1 and the overall gearbox disturbance is depicted in Figure 6.2.

Such signals represent exactly the gearbox disturbance that the estimator to be synthesised must be able to evaluate along with their amplitude and frequency, in order to avoid any coupling with the solar array flexible modes which would degrade its pointing performance.

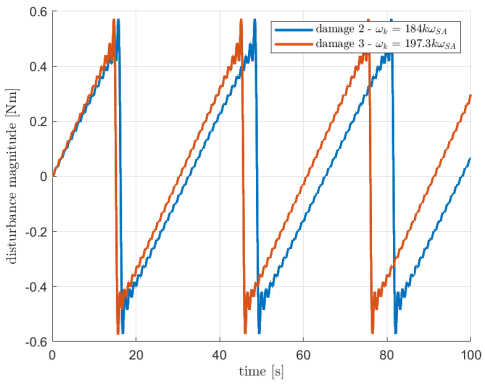

Figure 6.1: Sentinel-2 gearbox damages # 2 and #3

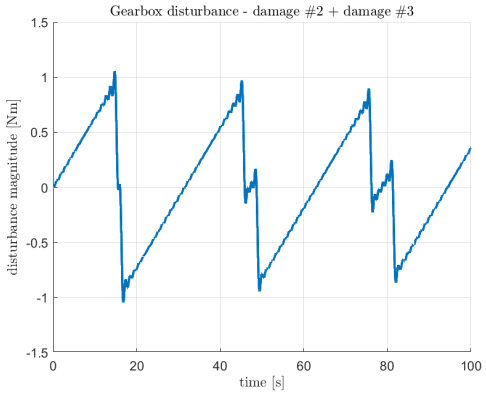

Figure 6.2: Modeled Sentinel-2 gearbox global disturbance

6.3 Robust disturbance estimation

The estimation of the spectral content generated by the gearbox disturbance acting on the system is treated with the same approach described in chapter 5. Since the dynamics of Sentinel-2 is linear, the input disturbance is estimated by means of two filters in series. The first part is devoted to the robust estimation of the input disturbance $d(t)$ using the $\mathcal{H}_\infty$ theory and the real-time data available from the on-board gyroscopes. In fact, this is

possible because of the linearity of the system. The main difference with the simple mass-spring-damper case is the variation of the satellite dynamics due to the rotation of the solar array around its axis. However, the system can still be considered to be linear and time-invariant by using the LPV approach already mentioned thanks to the knowledge of the time evolution of such rotation $\theta(t)$. The robust estimate $\hat{d}(t)$ is then processed by the second part of the filter as the input information for the implementation of a nonlinear estimation technique or of a Fourier transform to evaluate the values of both amplitude and frequency of the harmonics in which the input signal can be decomposed.

As described by the equations in (6.23) the global satellite dynamics can be expressed in a state-space representation and simplified by considering as input and output variables only the quantities of interest. In particular, the gearbox disturbance torque $d(t) = T_{PERT}(t)$ will represent the only input variable, while the angular velocities of the spacecraft $\boldsymbol{\omega}$ measured by the on-board sensors are the outputs that will be taken into account, as shown in the block diagram depicted in Figure 6.3.

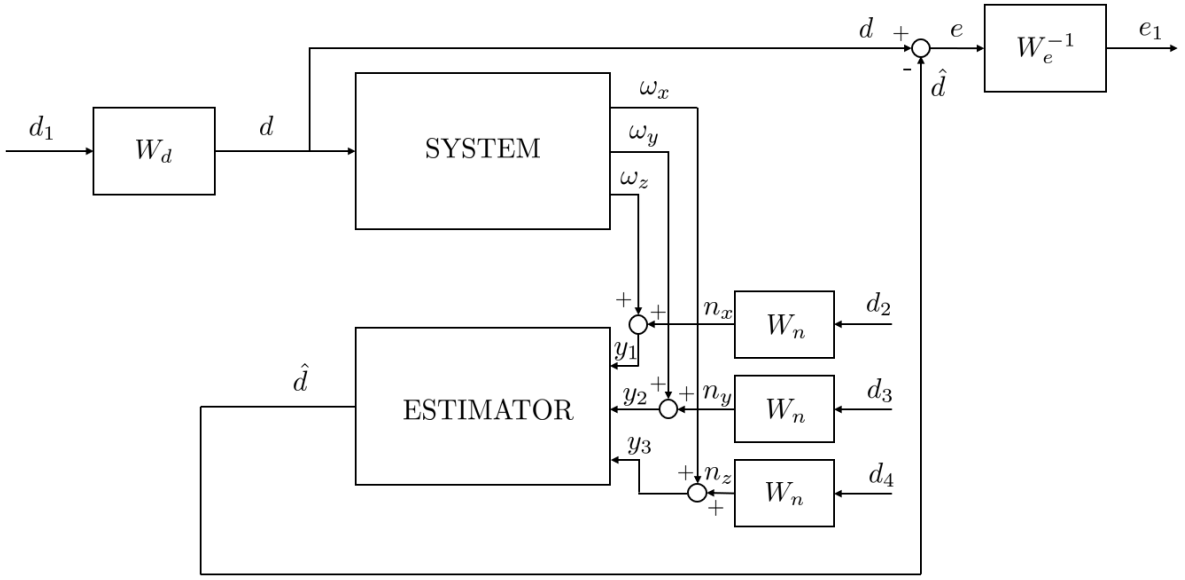

Figure 6.3: Sentinel-2 block diagram for gearbox disturbance estimation

The weighting functions $W_d(s)$, $W_n(s)$ and $W_e^{-1}(s)$ are designed with the same approach described in section 5.3. The disturbance weighting function $W_d(s)$ is a band-pass filter with bandwidth defined by the minimum and maximum frequency components of the disturbance model. The lowest value of the modeled sawtooth signal for both damages occurs at the fundamental frequency of damage #2 when the solar array is in forward mode, i.e. $\omega_m = 184\omega_{SA} = 0.1927$ rad/s. The largest frequency value is dependent upon the number of harmonics N_h considered to generate the model of the signal. In the real case, infinite components should be taken into account, however the amplitude of the components at high frequency do not produce relevant contribution to the signal. For $N_h = 60$ harmonics the maximum value of the frequency components is generated during the solar array backward mode. Nonetheless, the only mode of interest is the forward mode of the solar panel, since during the rewind mode the satellite is in eclipse and no performance requirements with respect to the pointing accuracy are defined. The maximum value for the disturbance weighting function can then be considered the frequency $\omega_M = 60 \cdot 197.3\omega_{SA} = 12.3967$ rad/s. The noise weighting function $W_n(s)$ depends on the

characteristics of the sensors. Since small information about the on-board gyroscopes is available, the same expected maximum value for the entire spectrum is considered. In addition, it is assumed that the same type of sensor is used along the three axis of the spacecraft with the same noise characteristics. To conclude, the weighting function $W_e(s)$ related to the normalised estimation error is designed with the same bandwidth of $W_d(s)$ and with amplitude computed by means of an iterative process to obtain the maximum possible value of the parameter γ connected to the suboptimal $\mathcal{H}_\infty$ filter (see equation (3.120) for its definition), while guaranteeing the constraint $\gamma < 1$ to prevent input amplification.

The system shall be then represented in an LFT form to use the $\mathcal{H}_\infty$ theory developed in chapter 3. Figure 6.4 shows the related block diagram, where the exogenous input vector $\mathbf{w}(t)$ is defined as:

$$\mathbf{w}(t) = \begin{Bmatrix} d_1(t) \\ d_2(t) \\ d_3(t) \\ d_4(t) \end{Bmatrix} \tag{6.28}$$

where d_1 represents the normalised input disturbance and the other three inputs are the normalised noise of the sensors placed along the three spacecraft axes. Similarly, the output vector $\mathbf{y}(t)$ encompasses the data measured by the three gyroscopes.

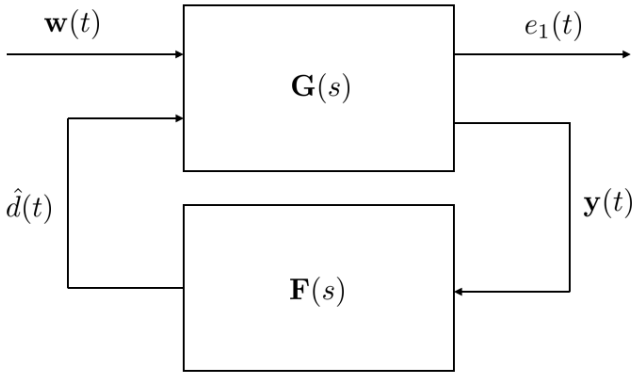

Figure 6.4: Sentinel-2 LFT block diagram representation for gearbox disturbance estimation

The expression of the transfer function $\mathbf{G}(s)$ can then be expressed as follows:

$$\begin{Bmatrix} e_1 \\ \mathbf{y} \end{Bmatrix} = \mathbf{G}(s) \begin{Bmatrix} \mathbf{w} \\ \hat{d} \end{Bmatrix} = \\ = \left[\begin{array}{c|c} \mathbf{G}_{11} & G_{12} \\ \hline \mathbf{G}_{21} & \mathbf{G}_{22} \end{array}\right] \begin{Bmatrix} \mathbf{w} \\ \hat{d} \end{Bmatrix} = \left[\begin{array}{cccc|c} W_e^{-1}W_d & 0 & 0 & 0 & -W_e^{-1} \\ \hline \mathbf{P}W_d & W_n & 0 & 0 & 0 \\ \mathbf{P}W_d & 0 & W_n & 0 & 0 \\ \mathbf{P}W_d & W_n & 0 & W_n & 0 \end{array}\right] \begin{Bmatrix} d_1 \\ d_2 \\ d_3 \\ d_4 \\ \hat{d} \end{Bmatrix} \tag{6.29}$$

where $\mathbf{P}(s)$ is the transfer function of the satellite with input $d(t) = T_{PERT}(t)$ and output the spacecraft angular velocity vector $\boldsymbol{\omega}$.

The $\mathcal{H}_\infty$ filtering generates the estimation $\hat{d}(t)$ which is compared with the real input disturbance $d(t)$ in Figure 6.5 for both the solar array forward mode and backward mode. In particular, the blue line in the figure represents the amplitude of the actual disturbance generated by the SADM gearbox, whereas the red dashed line is the robust estimation produced by the filter. It can be noted that the evaluation provided by the estimator approximates well the time evolution of the real disturbance. A more detailed analysis is obtained by considering the estimation error $e(t)$ computed as the difference between the actual value of the input signal and the value provided by the estimator.

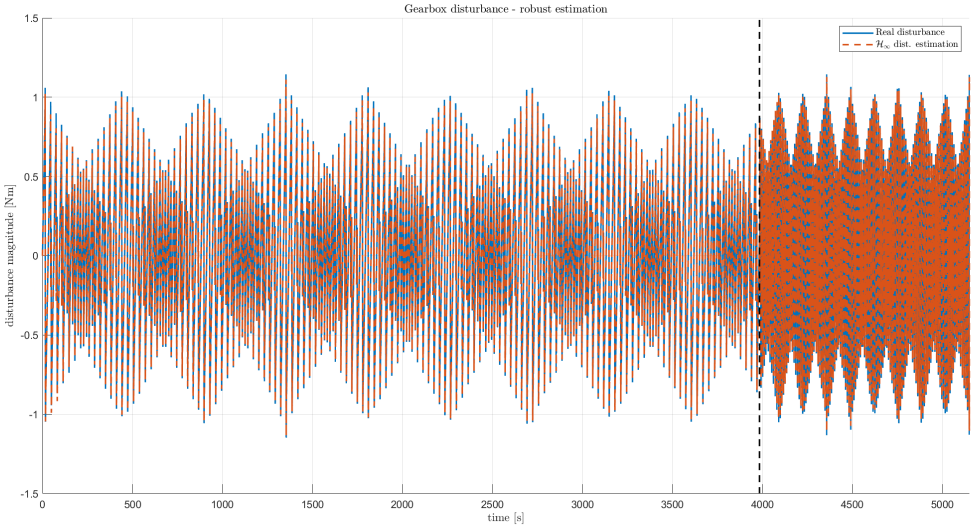

Figure 6.5: Sentinel-2 gearbox disturbance robust estimation

The estimation error $e(t) = d(t) - \hat{d}(t)$ over time is shown in Figure 6.6. It can be noted that after the initial time for both the two configurations, the error shows a repeated pattern bounded to the maximum value 0.03 Nm for the forward mode. Considering the disturbance magnitude, the filter generates an estimation with an average error of 3%. The estimation might be further improved if more detailed information about the sensor characteristics is available and by developing more refined models.

6.4 Disturbance spectral estimation

The disturbance spectral estimation concerns the frequency and amplitude evaluation of the harmonic components that generate the input disturbance. In this case, the input signal is generated by the first part of the filter, which produces a real-time estimate of the gearbox disturbance by means of a robust $\mathcal{H}_\infty$ filtering approach. The second part of the estimator must then rely on the robust estimation of the input disturbance that is treated as the signal generated by a fictitious sensor able to capture the disturbance variation over time.

As already introduced in section 5.4, the two main methods that are used for the spectral estimation of the disturbance are a real-time nonlinear approach that relies on Kalman filter theory and requires information of the input shape and number of harmonics, and a static *a posteriori* approach which is based on the Fourier transform.

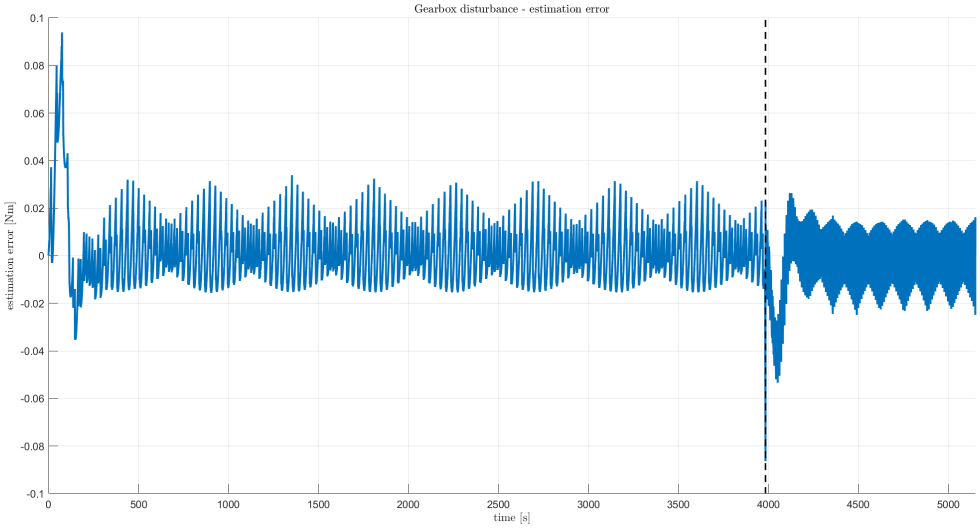

Figure 6.6: Sentinel-2 gearbox disturbance estimation error

6.4.1 Fast Fourier transform estimation

Once the input disturbance is reconstructed via the robust estimator, the fast Fourier transform can be implemented to obtain the signal spectrum, which gives information about the amplitude and the frequency of the harmonics generating the signal itself. This method can be seen as an *a posteriori* approach, since the estimation is not real-time, but requires knowledge of the signal over a time window. In this case, a time window of 1000 s is considered, and after the first FFT computation, the same approach is used every $\Delta t = 500$ s, with the same time window defined above. The results of this approach are reported in Figure 6.7. It is visible from the figure that this method produces several peaks at different frequencies representing the amplitude of the harmonic components that generate the input disturbance. As expected, it can be noted that the amplitude of the single harmonics tends to decrease as the frequency increases. In addition, the amplitude spectrum slightly changes over time following the time evolution of the input signal. An abrupt variation of the spectrum can be identified at time $t = 4500s$, when the FFT makes use of sensor data coming from both the solar array forward operational mode and the rewind mode.

In this case, the FFT approximates well the signal spectrum, however the estimation is not real-time, and requires some time before the first estimation can be carried out. In addition, the time window shall not be too narrow, to avoid poor estimation of the spectrum, nor too wide, to have information of amplitudes and frequencies in short periods of time. Furthermore, since the time window is not a multiple of the period of all the harmonics, the FFT does not approximate exactly the signal spectrum, and generates small peaks at low and high frequency that must be discarded and not confused as further harmonics composing the input disturbance. This behaviour is shown in Figures 6.8 and 6.9. Nonetheless, a first solution that might be implemented to avoid the above errors is the signal tapering through certain window functions, but in turn such approach would create a further degradation in the amplitude estimation of the peaks.

In the case shown in Figure 6.10, the low frequency peaks have been canceled, from *a priori* knowledge of the disturbance fundamental frequency. This figure shows the frequency and amplitude estimation of the first 10 harmonics, i.e. 5 harmonics for each

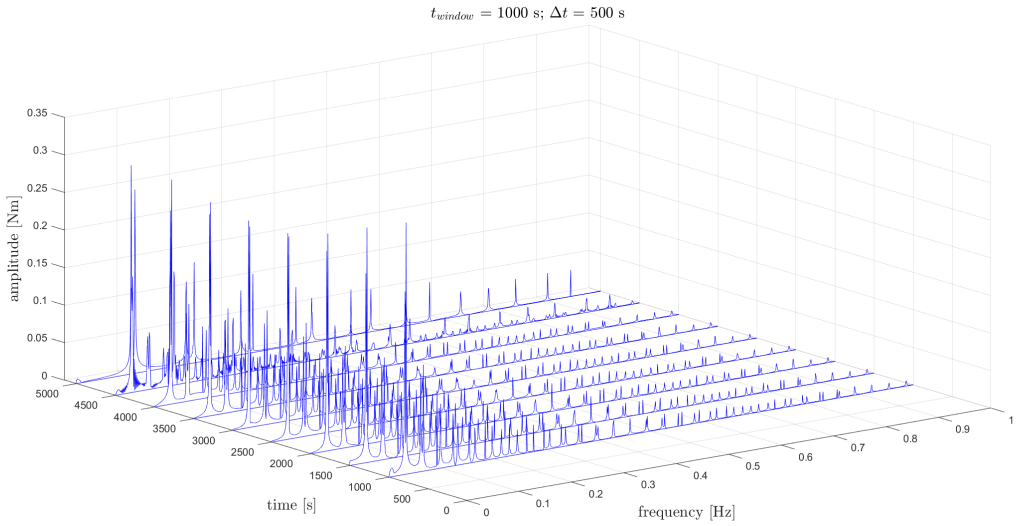

Figure 6.7: Sentinel-2 gearbox disturbance amplitude spectrum over time

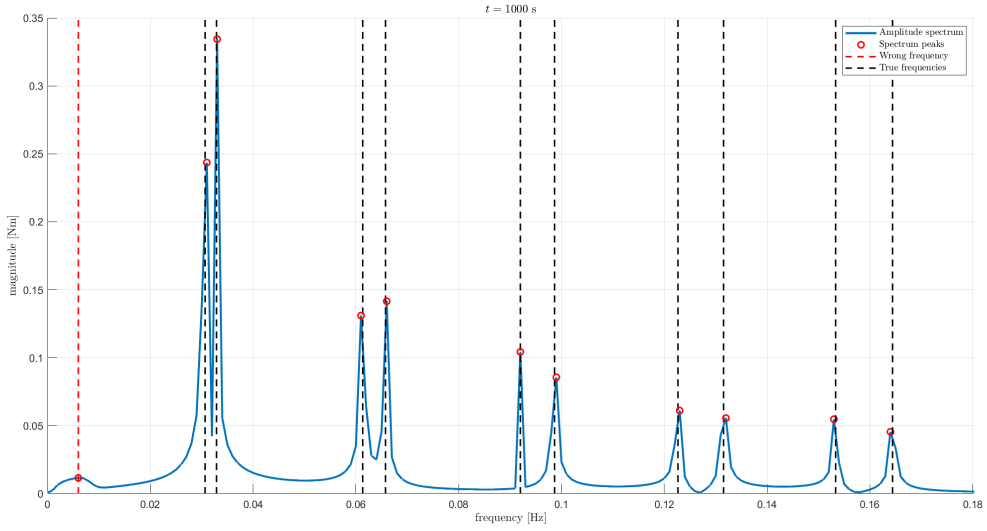

Figure 6.8: Sentinel-2 gearbox disturbance amplitude spectrum at $t = 1000$ s

gearbox damage. It can be noted that at 3000 s, a degradation of the estimation occurs due to a third peak at low frequency, which creates a fictitious harmonic that is not present in the real signal (see also Figure 6.9). At 4000 s and 4500 s, the estimation is rather poor because of the change in the solar array angular velocity (from forward mode to backward mode), which modifies the frequency of the disturbance harmonics. Since for the two above-mentioned intervals the FFT gets information partly from the harmonics in the forward mode and partly in the backward mode, the estimation is wrong. Nonetheless, this situation can be avoided, since the time at which the solar array changes mode is known, and the time windows can be modified accordingly. Moreover, the estimation is in general of interest only during the forward mode, as during the rewind mode the satellite is in eclipse and no solar array pointing requirement shall be fulfilled. To conclude, the estimation is well recovered at 5000 s, where the FFT takes information only from harmonics in the backward mode.

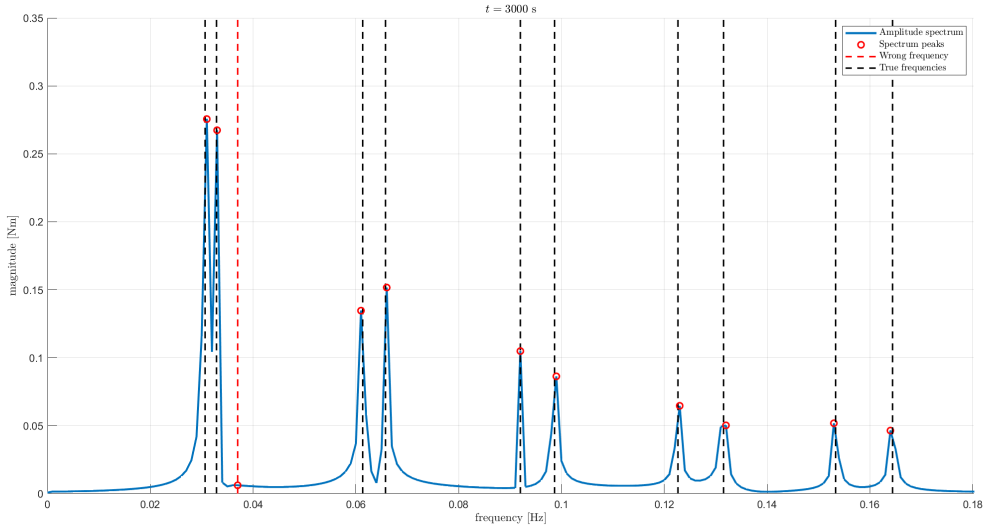

Figure 6.9: Sentinel-2 gearbox disturbance amplitude spectrum at $t = 3000$ s

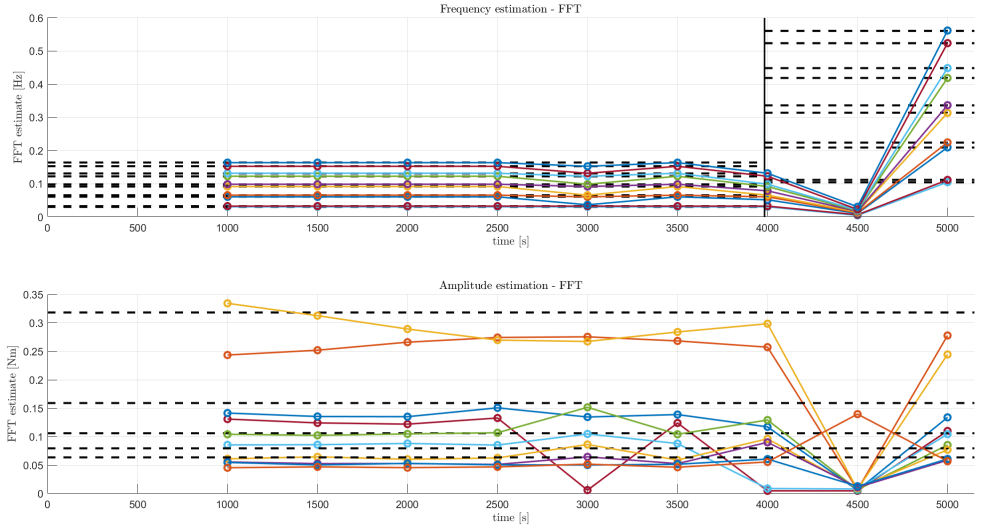

Figure 6.10: Sentinel-2 gearbox disturbance estimation of the first 10 harmonics

Figures 6.11 and 6.12 show the errors of FFT estimation for both harmonics amplitude and frequency respectively. The same considerations previously done still hold and are clearly visible in these images as well. If the intervals where the estimation is poor due to the generation of fictitious peaks are excluded (i.e., 3000 s, 4000 s, and 5000 s), the amplitude estimation error remains under 0.08 Nm, while the frequency estimation error stays beneath 1.5 mHz.

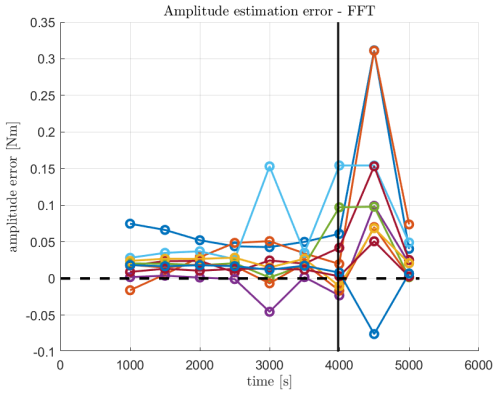

Figure 6.11: FFT amplitude estimation error for the first 10 harmonics

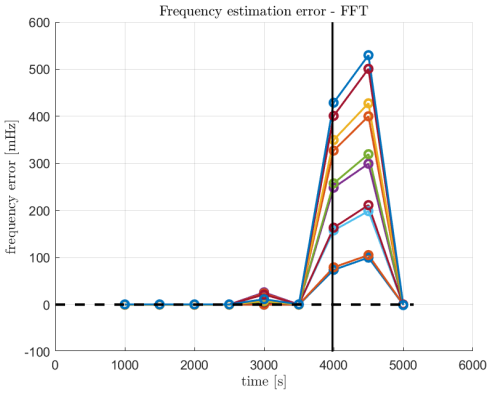

Figure 6.12: FFT frequency estimation error for the first 10 harmonics

6.4.2 Extended Kalman filter estimation

The EKF gives a real-time estimation of the input, and requires no time windows nor frequency spectra. However, knowledge of the signal is essential to construct the states that will estimate the signal. In addition, the initial state estimate $\hat{\mathbf{x}}_0$, as well as the initial state error covariance $\mathbf{P}_0$ and the process noise covariance $\mathbf{Q}$, shall be carefully selected in order to obtain reasonably accurate results, and this step may be rather difficult to perform if there is no information about the input disturbance. In the case $\hat{\mathbf{x}}_0$ perfectly matches the initial value of the real states, the estimation of the frequency for all the 60 harmonics gives extremely precise results, as reported in Figure 6.13.

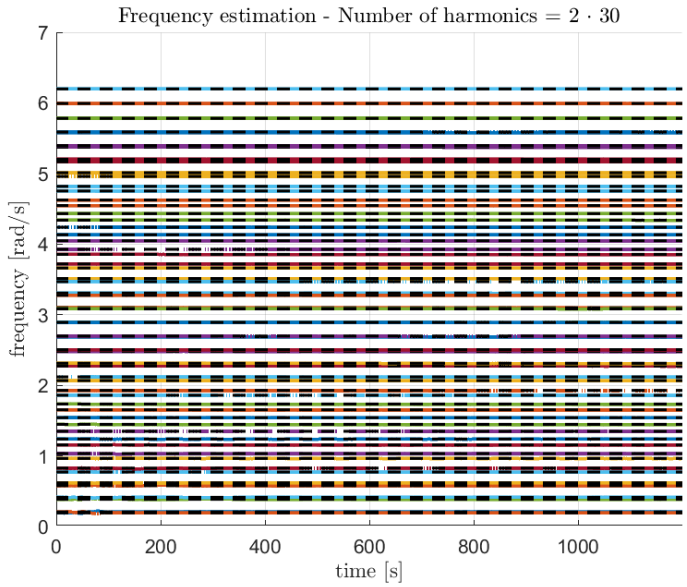

Figure 6.13: EKF frequency estimation of all the harmonic components in the case of perfect knowledge of the initial state

In a more general situation, the initial state is not perfectly known, therefore a 10% error deviation in $\hat{\mathbf{x}}_0$ from the real initial value of the states $\mathbf{x}_0^{real}$ is considered (i.e., $\hat{\mathbf{x}}_0 = 0.9\mathbf{x}_0^{real}$). The EKF simulation is then carried out for the complete simulation time.

The results of the simulation for a total number of harmonics $N_h = 10$ are reported in Figure 6.14 and 6.15 for frequency and amplitude respectively.

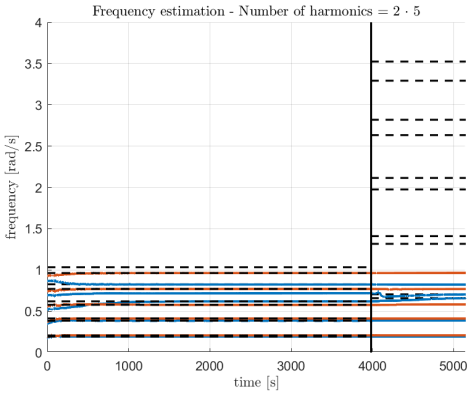

Figure 6.14: EKF frequency estimation for the first 10 harmonics

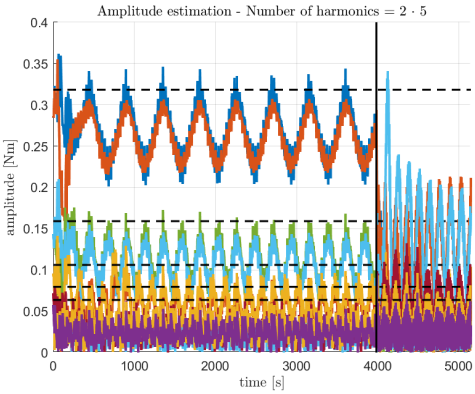

Figure 6.15: EKF amplitude estimation for the first 10 harmonics

It is clearly visible that the amplitude estimation is rather poor and the main cause of this might be due to the intrinsic degradation of the signal because of the presence of the upstream robust filter, which slightly alters the real signal, mainly in its amplitude. The EKF frequency estimation is well recovered for the components at low frequency, whereas it is poor for the ones at higher frequencies, where the estimated value tends to a wrong frequency. This occurs because the error in the initial state $\hat{\mathbf{x}}_0 = 0.9\mathbf{x}_0^{real}$ as selected above, gets bigger for larger values, and some frequencies happen to be initially closer to the value of the next frequency rather than the real one and will tend to that wrong value. The only solution to this issue is a better initial estimation of the state $\hat{\mathbf{x}}_0$. In addition, the same problem occurs when passing from the solar array forward mode to the backward one. The lower frequencies are recovered by the estimate of higher frequencies, which make the other estimates poor while the real high frequencies are not recovered. A possible solution may be to create a new initial state at the time when the solar array changes mode (which is known), but also the new estimate shall be as precise as possible.

To conclude, Figures 6.16 and 6.17 show the EKF estimation error for both frequency and amplitude estimation.

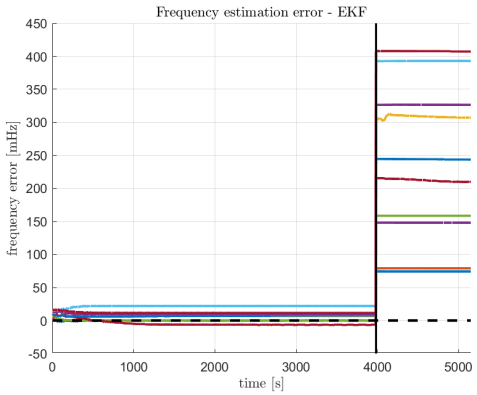

Figure 6.16: EKF frequency estimation error for the first 10 harmonics

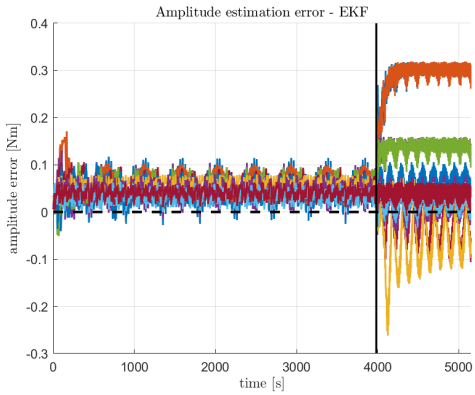

Figure 6.17: EKF amplitude estimation error for the first 10 harmonics

By considering only the forward mode, the largest value of the amplitude error occurs for the fundamental harmonics of the disturbance, with maximum error peaks of about 0.1 Nm at steady-state (the real value of the fundamental harmonic amplitude is $2a/\pi \approx$

0.3183 Nm). As regards frequency, the maximum value of the error remains under 25 mHz (1.5 mHz for FFT estimation). Nonetheless, if only the low frequencies are considered (i.e., the ones for which the value of $\hat{\mathbf{x}}_0$ is relatively close to the real initial value), the estimation error at steady-state remains beneath 0.15 mHz, as shown in Figure 6.18, which validates the previous discussion and makes the EKF more attractive if correctly initialized.

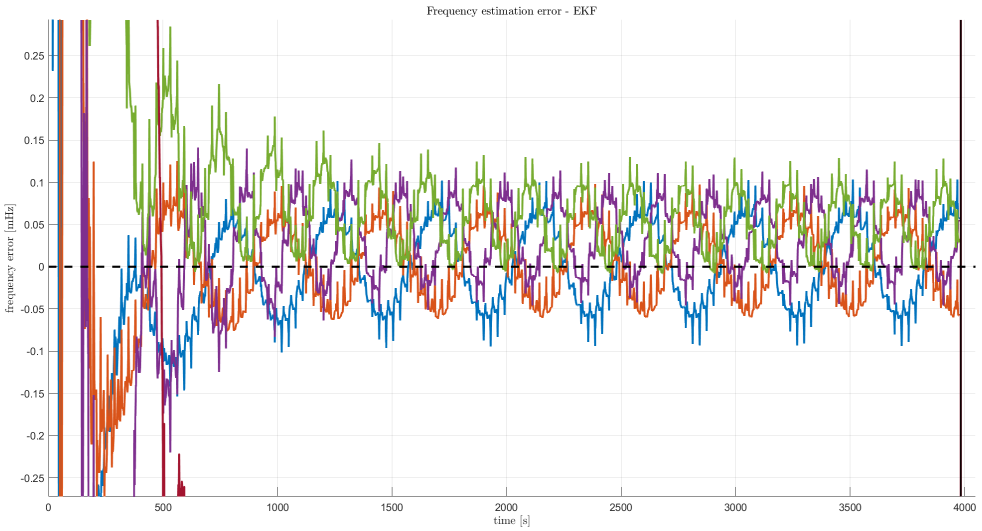

Figure 6.18: EKF frequency estimation error for $\hat{\mathbf{x}}_0$ close to the real value (zoom of Figure 6.16)

Chapter 7

Conclusions

THIS thesis explored different methods for the estimation of the frequency and amplitude spectra of an input signal acting on a linear system. In particular, the case of the estimation of the gearbox disturbance generated by the solar array drive mechanism on-board the Sentinel-2A spacecraft was investigated. The translational and rotational dynamics of the satellite were modeled using the satellite dynamics toolbox developed by Alazard and Cumer in [2], which was later integrated with the dynamics of the stepper motor and the gearbox composing the solar array driving assembly (Alazard and Cumer [1]) which allow the rotation of the appendage. The control of the solar array rotation permits to collect the maximum sun power onto the solar cells in order to provide the spacecraft with a steady energy supply. Nonetheless, both the motor and the gearbox are also sources of disturbances that may be dangerously magnified if coupling with the resonance frequencies of the solar array occurs. The frequency response of the two components of the assembly on the satellite rotational dynamics was explored and discussed in [1]. It was demonstrated that the major disturbance was ascribed to the gearbox dynamics.

Accordingly, to achieve fine performance requirements with respect to the solar array pointing accuracy, the coupling of the gearbox disturbance with the satellite and solar array natural frequencies shall be avoided. The objective of this study is the estimation of such frequencies that are the starting point for the future design of a controller able to prevent further magnification of the disturbance amplitude.

Multiple approaches for the disturbance estimation were identified and compared in this thesis. The most common nonlinear techniques such as the extended Kalman filter [5], the unscented Kalman filter [19] and the particle filter [22] were investigated and the main characteristics with respect to the case at hand were explored. These methods require the definition of a state vector which includes the states dominating the dynamics of the system and the quantities of interest to be estimated. In addition, the dynamics of all the variables contained in the state vector shall be known to implement the algorithm. Since the disturbance acting on the satellite is not known and the available information is produced by the on-board sensor that do not detect directly the value of the gearbox disturbance and its variation over time, a direct estimation of the amplitude and frequency of such input signal cannot be carried out. This conclusion is obtained even in the simple case of a linear one-dimensional system with a single harmonic component as the input disturbance. The present study demonstrated that the amplitude and frequency of the input signal cannot be evaluated by means of an estimation technique based on the nonlinear Kalman filter theory because of the non-observability of the system. In the case direct information of the disturbance was available, it is possible to

implement a nonlinear Kalman filter with direct estimation of the quantities of interest, but a sensor that produces such measurement does not exist.

This thesis proposes an alternative approach which relies on the design of an estimator made up of two main components. A first filter based exclusively on the system dynamics generates a robust estimate of the input disturbance, while the second part of the filter decomposes such estimate in a series of harmonic components by evaluating the relative frequency and the amplitude spectra. In other words, the first estimator can be viewed as a sort of sensor whose output is the estimate of the input disturbance which is then provided to the second segment of the filter, overcoming the issues presented above. Furthermore, since the first filter is dependent only on the system, it is possible to introduce a different approach to generate the input estimation which relies on the linearity of the system. As a matter of fact, the nonlinearities are introduced exclusively by the input disturbance, while the satellite dynamics can be approximated as linear. In fact, the Euler equations which are used to model the dynamics of the spacecraft are nonlinear but can be easily linearised by assuming that the angular velocity of the satellite is small. The linearity assumption is typically realistic, since the external perturbations acting on the satellite and thus the motion are usually small. In addition, it brings the great advantage, that the mathematical formulations developed in a linear framework (which are, in general, easier than the nonlinear case and more mature) can be exploited. Linear approaches are in general easier to treat with respect to the nonlinear case and are typically more mature. In particular, the linear $\mathcal{H}_\infty$ theory was used to obtain a robust estimator which minimises the worst-case scenario by guaranteeing the attenuation of the input disturbance at any frequency. The $\mathcal{H}_\infty$ theory is typically devoted to the controller synthesis, but it was specialised for the filtering case, since it can be demonstrate to be a special case of the $\mathcal{H}_\infty$ control problem with no internal stability requirements.

For the frequency and amplitude spectrum estimation, this study proposed two different techniques which show benefits but also drawbacks. Different case were explored in which a simple one-dimensional system with one degree of freedom is subjected to different input disturbances. A first approach relies on the Fourier transform which showed precise estimation when the input amplitude and frequency are constant over time, by generated inaccurate results otherwise. In addition, it relies on the introduction of a time window over which the procedure is carried out, which makes it an *a posteriori* approach and can produce undesirable effects such as the spectral leakage when the time window is not consistently defined. The second technique relies on the nonlinear Kalman filter theory already mentioned. This latter option has the advantage to produce real-time estimates but suffers of poor accuracy if not correctly initialised. The final approach for the spectral estimation may then be the combination of the two methods. The estimation generated by technique which relies on the Fourier transform could be used to initialise the nonlinear Kalman filter approach in order to obtain real-time precise estimates.

This thesis can be considered as the starting point for different future developments. The present study does not encompass the parameter uncertainties of the system and the estimator is implemented for the nominal plant. However, manufacturing and measurement errors or slight variations in the characteristics of the system properties due to the exposure with a different environment may occur and are typically taken into account by introducing uncertain quantities including a deviation from the nominal value. These uncertainties might modify the system dynamics and the robust estimator developed in the present study may not satisfy completely the $\mathcal{H}_\infty$ requirements due to such variation. A more robust approach could be implemented by considering the system uncertainties

as well. One common approach relies on the μ-synthesis technique, which extends the methods of the $\mathcal{H}_\infty$ synthesis to design a more robust controller or estimator for an uncertain plant. Nevertheless, it is necessary to quantify the such system uncertainties to have information about the maximum extent to which the parameter values are supposed to change.

In addition, the estimation of the input disturbance generated by the solar array driving mechanism and the evaluation of the related frequency and amplitude spectra make it possible to synthesise a controller which prevents magnification of the input disturbance due to the coupling of the disturbance with the satellite and solar array natural frequencies. Thus, the controller can be designed such that the performance requirements are fulfilled and the related fine pointing accuracy of the solar is achieved.

Acknowledgements

I would like to acknowledge and thank my thesis supervisor Professor Camilla Colombo of the Aerospace Science and Technology Department at Politecnico di Milano for the valuable advice, constant support and patience during this long period of thesis development and writing. I am also truly grateful for giving me the opportunity to participate in several experiences, including the possibility to take part in my first international course at the ESA Education Training Centre in Belgium.

I would also like to express my gratitude to my supervisor at ESTEC Davide Oddenino for the great opportunity to work at ESA and for the precious support, continuous availability and the professional guidance given during the intense months of my internship.

Thank you to my parents that, despite the hard period we have been going through, have always encouraged and supported me in any decision I made, besides helping me in any way possible. All of this has been possible only thanks to you.

A huge thank you goes to my brother Alessandro. I appreciate your more silent support and I am extremely grateful to have an older brother like you.

Thank you to all the people I met during this university journey: Elena, Vittorio, Alessandra, Andrea, Arianna, Dario, Caterina and Diego, you made these last years the best of my life.

To conclude, I would like to thank my longer-standing friends, Daniela and Gianfranco for the essential support during the first period of the COVID-19 outbreak and Alice, the best listener (and with me the worst complainer) I know, for your patience and for all the valuable advice you have always given me.

Gianluca

Bibliography

[1] Daniel Alazard and Christelle Cumer. "Engineering tool for characterization of SADM induced disturbances and their effects on spacecraft pointing errors". 2018.

[2] Daniel Alazard and Christelle Cumer. "Satellite dynamics toolbox - Principles, user guide and tutorials". 2014.

[3] Daniel Alazard, Christelle Cumer, and Khalid Tantawi. "Linear dynamic modeling of spacecraft with various flexible appendages and on-board angular momentums". In: *7th International ESA Conference on Guidance, Navigation & Control Systems (GNC 2008)* (2008).

[4] Gary Balas et al. *Robust Control Toolbox™ 3 User's Guide*. MathWorks, Inc., 2012.

[5] J. Bellantoni and K. W. Dodge. "A square root formulation of the Kalman- Schmidt filter". In: *AIAA Journal* 5 (1967), pp. 1309–1314.

[6] M.E. Campbell and S. Brunke. "Nonlinear estimation of aircraft models for on-line control customization". In: *2001 IEEE Aerospace Conference Proceedings* 2.247 (2001), pp. 621–628.

[7] Jiangpan Chen and Wei Cheng. "Research on the disturbance generated by a solar array drive assembly driving a flexible system". In: *Journal of Theoretical and Applied Mechanics* 54 (2016), pp. 1001–1012.

[8] J.P. Chrétien and C. Manceaux-Cumer. "Minimal LFT form of a spacecraft built up from two bodies". In: *AIAA Guidance, Navigation, and Control Conference and Exhibit* (2001).

[9] Cornelius Dennehy and Oscar S. Alvarez-Salazar. "Spacecraft micro-vibration: a survey of problems, experiences, potential solutions, and some lessons learned". In: *European Conference on Spacecraft Structures, Materials and Environmental Testing (ECSSMET)* (2018).

[10] J. C. Doyle et al. "State-space solutions to standard $\mathcal{H}_2$ and $\mathcal{H}_\infty$ control problems". In: *IEEE Transactions on Automatic Control* 34.8 (1989), pp. 831–847.

[11] Carlton L. Foster et al. "Solar-array-induced disturbance of the Hubble space telescope pointing system". In: *Journal of Spacecraft and Rockets* 32.4 (1995), pp. 634–644.

[12] Bernard Friedland. *Control system design: An introduction to state-space methods*. Dover Publications, 1986. ISBN: 9780070224414.

[13] Pascal Gahinet and Pierre Apkarian. "A linear matrix inequality approach to $\mathcal{H}_\infty$ control". In: *International Journal of Robust and Nonlinear Control* 4.4 (1994), pp. 421–448.

[14] Steven Gillijns and Bart De Moor. "Unbiased minimum-variance input and state estimation for linear discrete-time systems". In: *Automatica* 43.1 (2007), pp. 111–116.

[15] Keith Glover and John C. Doyle. "State-space formulae for all stabilizing controllers that satisfy an $\mathcal{H}_\infty$-norm bound and relations to relations to risk sensitivity". In: *Systems & Control Letters* 11 (1988), pp. 167–172.

[16] Nicolas Guy et al. "A new attitude control design approach for flexible satellites". In: *IFAC Proceedings Volumes* 46.19 (2013), pp. 500–505.

[17] Robert Hermann and Arthur J. Krener. "Nonlinear controllability and observability". In: *IEEE Transactions on Automatic Control* 22.5 (1977), pp. 728–740.

[18] Robert L. Williams II and Douglas A. Lawrence. *Linear state-space control systems*. John Wiley & Sons, Inc., 2007. ISBN: 9780470117873.

[19] Simon J. Julier and Jeffrey K. Uhlmann. "A new extension of the Kalman filter to nonlinear systems". In: *Defense, Security, and Sensing* (1997).

[20] Rudolf Emil Kálmán. "A new approach to linear filtering and prediction problems". In: *Journal of Basic Engineering* 82.1 (1960), pp. 35–45.

[21] Jaechan Lim. "A tutorial – game theory-based extended $\mathcal{H}_\infty$ filtering approach to nonlinear problems in signal processing". In: *Digital Signal Processing* 34 (2014), pp. 1–15.

[22] Nicholas Metropolis and S. Ulam. "The Monte Carlo Method". In: *Journal of the American Statistical Association* 44.247 (1949), pp. 335–341.

[23] G. S. Nurre, J. P. Sharkey, and H. B. Waites. "Initial performance improvements due to design modifications for the pointing control system on the Hubble Space Telescope". In: *Guidance and Control 1991* (1991), pp. 493–511.

[24] Julie Penaud, Daniel Alazard, and Alexandre Amiez. "Kinematic analysis of spatial geared mechanisms". In: *Journal of Mechanical Design* 134.2 (2012), pp. 21009–21014.

[25] N. Zhou S. Akhlaghi and Z. Huang. "Adaptive adjustment of noise covariance in Kalman filter for dynamic state estimation". In: *2017 IEEE Power & Energy Society General Meeting* (2017), pp. 1–5.

[26] Francesco Sanfedino and Daniel Alazard. "Estimation of harmonic disturance within a Solar Array Drive Mechanism - A robust control approach". 2020.

[27] Dale E. Seborg and Michael A. Henson. *Nonlinear process control*. Prentice-Hall, Inc., 1997. ISBN: 9780136251798.

[28] Dan Simon. *Optimal state estimation - Kalman, $\mathcal{H}_\infty$ and nonlinear approaches*. Wiley-Interscience, 2006. ISBN: 9780470045336.

[29] European Cooperation for Space Standardization (ECSS). *Spacecraft mechanical loads analysis handbook*. European Space Agency (ESA), 2013.

[30] Lloyd N. Trefethen and David Bau. *Numerical linear algebra*. Society for Industrial and Applied Mathematics, 1997. ISBN: 9780898713619.

[31] Wikimedia.org. *Sentinel-2 model*. June 2015. URL: `https://commons.wikimedia.org/wiki/File:Sentinel_2-IMG_5873-white_(crop).jpg`.

[32] G. Zames. "Feedback and optimal sensitivity: Model reference transformations, multiplicative seminorms, and approximate inverses". In: *IEEE Transactions on Automatic Control* 26.2 (1981), pp. 301–320.

[33] Paul Zarchan and Howard Musoff. *Fundamentals of Kalman filtering: a practical approach*. American Institute of Aeronautics and Austronautics, 2009. ISBN: 9781600867187.

[34] Kemin Zhou. *Essentials of robust control*. Prentice Hall, 1998. ISBN: 9780135258330.